Theoretical Study of Passively Modelocked Lasers with Fast Saturable Absorbers

by

Chien-Jen Chen

Dissertation submitted to the Faculty of the Graduate School
of the University of Maryland in partial fulfillment
of the requirements for the degree of
Doctor of Philosophy
1993

Advisory Committee:

Professor Curtis R. Menyuk, Chairman/Advisor
Professor Chi H. Lee
Professor Gary M. Carter
Dr. Ping-kong A. Wai
Professor Chuan Sheng Liu

Abstract

Title of Dissertation: Theoretical Study of Passively Modelocked Lasers with Fast Saturable Absorbers

Chien-Jen Chen, Doctor of Philosophy, 1993

Dissertation directed by: Professor Curtis R. Menyuk
Department of Electrical Engineering

In this thesis, modelocked lasers with fast saturable absorbers are studied theoretically and numerically. We start from a laser equation which is closely related to the Ginzburg-Landau equation and is valid when the change of the laser pulse in a round trip is small. To determine whether a laser self-starts, we find the CW solution of the laser equation and then carry out a stability analysis around this solution. When the CW state is unstable, experimental work suggests that the laser will typically self-start from noise; in contrast, when the CW state is stable, experiments suggest that the laser typically tends toward a CW state. A dispersion relation that determines the growth rate of plane wave perturbations is derived and the laser can self-start if the growth rate is positive. We find the region in parameter space in which a modelocked laser can self-start.

To determine the stability of pulsed mode operation, we find the pulse solution of the laser equation and then linearize this equation around the pulse

solution. Both continuum modes and discrete modes of the linearized equation are studied and the conditions for a laser to operate stably are given. In particular, we find that gain saturation stabilizes the most unstable discrete eigenmode and is required for stable laser operation.

We apply these analyses to figure eight lasers and fiber ring lasers. The parameters used in the laser equation are first determined from physical parameters and then analysis is carried out. Numerical simulations that calculate wave evolution in laser cavities in a modular fashion are also carried out. The results from the analyses based on the laser equation and the simulations are then compared.

Dedication

To my family

Stephanie, for providing additional motivation to complete the research work.

The work reported here was supported by the Department of Energy and the National Science Foundation. Computer work was carried out at the National Energy Research Supercomputing Center and the San Diego Supercomputing Center.

Acknowledgements

The author would like to express his gratitude to Professor C. R. Menyuk for his guidance and encouragement in carrying out the research and preparing the manuscript. Professor Menyuk's critical comments helped to clarify numerous research ideas and to generate a more readable thesis.

The author is grateful to Dr. I. N. Duling, III at the Naval Research Laboratory who invented the figure eight laser and introduced this laser to the author. Dr. Duling's comments and suggestions often lead to better understanding of laser physics.

The author acknowledges guidance from Professor M. N. Islam of the University of Michigan who introduced the author to the experimental world of optics while the author was visiting AT&T Bell Laboratories. His dedication to his work and ability to bring new idea into experiments greatly impressed the author.

Special thanks goes to Dr. P. K. A. Wai, who spent considerable time and effort discussing the concept in this thesis with the author, and who helped the author in daily life. Also, Mr. V. R. Chinni, Mr. S. Saxena, and Mr. B. Raghavan help create a hard-working research group.

Last, but not least, the author thanks his wife, Dr. C.-T. Chiu, for her understanding and patience, his two-year-old son, Mark, and newborn daughter,

Contents

List of Figures

Chapter 1

Introduction

Since the invention of the laser in 1960, optical science and technology have grown rapidly in importance. Laser applications cover a broad range, from compact disks to nuclear fusion. Lasers provide coherent, high intensity, and possibly short duration optical beams for numerous purposes. In spite of being considered a mature technology, lasers are still an interesting research topic, as new laser systems and applications are constantly emerging.

While many complicated physical processes can occur in lasers, their basic operation is simple. Any laser must contain amplification and feedback, which work together as a resonator. In its simplest form, the laser could be a gain medium inside a pair of mirrors or a Fabry-Perot cavity [1], [2]. The gain medium amplifies the optical power while the mirrors provide feedback. There exist many laser cavity configurations, most of which can be classified conceptually as cavities in which light passes through one laser element after another in a cyclical fashion. We will call this type of cavity a cyclical cavity, and all the lasers which we will study in this thesis are of this type. A Fabry-Perot cavity is a cyclical cavity if the waves traveling in opposite directions have little interaction; by

contrast, a Fabry-Perot cavity is not a cyclical cavity if the coupling of waves traveling in opposite directions is strong.

In this thesis, we will theoretically and computationally study passively modelocked lasers. While lasers contain both longitudinal and transverse modes [1]-[3], our study will focus on the longitudinal modes. These longitudinal modes are determined by the cavity configuration and have a frequency spacing of $\Delta f = 1/T_R$, where T_R is the round trip time of the cavity. In a Fabry-Perot cavity, the frequency separation is $c/2L$, where L is the optical length of the cavity and c is the speed of light. Since a gain medium typically provides gain over a wide frequency range, many longitudinal modes typically exist.

The output electrical field of a laser is a sum of the field contribution from all the modes surrounding the central frequency f_0. The n-th mode from the central frequency, f_0, can be written as $E_n \exp[2\pi(f_0 + n\Delta f)t + \phi_n]$, where E_n is the amplitude of this mode and ϕ_n is the phase. The total field can be represented as [3]-[5]

$$E(t) = \sum_n E_n \exp[2\pi(f_0 + n\Delta f)t + \phi_n]. \tag{1.1}$$

When the phase ϕ_n of each mode is random, the output $E(t)$ will fluctuate. In a CW laser, from which a monochromatic output is desired, a frequency limiting element, such as a birefringent plate, is used to exclude unwanted modes. However, in many applications in spectroscopy and telecommunications, a pulsed output is desirable, in which case a large bandwidth is needed. However, the modes must be properly related. A large amount of work has been done in generating short pulses [1]. In Section 1.1, we will briefly discuss some commonly used techniques.

1.1 Pulse generation techniques

Q-switching is one way to generate short and intense pulses [1], [6]. In the first stage of Q-switching, the gain medium is pumped while the laser feedback is blocked by lowering the "quality factor" of the cavity. There is no output energy at this point, but energy is stored in the gain medium in the form of a large population inversion. One then abruptly turns on the feedback, so that the laser dumps the stored energy, quickly depleting the inverted atomic population and producing a burst of high-intensity light. Methods of changing the quality factor include mechanically rotating mirrors, electro-optic devices, and saturable absorbers. The pulse widths of Q-switched pulses of a Nd:YAG laser are in nanoseconds.

Another category of pulse generation technique is modelocking [3]-[5]. Modelocked lasers are lasers that maintain a constant amplitude and phase relation among longitudinal modes. From Eq. (1.1), we find that when E_n and ϕ_n remain fixed, the output is regular and periodic. In particular, when the set $\{E_n \exp(\phi_n)\}$ are the Fourier coefficients of a pulse, the laser will generate pulsed output. To modelock a laser, one must introduce a mechanism which forces the amplitudes and phases of the most significant modes to couple and, as a consequence, to maintain a constant relationship.

There are several ways to modelock a laser. A simple idea is to introduce an element that can change the gain or loss and can be synchronized with the pulse round trip time. For instance, one may introduce an acoustic optical modulator which operates at the repetition rate of the laser, or one may pump the gain medium at the same rate to modify the gain [1], [7]. In this case, the amplitude of each mode is modulated and E_n becomes $E_n(1 + m\cos 2\pi\Delta f t)$,

where m is the modulation constant. A pulse train may form to minimize the loss from the modulator or maximize the gain from the amplifier. This sort of modelocking is called AM modelocking. Modulating the phase ϕ_n, such that it becomes $\phi_n + m\cos 2\pi\Delta f t$, is another way to align the modes [1], [7]. This type of modelocking is called FM modelocking. Both AM and FM modelocking are referred to as active modelocking because they use external modulators. Since the modulation in loss or gain is usually slow, active modelocking cannot generate sub-picosecond pulses. To generate very short pulses, one must use passive modelocking which is described in the next section.

1.2 Elements of passive modelocking

The final modelocking approach which we will discuss is passive modelocking, which is realized by using saturable absorbers [1], [2]. The function of a saturable absorber is to pass a larger fraction of the optical power during the higher intensity portion of a light pulse. The absorber can be made from organic dyes, gases, solid state devices, or an interferometric setup of several components. To minimize the loss due to passing through saturable absorbers, pulses tend to increase their amplitude and decrease their pulse width. Pulse widths on the order of femtoseconds have been observed using passively modelocked lasers.

In the frequency domain, the existence of nonlinearity is essential for a modelocked laser since it provides coupling between longitudinal modes. Due to the coupling of longitudinal modes, their relative amplitudes and phases lock. Saturable absorbers are nonlinear elements. The spectral width is increased when a pulse passes through a saturable absorber, which thereby generates more side-

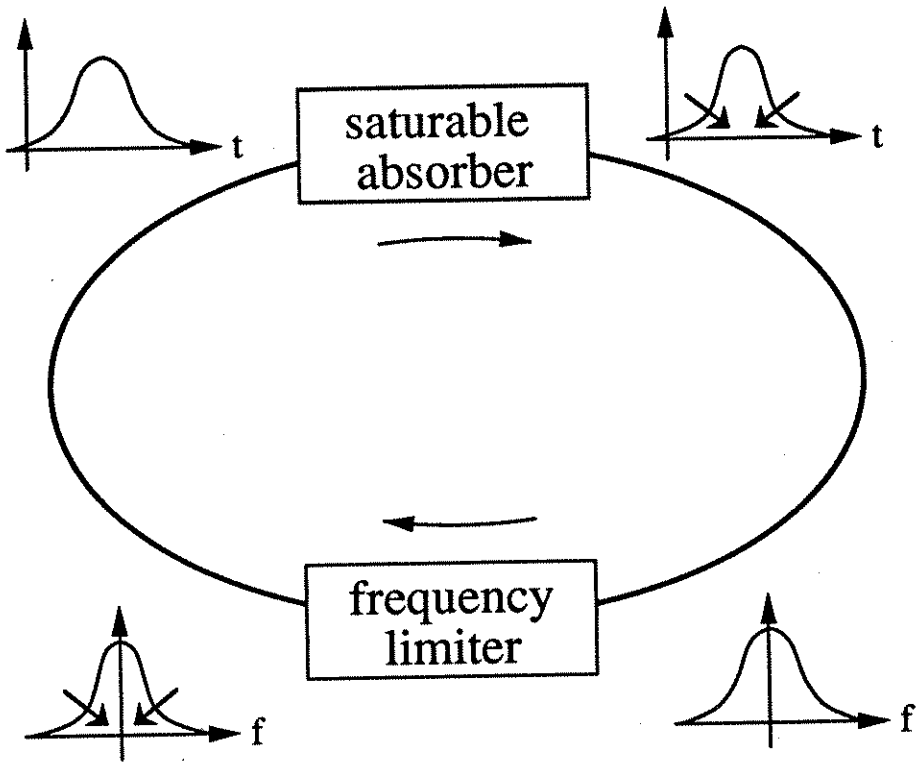

Figure 1.1: Schematic illustration of the balance between a fast saturable absorber and a frequency limiter.

bands.

An important element in a passively modelocked laser, in addition to saturable absorption, is a frequency limiter [8]-[10]. A saturable absorber cuts off the low intensity wings of a pulse and tends to reduce its time duration. The process cannot go on without limit. A frequency limiter becomes increasingly significant as the pulse width decreases and the spectral width increases. A frequency limiter usually has a bell shaped transmission curve around its central frequency in the frequency domain. It works in the frequency domain to reduce spectral width like the saturable absorber works in the time domain to reduce pulse width. When a balance is reached, a pulse train is generated. In Fig. 1.1, we illustrate schematically this balancing effect.

It is common that the frequency limiter does not consist of a single, identifiable laser element. Instead, many components and effects in the cavity combine to produce the frequency limiter. The gain medium itself has a finite spectral width, which sets the ultimate limit on the frequency content that a pulse generated by using that gain medium can have. Other elements which may further limit the frequency include birefringent plates, dichroic couplers, and even mirrors.

There are other effects which appear in a passively modelocked laser cavity. For example, some optical components are dispersive and some are nonlinear. Dispersion implies that different frequency components of a pulse travel at different speeds. Dispersion can exist in the gain medium, in a prism, or in a length of optical fiber. A particularly important nonlinearity is the Kerr nonlinearity. The Kerr nonlinearity implies that higher intensity portions of a pulse travel more slowly than the low intensity portions since the induced refractive indices are higher when the intensity is higher. A short pulse generally has high peak intensity and the nonlinearity may be significant in many components. Both dispersion and nonlinearity impact the quality of the pulses which are ultimately produced because they combine to generate chirp.

1.3 Research topics

Much of the work in this thesis is concerned with determining the stability of the laser's CW and/or pulsed mode operation. When we speak of an operating mode as stable, we mean that when it is perturbed by a small amount, the perturbation will always decay or at least not grow. By contrast, when an unstable operating

mode is perturbed, at least some perturbations will grow. Even if an operating mode is stable with respect to small perturbations, it may be unstable with respect to large ones. Thus, it is useful to operate a modelocked laser in the middle of a large sea of stability so that it is hard to destabilize the laser with large perturbations. We will map out these seas of stability. Conversely, when self-starting a laser from noise, experiments indicate that one must destabilize CW mode operation, and it is occasionally useful to artificially introduce large fluctuations in the laser to induce modelocking when the CW state is stable.

Stability of the CW state has been studied for various laser equations which are obtained by assuming that the change of a laser pulse in one round trip is small. The effect of saturable absorption [11], [12] and gain saturation [13] on self-starting has been reported. However, the effect of a frequency limiter, dispersion, and the Kerr nonlinearity have not yet been examined. We will examine self-starting of passively modelocked lasers based on a laser equation that includes all of these phenomena.

The stability of pulsed mode operation has been studied to date using two almost diametrically opposite approaches. In the first approach, which is analytical, one, again, uses the idealization in which the pulse evolution during a single pass through the laser is assumed to be small to obtain a simple equation, closely related to the Ginzburg-Landau equation, which describes the evolution. One then determines the equilibria of this equation and their stability. Determining the stability is a crucial step since only *stable* equilibria can occur in nature; yet, it is a step that is hard to carry out analytically, and work to date [8], [14] has relied on approximate methods which require considerable *a priori* physical insight into the form that the most unstable perturbations will have.

In the second approach, which is computational, one simulates the entire evolution of light within the laser, starting from noise [15]-[17]. Numerical simulation provides details of the wave evolution from initial noise to either stable pulses or chaotic waveforms; however, unlike analytical studies, numerical simulations do not provide a global view of the laser behavior over a wide parameter regime. We have carried out both analytical and computational studies of the pulse mode stability problem. Without using approximations in contrast to previous studies, we solve the eigenvalue problem which determines the growth rate of the perturbations and, hence, the stability of pulsed mode operation.

1.4 Summary of contents

We will consider all of the effects mentioned in Section 1.2 in the study of passively modelocked lasers. Derivation of the laser equation is introduced in Chapter 2. The pulse change during one round trip in the laser cavity is assumed to be small and the laser equation is written as a partial differential equation, in which the number of round trips is the propagation variable. We also discuss the modeling of elements often seen in a passively modelocked laser and how they fit into our formalism.

In Chapter 3, we study the stability of both the CW and modelocked states. A laser may have a steady modelocked state which cannot be observed when the laser is powered on because the CW state is stable, and the laser tends toward that state. We assume, consistently with experimental results, that the laser will only self-start if the CW state is unstable and the modelocked state is stable. We therefore evaluate the stability of both states by linearizing the laser equation

around the CW or pulsed solution and obtaining an eigenvalue problem, which is studied both analytically and numerically. The numerical methods that we use to study the eigenvalue problem and to calculate the pulse evolution are described.

As examples, we study the figure eight laser in Chapter 4 and the fiber ring laser in Chapter 5. Both lasers are primarily made from fibers and erbium-doped fiber amplifiers are used as gain media. In the figure eight laser, the fast saturable absorber is implemented using an amplifying nonlinear loop mirror, while in the fiber ring laser, the saturable absorption is due to nonlinear polarization rotation. Using the parameters of all elements in the cavity, we derive the parameters used in the laser equation and carry out the analysis outlined in Chapter 3.

We also use the beam propagation method to simulate both lasers in a modular fashion. By iterating the wave profile as it passes through each element in the cavity during one round trip after another, we follow the light evolution in the cyclical cavity. For both lasers, within some parameter ranges, modelocked pulses are observed to self-start from initial noise. Finally, conclusions and future research topics are discussed in Chapter 6.

Chapter 2

The laser equation and modeling of laser elements

A laser system is modular in nature, *i.e.*, it is composed of elements which have different physical effects on the electromagnetic field propagating in them. For instance, the optical energy increases as light passes through the gain section of the laser, but decreases as it passes through an output coupler. A component can affect the optical fields in more than one way. For example, an optical fiber is dispersive as well as nonlinear.

We write down the effect of each element, which is represented by a specific operator, and derive the laser equation in Section 2.1. In doing so, we assume that the pulse shape does not change significantly when it passes through any element in the cavity—an assumption which is valid for many modelocked lasers. These operators are therefore additive and the ordering during one round trip is not important.

Various physical effects commonly observed in a passively modelocked laser, such as saturable gain, loss, frequency limiting, dispersion, saturable absorption, and Kerr nonlinearity are discussed. In Section 2.2, we outline the mathematical

model used to describe these effects in detail. The saturable gain and saturable absorption need a more detailed description, which are given in Section 2.3. A summary is then given in Section 2.4.

2.1 The laser equation

We use an operator to mathematically model each physical effect. The output optical wave profile after the effect acts is related to the input wave profile before the effect acts by the transformation

$$U_{\text{out}}(t) = \mathcal{T} U_{\text{in}}(t), \tag{2.1}$$

where t is time, $\mathcal{T}$ is an operator corresponding to a particular physical effect, $U(t)$ is the electrical field vector, and U_{in} and U_{out} refer respectively to the values of U before and after the effect. In most cases, $\mathcal{T}$ is a constant operator, a differential-integral operator, or an operator described by an evolution equation.

A convenient and natural representation of the operator $\mathcal{T}$ is the exponential form, *i.e.*, $\exp(\mathcal{O}) = \mathcal{T}$, where $\mathcal{O}$ is an operator. Hence, Eq. (2.1) can be written as

$$\frac{\partial U(z,t)}{\partial z} = \mathcal{O} U(z,t), \tag{2.2}$$

where z is the number of round trips, meaning that $U(z=0) = U_{\text{in}}$ and $U(z=1) = U_{\text{out}}$. Formally, we write $U_{\text{out}} = \exp(\mathcal{O}) U_{\text{in}}$ and the equivalence of $\exp(\mathcal{O}) = \mathcal{T}$ is evident. The wave profile $U(z,t)$ is normalized such that $|U(z,t)|^2$ represents optical power.

Since the change in pulse shape in a laser cavity is modular in nature, one way to study the dynamics of a cyclical laser, in which light passes one laser element after the other, is to iterate the optical wave over successive actions of

the elements. The wave shape after one round trip is then related to the input wave shape through

$$U(z=1,t) = \mathcal{T}_n \cdots \mathcal{T}_1 U(z=0,t) = \exp(\mathcal{O}_n) \cdots \exp(\mathcal{O}_1) U(z=0,t), \qquad (2.3)$$

where n elements are assumed to exist in the laser cavity. Light passes through each element, acquiring a change in its pulse shape, until an equilibrium is reached. Alternatively, an equilibrium may not exist, and the pulse shape continues to change in a chaotic way forever.

Since the operators $\mathcal{O}_1, \cdots, \mathcal{O}_n$ do not commute in general, *i.e.*, $\mathcal{O}_i \mathcal{O}_j \neq \mathcal{O}_j \mathcal{O}_i$, the operator, $\exp(\mathcal{O}_n) \cdots \exp(\mathcal{O}_1) \neq \exp(\mathcal{O}_n + \cdots + \mathcal{O}_1)$. However, when the laser system is close to its equilibrium, the change in the pulse shape as light passes through each element is small, and hence the operators nearly commute. Generally, when $\mathcal{O}_1, \cdots, \mathcal{O}_n$ are small compared to unity, the sequence of operators in Eq. (2.3) can be approximated by treating them as if they commuted, *i.e.*,

$$\exp(\mathcal{O}_n) \cdots \exp(\mathcal{O}_1) \approx \exp(\mathcal{O}_n + \cdots + \mathcal{O}_1). \qquad (2.4)$$

The evolution of the pulse shape over round trip can then be written as

$$\frac{\partial U(z,t)}{\partial z} = (\mathcal{O}_n + \cdots + \mathcal{O}_1) U(z,t), \qquad (2.5)$$

which determines the laser equation when $\mathcal{O}_1, \cdots, \mathcal{O}_n$ are known for a given laser.

This approximation is made clearer by considering the Baker-Hausdorff formula [18],

$$\exp(\mathcal{O}_2)\exp(\mathcal{O}_1) = \exp\left(\mathcal{O}_1 + \mathcal{O}_2 + \frac{1}{2}[\mathcal{O}_2, \mathcal{O}_1] + \frac{1}{12}[\mathcal{O}_2 - \mathcal{O}_1, [\mathcal{O}_2, \mathcal{O}_1]] + \cdots\right), \qquad (2.6)$$

where $[\mathcal{X}, \mathcal{Y}] = \mathcal{X}\mathcal{Y} - \mathcal{Y}\mathcal{X}$ is the commutator. It is possible to generalize this formula to include more than two operators by applying Eq. (2.6) many times. The asymmetry of the ordering of the elements is taken care of by the commutators in the second and higher order terms. Therefore, when the approximation is applied, we ignore the order of elements in the cavity. To increase the accuracy of the approximation in Eq. (2.4), one can in principle include higher order commutator terms, although we do not use this approach in this thesis.

In the subsequent sections, we will describe in detail the modeling of the physical effects that are often seen in a laser cavity.

2.2 Elements inside laser cavities

The operator representations for constant gain, constant loss, constant phase shift, frequency limiting, dispersion, and Kerr nonlinearity are introduced. We follow the formalism described in Section 2.1.

2.2.1 Constant gain, loss, and phase shift

We study a constant gain element as the first example. A power gain of G_0 means $|U_{\text{out}}|^2 = G_0|U_{\text{in}}|^2$ and can be modeled by

$$\frac{\partial U}{\partial z} = \frac{\ln(G_0)}{2} U. \tag{2.7}$$

The original power relation between U_{in} and U_{out} is obtained, by integrating Eq. (2.7) and assigning $U(z = 0) = U_{\text{in}}$ and $U(z = 1) = U_{\text{out}}$. For a 30 dB gain, G_0 has a value of 1000. The operator $\mathcal{T} = \sqrt{1000}$ and $\mathcal{O} = \ln(1000)/2 \approx 3.45$ are constant operators. A constant loss ($G_0 < 1$) has a similar representation. The

effect of a uniform phase shift, θ, is modeled by

$$\frac{\partial U}{\partial z} = i\theta U. \tag{2.8}$$

By integrating this equation from $z = 0$ to $z = 1$, we recover the input/output relation, $U_{\text{out}} = \exp(i\theta)U_{\text{in}}$.

2.2.2 Frequency limiter

Most components used in a laser cavity are frequency dependent. For example, a mirror or a dichroic beam splitter has different reflection or transmission coefficients at different wavelengths. Also, the gain media have different amplification factors at different wavelengths. There are other frequency dependent effects, such as chromatic dispersion, which will be discussed latter. We shall first focus on frequency limiting, which affects the transmission of light at different wavelengths.

A frequency limiter is modeled as an optical bandpass filter, which has a Lorentzian shaped filter function in the frequency domain and has a bandwidth ω_0. The output wave shape is related to the input beam in the frequency domain by

$$\tilde{U}_{\text{out}}(\omega) = \frac{1}{1 + (\omega/\omega_0)^2}\tilde{U}_{\text{in}}(\omega), \tag{2.9}$$

where $\tilde{U}(\omega)$ is the Fourier transform of $U(t)$, defined as $\int_{-\infty}^{\infty} U(t)\exp(i\omega t)dt$. By using a Taylor expansion, the filter function can be approximated as $1-(\omega/\omega_0)^2+\cdots$, which yields $\tilde{U}_{\text{out}}(\omega) \approx [1 - (\omega/\omega_0)^2]\tilde{U}_{\text{in}}(\omega)$, when the limiter bandwidth is large compared to the pulse bandwidth.

Evaluating the bandwidth of the frequency limiter at the 3 dB power loss

points, we obtain the bandwidth, $\Delta\omega$, as

$$\Delta\omega = 2\sqrt{\sqrt{2}-1}\omega_0 \approx 1.287\omega_0. \tag{2.10}$$

When bandwidth, $\delta\lambda$, is given (generally in nm), we deduce the following formula for ω_0,

$$\omega_0 = \frac{2\pi c}{1.287\lambda_0^2}\delta\lambda, \tag{2.11}$$

where λ_0 is the free space wavelength.

In the time domain, using the Fourier transform relations, $d/dt \leftrightarrow -i\omega$, we find

$$U_{\text{out}}(t) = \left(1 + \frac{1}{\omega_0^2}\frac{d^2}{dt^2}\right) U_{\text{in}}(t). \tag{2.12}$$

In order to fit Eq. (2.12) into the formalism discussed in Section 2.1, we approximate the operator by $\exp(Bd^2/dt^2)$, where $B = 1/\omega_0^2$, assuming that the effect of frequency limiting is small. Finally, the effect of the frequency limiter is expressed as

$$\frac{\partial U}{\partial z} = B\frac{\partial^2}{\partial t^2}U. \tag{2.13}$$

2.2.3 Dispersion

Another frequency dependent phenomenon usually seen is chromatic dispersion. It is best described by the dispersion relation $k(\omega)$, which determines the wavenumber as a function of frequency. A well known result is that the group velocity v_g of a narrow band pulse can be calculated from $v_g = \partial\omega/\partial k$ evaluated at the center frequency, ω_{cent}. Since the first derivative of the dispersion relation only affects the pulse propagation velocity, the pulse shape is altered by second or higher order terms. The second derivative of the dispersion

relation, which is related to the group velocity dispersion, is the principal source of pulse spreading.

The dispersion inside a laser cavity is generally due to the combined effect of several laser elements. For instance, both a segment of a optical fiber and the gain medium would typically contribute to the dispersion. Dispersion in a material is modeled by the equation [18]

$$\frac{\partial U}{\partial \Xi} = -i\frac{k''}{2}\frac{\partial^2}{\partial t^2}U, \tag{2.14}$$

where Ξ is the propagation distance, ranging from 0 to L_{mat}, the material length, and $k'' = \partial^2 k/\partial\omega^2$ evaluated at $\omega = \omega_{\text{cent}}$. Setting $\Xi = zL_{\text{mat}}$, we introduce z into Eq. (2.14) and obtain

$$\frac{\partial U}{\partial z} = -iL_{\text{mat}}\frac{k''}{2}\frac{\partial^2}{\partial t^2}U. \tag{2.15}$$

Therefore, the operator that describes the dispersion is,

$$\mathcal{O} = iD\frac{\partial^2}{\partial t^2}, \tag{2.16}$$

where $D = -L_{\text{mat}}k''/2$, which is the total dispersion which occurs over a length L_{mat}. With such a definition of dispersion, $D > 0$ corresponds to anomalous dispersion, and $D < 0$ corresponds to normal dispersion. Integrating Eq. (2.15) from 0 to 1 to obtain the relation between input and output fields, we find

$$U_{\text{out}}(t) = \frac{1}{2\pi}\int_{-\infty}^{\infty}\tilde{U}_{\text{in}}(\omega)\exp(-iD\omega^2)\exp(-i\omega t)d\omega, \tag{2.17}$$

where $\tilde{U}_{\text{in}}(\omega)$ is the Fourier transform of $U_{\text{in}}(t)$, the input pulse, and $U_{\text{out}}(t)$ is the output pulse.

In practice, dispersion is measured and denoted as D_m which is in delay time per unit material length per unit wave length [19]. The parameter D_m is related

to k'' through

$$D_m = \frac{\partial}{\partial \lambda}\left(\frac{1}{v_g}\right) = -\frac{2\pi c}{\lambda_0^2}k''. \tag{2.18}$$

We have $D = L_{\mathrm{mat}} D_m \lambda_0^2/(4\pi c)$ when D is expressed in terms of D_m.

The effect of dispersion is to broaden the temporal size of the optical pulse and generate a chirp in its frequency content. In a medium with anomalous dispersion, the higher frequency portion of a pulse travels faster, and the rising part of the pulse amplitude contributes to the higher frequency components. The broadening effect is more significant for shorter pulses which have larger spectra.

2.2.4 Kerr nonlinearity

When the optical intensity in a material is large, the polarizability of the material may change in response, leading to a nonlinear refractive index change. As a consequence, the index of refraction for the peak and the wings of a pulse will differ. The most important nonlinearity in lasers is the Kerr nonlinearity. The Kerr nonlinearity affects the phase of an optical beam through the intensity dependent refractive index n. The dependence of n on the optical intensity I is $n = n_0 + n_2 I$. In optical fibers, $n_0 = 1.45$ is the low intensity refractive index and n_2 is the Kerr coefficient having a value of 3.2×10^{-20} $\mathrm{m^2W^{-1}}$. In general, over the material length, the Kerr effect on wave propagation is described by [18]

$$\frac{\partial U}{\partial \Xi} = i\frac{2\pi n_2}{\lambda_0 A_{\mathrm{eff}}}|U|^2 U, \tag{2.19}$$

where A_{eff} is the effective area of the nonlinear medium. Since U is normalized to represent power, $|U|^2/A_{\mathrm{eff}}$ represents optical intensity. In an optical fiber,

effective area is around 2 to 4 $\times$ the core area of the fiber, depending on the intensity profile over the cross section.

Again, using $\Xi = zL_{\text{mat}}$ and writing down the propagation equation in z, we may identify the operator

$$\mathcal{O} = iK|U|^2 = i\frac{2\pi n_2 L_{\text{mat}}}{\lambda_0 A_{\text{eff}}}|U|^2, \tag{2.20}$$

where K is defined as $(2\pi n_2 L_{\text{mat}})/(\lambda_0 A_{\text{eff}})$, which is the total Kerr nonlinearity in the material.

It is possible to integrate Eq. (2.19) directly. Since only the phase changes when the input wave profile propagates in accordance with Eq. (2.19), we find $|U(z)| = |U_{\text{in}}|$ at any z value, so that

$$U_{\text{out}} = \exp(iK|U_{\text{in}}|^2)U_{\text{in}}. \tag{2.21}$$

The overall operator $\mathcal{T} = \exp(\mathcal{O}) = \exp(iK|U_{\text{in}}|^2)$ represents a non-uniform phase shift over the pulse. The spectral content of a pulse is affected by the nonlinear phase. Since $\omega = -\partial K|U_{\text{in}}|^2/\partial t$, from the definition of the Fourier transform, the frequency of the rising part, or the incoming part, of the pulse is downshifted.

2.3 Saturable gain and saturable absorption

Since a saturable amplifier and a saturable absorber themselves are dynamical systems, they play an important role in the dynamics of passively modelocked lasers. Generally, both the saturable gain and the saturable absorber can be treated with the same type of rate equation which depends upon the population differences in the molecular levels of their material. In this thesis, we will assume

that the saturable amplifiers have a large relaxation time, while the saturable absorbers have a small relaxation time. While that is not the case for all lasers, it is the case for the figure eight lasers and the fiber ring lasers which we will ultimately be modeling.

2.3.1 Saturable gain

A saturable amplifier produces less gain as the input power, integrated over the relaxation time, increases. The detailed dependence of the gain on the input power varies for different gain media and should be determined by experiments.

A rate equation which is valid in two-level media may be used to describe a small segment of the saturable amplifier [1], [8]. The gain is described by a first order differential equation in t [8], [12]-[20],

$$\frac{dg}{dt} = -\frac{g - g_0}{T_0} - \frac{|U(t)|^2}{T_0 P_{\text{sat}}} g, \tag{2.22}$$

where T_0 is the relaxation time and P_{sat} is the saturation power. The product $T_0 P_{\text{sat}}$ is denoted as E_{sat} and is related to the beam cross section, A_{sec}, in the medium and the optical cross section, σ_c, of the medium through the equation [1], [20]

$$\frac{1}{E_{\text{sat}}} = \frac{1}{T_0 P_{\text{sat}}} = \frac{\sigma_c}{\hbar \omega_0 A_{\text{sec}}}. \tag{2.23}$$

When $U(t) = 0$, for example between optical pulses, the gain will reach a steady value in which $dg/dt = 0$. The value of g_0 is related to the small signal gain and is dependent upon the pumping power applied to the gain medium. For a continuous wave input $U = U_c$, where U_c is a constant, the gain medium again reaches a steady state. The steady state gain, g_s, can be expressed as [21]

$$g_s = \frac{g_0}{1 + P_{\text{av}}/P_{\text{sat}}}, \tag{2.24}$$

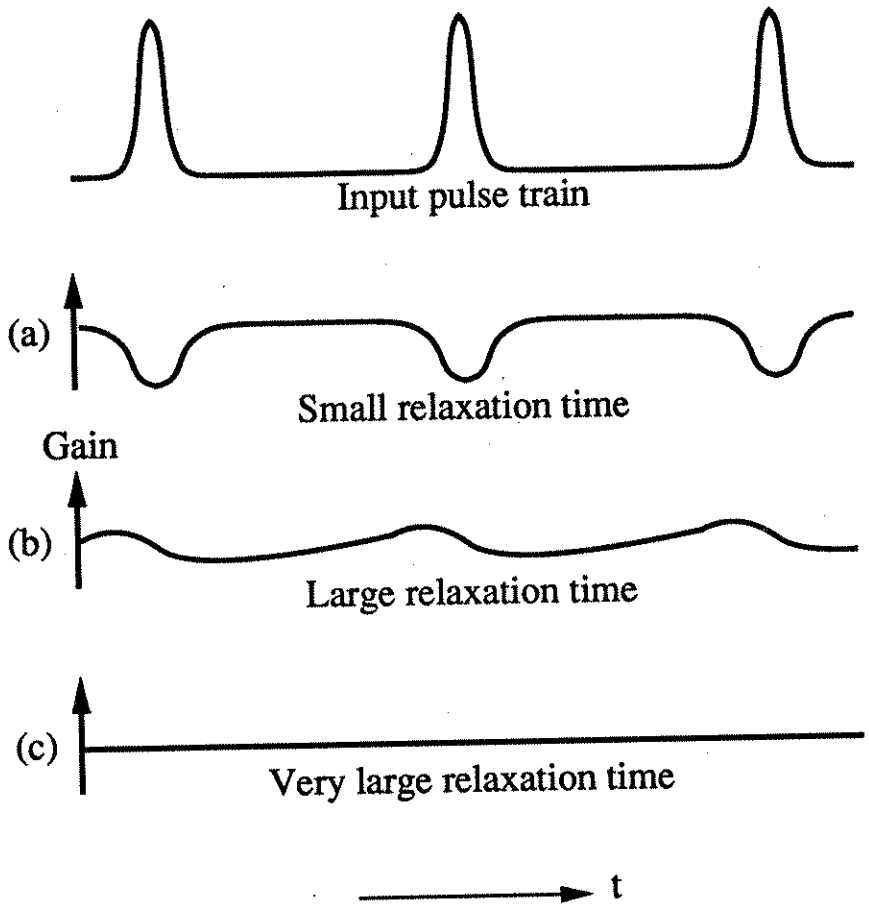

Figure 2.1: Gain characteristics for a pulse train input, (a) small relaxation time, (b) large relaxation time, and (c) very large relaxation time.

where $P_{av} = |U_c|^2$ is the average power.

It is interesting to compare two extremes of the relaxation time T_0 when U consists of a series of optical pulses. When T_0 is much smaller than the fluctuation time of the input, g reaches its steady state relatively fast, and the gain can catch up to the variation in the input and has an expression given by

$$g(t) = \frac{g_0}{1 + |U(t)|^2/P_{sat}}. \tag{2.25}$$

The variation in gain is shown in Fig. 2.1(a) for a pulse train input. On the

other hand, when T_0 is large so that $1/T_0 \ll |U_{\text{peak}}|^2/T_0 P_{\text{sat}}$, where $|U_{\text{peak}}|^2$ is the peak power of $U(t)$, the first term in Eq. (2.22) is negligible and $g(t)$ may be found by direct integration of the remaining term [13],

$$g(t) = g_s \exp\left(-\int_{-\infty}^{t} \frac{|U(t')|^2}{T_0 P_{\text{sat}}} dt'\right). \tag{2.26}$$

After the pulse passes, the gain increases slowly to its steady state value, where it remains until the arrival of next pulse as shown in Fig. 2.1(b). The change in the gain is slow when the gain variation is compared to the previous case in Fig. 2.1(a). Furthermore, when T_0 is very large compared with the pulse width τ so that $\tau|U_{\text{peak}}|^2/T_0 P_{\text{sat}} \ll 1$, the integration in Eq. (2.26) is small and the gain is virtually a constant g_s as shown in Fig. 2.1(c).. The value of g_s is determined by the average power of the pulse train as in Eq. (2.24); however, the average power P_{av} is the ratio of the energy in one pulse and the round trip time. In practice, for gain media such as Ti:sapphire whose relaxation time is in microseconds and erbium doped fibers whose relaxation time is in milliseconds, the gain formula, Eq. (2.24), is adequate for a pulse width of picoseconds.

The overall gain is found by summing the effect of each small section over the entire medium. To do so, we perform an integration from $z = 0$ to $z = 1$ on the following operational equation,

$$\frac{\partial U}{\partial z} = g_s U. \tag{2.27}$$

The length of the medium is taken into account in Eq. (2.27); however, we keep the same notation g_s.

In the large T_0 limit and with a pulse train input in mind, the average power that determines g_s is $P_{\text{av}} = E_R/T_R$, where $E_R = \int_0^{T_R} |U|^2 dt$ is the optical energy in one round trip and T_R is the round trip time of the laser cavity. Multiplying

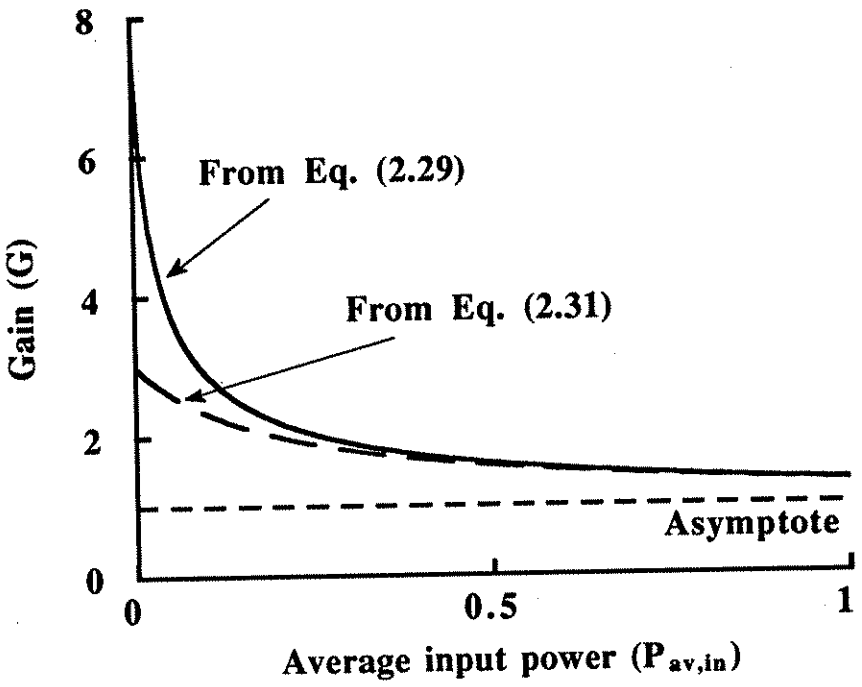

Figure 2.2: Gain as a function of input power (solid line) is calculated from Eq. (2.29) with $g_0 = 1$ and $P_{sat} = 0.2$. Approximate gain (dashed line) is calculated from Eq. (2.31).

both sides of Eq. (2.27) by U^*, the complex conjugate of U and carrying out some algebraic manipulation, we obtain [1]

$$\frac{\partial P_{av}}{\partial z} = \frac{2g_0}{1 + P_{av}/P_{sat}} P_{av}. \tag{2.28}$$

The input and output power are found to satisfy the relation,

$$P_{av,out} \exp\left(\frac{P_{av,out}}{P_{sat}}\right) = P_{av,in} \exp\left(\frac{P_{av,in}}{P_{sat}} + 2g_0\right). \tag{2.29}$$

We plot the power gain, $G = P_{av,out}/P_{av,in}$, versus $P_{av,in}$ in Fig. 2.2 by solving Eq. (2.29) numerically. The overall gain decreases and approaches unity as the input

power increases. On the low input power side, both $P_{\text{av,in}}$ and $P_{\text{av,out}}$ are small compared with P_{sat} and $G \approx \exp(2g_0)$, which is the small signal power gain. On the high input power end, the gain decays to unity at a rate of $1/P_{\text{av,in}}$, which can be justified by the following argument. When $G = P_{\text{av,out}}/P_{\text{av,in}} \approx 1$ and both $P_{\text{av,in}}$ and $P_{\text{av,out}}$ are much larger than P_{sat}, the effect of the factor $\exp(2g_0)$ becomes less important. From Eq. (2.29), it then follows that

$$G \approx 1 + 2g_0 + \frac{P_{\text{av,in}}}{P_{\text{sat}}}(1 - G). \tag{2.30}$$

The right hand side is from expansion of the exponential function to first order. The over all gain is found easily to be

$$G = \frac{P_{\text{av,out}}}{P_{\text{av,in}}} \approx 1 + \frac{2g_0}{1 + P_{\text{av,in}}/P_{\text{sat}}}. \tag{2.31}$$

Two key parameters, g_0 and P_{sat}, are measurable from experiments. In a segment of erbium-doped fiber, the value of g_0 ranges from around 2 to 4, corresponding to a small signal gain of 17 dB to 35 dB. The saturation power is 1 to 3 mW. Using Eq. (2.29) to fit a set of experimental data from Dr. I. Duling of the Naval Research Laboratory, we find $g_0 = 3.94$ and $P_{\text{sat}} = 2.77$ mW [22]. The relaxation time for the erbium dopant is 10 msec.

2.3.2 Saturable absorption

The last element in a passively modelocked laser which we will consider is the saturable absorber. A saturable absorber has an intensity dependent transmission coefficient. It sharpens a pulse by letting a larger fraction of the energy pass through in the high intensity peak than in the low intensity wings. As a consequence, a saturable absorber can shorten the pulse duration. This effect is remarkable, considering that most of the elements inside a laser cavity tend

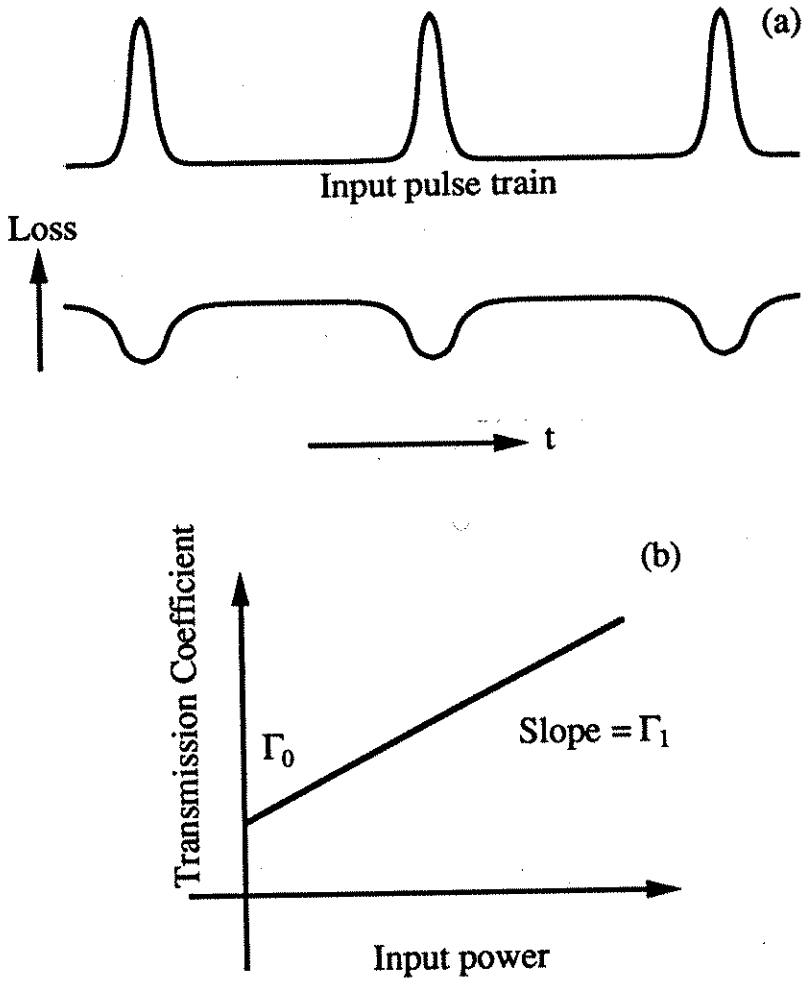

Figure 2.3: (a) Loss characteristics for a pulse train input. (b) Transmission coefficient versus input power.

to broaden the pulse in the time domain. In a physical saturable absorber such as a dye jet, the population difference of the saturable absorber is modeled by the same type of equation as Eq. (2.22) except that now the gain becomes a loss. Saturable absorbers can be classified as slow or fast, depending upon their response times.

We are only interested in saturable absorbers with short relaxation times, which by definition have a very short response time with respect to the pulse duration. Replacing gain with loss and referring to Fig. 2.1(a), the loss of a fast

saturable absorber with a pulse train input is shown in Fig. 2.3(a). In addition to a background loss, the pulse generates a differential loss which depends on the local intensity. The transmission coefficient of a saturable absorber has an expression similar to the reciprocal of Eq. (2.25) and is plotted in Fig. 2.3(b). The relation between the input and output wave profiles of a fast saturable absorber can now be written as [8]

$$U_{\text{out}} = \left(\Gamma_0 + \Gamma_1 |U_{\text{in}}|^2\right) U_{\text{in}}, \tag{2.32}$$

where Γ_0 is the background loss at low intensity, and Γ_1 is the coefficient controlling the steepness of a saturable absorber. This effect is decomposed into two consecutive operators, a multiplication of U_{in} by $[1 + (\Gamma_1/\Gamma_0)|U_{\text{in}}|^2]$ and then another multiplication by Γ_0. The latter has been described before. The former multiplication becomes

$$\frac{\partial U}{\partial z} = \Gamma |U|^2 U, \tag{2.33}$$

where Γ is an amount to be determined from Eq. (2.32) and can be inferred from known physical parameters. Since phase is not involved in Eq. (2.33) and the equation is time independent, we can solve for U_{out} at $z = 1$ exactly. The result is expressed as

$$U_{\text{out}} = U(z=1) = \left(\frac{|U_{\text{in}}|^2}{1 - 2\Gamma |U_{\text{in}}|^2}\right)^{1/2} \approx \left(1 + \Gamma |U_{\text{in}}|^2\right) U_{\text{in}}. \tag{2.34}$$

We conclude that $\Gamma = \Gamma_1/\Gamma_0$.

Note that a fast saturable absorber is not necessarily a single physical item. It could be an assembly in which part of its transmission curve demonstrates fast saturable absorption as shown in Fig. 2.3(b). That is the case for the figure eight laser and fiber ring laser, as we shall describe later in this thesis.

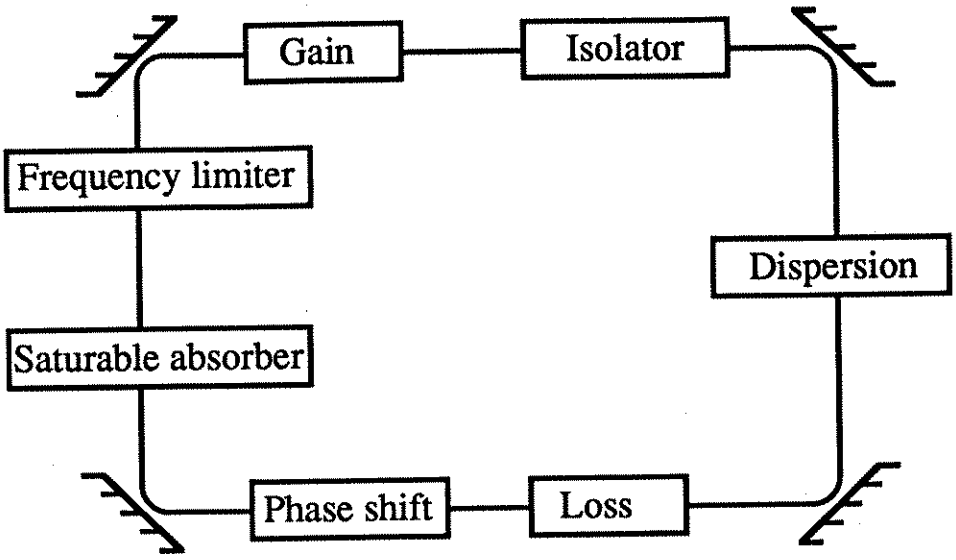

Figure 2.4: Schematic diagram of a laser cavity.

2.4 Summary

In Fig. 2.4, a possible realization of a cyclical, passively modelocked laser is shown schematically. Optical power will pass through each element, acquiring a change in pulse shape. This evolution will continue until an equilibrium is reached, or, alternatively, an equilibrium may never be reached, and the evolution will continue forever.

Combining all the effects described in Section 2.2 and Section 2.3, the corresponding laser equation is derived. In this equation, we will include in a single equation all the elements discussed in previous two sections, namely the loss in Eq. (2.7), the phase shift in Eq. (2.8), the frequency limiter in Eq. (2.13), the dispersion in Eq. (2.15), the Kerr nonlinearity in Eq. (2.20), the saturable gain in Eq. (2.27), and the fast saturable absorber in Eq. (2.33). The laser equation

is written as [14]-[24]

$$\frac{\partial U}{\partial z} = \left[g_s - l + i\theta + (B + iD)\frac{\partial^2}{\partial t^2} + (\Gamma + iK)|U|^2 \right] U. \qquad (2.35)$$

In this approximation, a single physical element may contribute to two or more of the effects on the pulse shape. The magnitude of the parameters in Eq. (2.35) is determined by summation of the contributions by all the physical elements inside the cavity. For example, the magnitude of dispersion is the sum of dispersion in fibers, mirrors, gain media, and any other dispersive elements.

We will discuss both self-starting and stability of passively modelocked lasers based on this laser equation in the next chapter.

Chapter 3

Dynamics of passive modelocking

The dynamics of a passively modelocked laser, in particular, its ability to self-start from noise and the stability of its pulsed operation mode, are studied in this chapter. We shall consider passively modelocked lasers with cyclical cavities, as shown schematically in Fig. 2.4. The laser equation Eq. (2.35) is the starting point of the discussion. In order for passively modelocked operation to self-start from noise, we assume that CW operation should be unstable while passively modelocked operation must be stable. When both are stable, the laser can be modelocked, but we assume that it will not self-start from noise. Experimental data supports this hypothesis [13]. When both the CW and modelocked states are unstable, the laser can never reach an equilibrium. Thus, the stability properties of the laser determine its dynamical evolution and ultimate operating mode. In Section 3.1, we discuss the stability of CW operation and self-starting. In Section 3.2, we discuss the stability of passively modelocked operation. In Section 3.3, we present the numerical techniques that we used to solve the eigenvalue problems which appear in Section 3.2. The beam propagation technique that is used to simulate the lasers is also introduced.

3.1 Self-starting of passively modelocked lasers

Self-starting of passively modelocked lasers with fast saturable absorption is examined in this section. In order for passive modelocking to reliably self-start from noise, the CW state of the laser should be unstable [12], [13], [25]. We will perform a stability analysis of the CW solution of the laser equation, Eq. (2.35), and determine the laser parameters which are required for self-starting.

3.1.1 The CW solution to the laser equation

Substituting

$$U = U_c \exp(iP_c z), \tag{3.1}$$

where both U_c and P_c are time independent real constants, into Eq. (2.35) and using Eq. (2.24) for the gain, the CW solution is determined by equating the real and imaginary parts. The parameters U_c and P_c are determined by the equations

$$\frac{g_0}{1 + U_c^2/P_{\text{sat}}} = l - \Gamma U_c^2, \tag{3.2}$$

$$P_c = \theta + K U_c^2. \tag{3.3}$$

The average power $P_{\text{av}} = U_c^2$ is determined from Eq. (3.2), as shown graphically in Fig. 3.1. In general, Eq. (3.2) has two possible solutions for P_{av}. The solution with the larger P_{av} value is unstable. When P_{av} is at this value and there is a small increase in U_c, then the net gain after a round trip is larger than zero and the power will increase indefinitely. Conversely, if there is a small decrease in U_c, the net gain is less than zero and the power decreases until the other solution is reached.

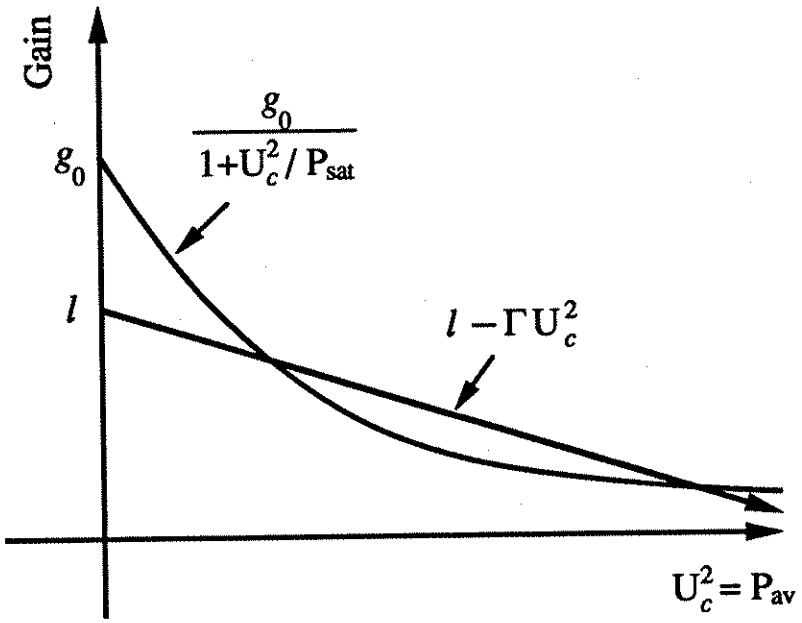

Figure 3.1: Graphic determination of the continuous wave working point.

3.1.2 Gain perturbation and the laser equation

We now study the stability of the remaining CW solution. The wave profile is written as $U = (U_c + \tilde{u})\exp(iP_c z)$, where $\tilde{u}$ is a small perturbation of the amplitude. Correspondingly, the gain deviates from g_s due to changes in the CW state. We denote $g = g_s + \delta g$. We perturb Eq. (2.22) to obtain a differential equation for δg, which may be rewritten

$$\frac{d\delta g}{dt} = -\frac{\delta g}{T_0} - \frac{U_c^2}{T_0 P_{sat}}\delta g - \frac{g_s U_c}{T_0 P_{sat}}(\tilde{u}^* + \tilde{u}). \tag{3.4}$$

Integrating the first order ordinary differential equation, Eq. (3.4), the perturbed gain, δg, is found. The full solution is

$$\delta g = \delta g_0 \exp\left(-\frac{t}{T_c}\right) - \frac{\epsilon_c}{T_c}\int_0^t (\tilde{u} + \tilde{u}^*)\exp\left(-\frac{t-t'}{T_c}\right) dt', \tag{3.5}$$

where $\delta g_0 = \delta g(t=0)$, $\epsilon_c = g_0 U_c/[(1+U_c^2/P_{sat})^2 P_{sat}]$, and $T_c = T_0/(1+U_c^2/P_{sat})$ is the effective relaxation time of the gain medium for the CW solution. Since g

is a real function of time, so is δg, which depends only on real part of $\tilde{u}$. When the perturbation is turned off, we find from Eq. (3.4) that the gain returns to a steady value with a time constant T_c. The effective relaxation time T_c is smaller than T_0, since the gain medium is partially depleted by the CW power. Since the first term in Eq. (3.5) decays exponentially, we may keep only the second term and change the lower limit to $-\infty$ for analytic convenience, which leads to

$$\delta g = -\frac{\epsilon_c}{T_c}\int_{-\infty}^{t}(\tilde{u}+\tilde{u}^*)\exp\left(-\frac{t-t'}{T_c}\right)dt'. \tag{3.6}$$

Substituting the perturbed U and g into Eq. (2.35) and keeping the first order terms, we have

$$\frac{\partial\tilde{u}}{\partial z} = \delta g U_c + (B+iD)\frac{\partial^2\tilde{u}}{\partial t^2} + (\Gamma+iK)U_c^2(\tilde{u}+\tilde{u}^*). \tag{3.7}$$

We must consider as well the complex conjugate equation, which may be written

$$\frac{\partial\tilde{u}^*}{\partial z} = \delta g U_c + (B-iD)\frac{\partial^2\tilde{u}^*}{\partial t^2} + (\Gamma-iK)U_c^2(\tilde{u}+\tilde{u}^*). \tag{3.8}$$

The evolution of a small perturbation on U_c is described by Eqs. (3.7) and (3.8).

3.1.3 The dispersion relation of the perturbation

By treating $\tilde{u}^*$ as a new variable, $\tilde{v}$, Eqs. (3.7) and (3.8) can be written as

$$\begin{aligned}
\frac{\partial\tilde{u}}{\partial z} &= U_c J(\tilde{u},\tilde{v}) + (B+iD)\frac{\partial^2\tilde{u}}{\partial t^2} + (\Gamma+iK)U_c^2(\tilde{u}+\tilde{v}),\\
\frac{\partial\tilde{v}}{\partial z} &= U_c J(\tilde{u},\tilde{v}) + (B-iD)\frac{\partial^2\tilde{v}}{\partial t^2} + (\Gamma-iK)U_c^2(\tilde{u}+\tilde{v}),
\end{aligned} \tag{3.9}$$

where J is an integral operator which may be written

$$J(\tilde{u},\tilde{v}) = -\frac{\epsilon_c}{T_c}\int_{-\infty}^{t}(\tilde{u}+\tilde{v})\exp\left(-\frac{t-t'}{T_c}\right)dt'. \tag{3.10}$$

To study the stability of U_c, we set $\tilde{u} = A_1 \exp(\lambda z + i\omega t)$ and $\tilde{v} = A_2 \exp(\lambda z + i\omega t)$, where ω is real. The integral $J(\tilde{u}, \tilde{v})$ is given by

$$\frac{\epsilon_c}{T_c} \int_{-\infty}^{t} A_k \exp(\lambda z + i\omega t) \exp\left(-\frac{t-t'}{T_c}\right) dt' = \frac{\epsilon_c}{1 + i\omega T_c} A_k \exp(\lambda z + i\omega t), \quad (3.11)$$

where $k = 1, 2$. Thus, we have transformed the evolution problem into an eigenvalue problem with λ as the eigenvalue. The resulting eigenvalue problem is

$$\begin{aligned} \lambda \begin{pmatrix} A_1 \\ A_2 \end{pmatrix} &= M \begin{pmatrix} A_1 \\ A_2 \end{pmatrix} \\ &\equiv \left[\begin{pmatrix} M_1 & M_2 \\ M_2^* & M_1^* \end{pmatrix} - \frac{U_c \epsilon_c}{1 + i\omega T_c} \begin{pmatrix} 1 & 1 \\ 1 & 1 \end{pmatrix} \right] \begin{pmatrix} A_1 \\ A_2 \end{pmatrix}, \end{aligned} \quad (3.12)$$

where $M_1 = -(B + iD)\omega^2 + (\Gamma + iK)U_c^2$ and $M_2 = (\Gamma + iK)U_c^2$. To obtain nontrivial solutions of A_1 and A_2, we must set the determinant of $\lambda I - M$ to zero. It follows that

$$\begin{aligned} \lambda &= \Gamma U_c^2 - B\omega^2 - \frac{U_c \epsilon_c}{1 + i\omega T_c} \\ &\quad \pm \left[\left(\frac{U_c \epsilon_c}{1 + i\omega T_c} - \Gamma U_c^2 \right)^2 - D^2\omega^4 + 2DKU_c^2\omega^2 \right]^{1/2}, \end{aligned} \quad (3.13)$$

which is the dispersion relation. The real part of λ at each ω determines the growth rate of the plane wave perturbation.

There are two solutions of λ for each ω, representing the two branches of solutions. When $\omega = 0$, the two eigenvalues are 0 and $2\Gamma U_c^2 - 2\epsilon_c U_c$. When $\omega \to \pm\infty$, both branches tend to the asymptotes, $-B\omega^2 + \Gamma U_c^2 \pm i(D\omega^2 - KU_c^2)$. The graph of λ on the complex plane is symmetric across the real axis, since the substitution, $\lambda \to \lambda^*$ and $\omega \to -\omega$ leaves Eq. (3.13) unchanged. The term $U_c\epsilon_c/(1 + i\omega T_c)$, which is due to the gain saturation tends to stabilize the system;

without it, the system will have eigenvalues where real part is positive when ω is close to zero. In the limit of no gain saturation, *i.e.*, when $T_0 \to \infty$, the gain saturation term disappears and $\lambda = 2\Gamma U_c^2$ at zero frequency.

3.1.4 Self-starting conditions

The condition for the laser to self-start is that λ must have a positive real part for some range of ω, corresponding to unstable CW operation. In Fig. 3.2, we plot $\lambda(\omega)$ in the complex plane for two sets of parameters whose values are shown in the figure caption. Time is measured in picoseconds and power in watts. The parameter set for Fig. 3.2(a) corresponds to a stable CW laser since $\mathrm{Re}\{\lambda\} < 0$ for all ω. However, a laser with the parameter values used in Fig. 3.2(b) does not have a stable CW solution for some values of ω and could evolve into pulses.

While Eq. (3.13) appears complicated, one can extract from it several simple rules which govern a laser's ability to self-start. First, when $\Gamma U_c > \epsilon_c$, the CW solution is unstable in the neighborhood of $\omega = 0$ and hence self-start is possible. If Γ increases, then U_c must increase in accordance with Eq. (3.2) and ϵ_c decreases from the definition following Eq. (3.5). Thus, it becomes easier for the laser to self-start. Experiments on additive-pulse modelocking [26] show that less threshold power is needed for a laser to self-start as the fiber length in the external cavity becomes larger, which corresponds to a larger Γ value in agreement with our theory.

Second, the laser self-starts more easily as T_0 increases. When T_0 increases, the term $\epsilon_c U_c/(1 + i\omega T_c)$ in Eq. (3.13), which stabilizes CW operation, becomes smaller. The effect is equivalent to reducing the gain saturation ϵ_c. This result is in agreement with the observations mentioned in ref. [13], where the authors

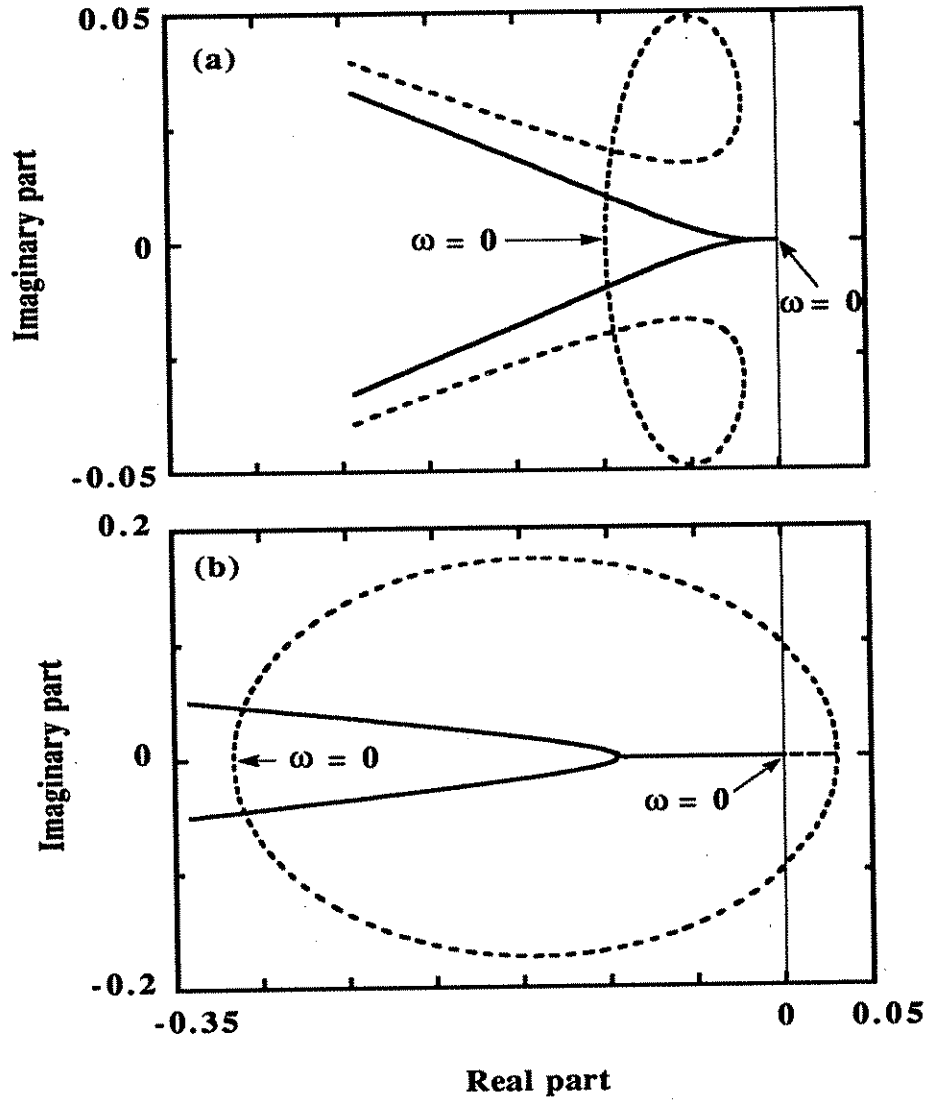

Figure 3.2: Eigenvalue λ on the complex plane. The solid line corresponds to the + branch of Eq. (3.13), while the dashed line corresponds to the − branch. (a) Non-self-starting case. Parameter values are $P_{\text{sat}} = 1$ mW, $B = 0.3$ psec^2, $D = 0.045$ psec^2, $\Gamma = 0.001$ W^{-1}, $K = 0.008$ W^{-1}, $T_0 = 1000$ psec, $g_0 = 3$ and $l = 0.05$. These parameters correspond to a Dye laser with a weak saturable absorber. (b) Self-starting case. Parameter values are $P_{\text{sat}} = 10$ mW, $B = 0.3$ psec^2, $D = 0.045$ psec^2, $\Gamma = 0.1$ W^{-1}, $K = 0.008$ W^{-1}, $T_0 = 10^8$ psec, $g_0 = 3$ and $l = 0.2$. These parameters correspond to a figure eight laser.

explain that lasers with smaller emission cross sections, σ_c, self-start more easily. From the relationship between $T_0 P_{\text{sat}}$ and σ_c in Eq. (2.23), smaller σ_c implies larger T_0 if P_{sat} is fixed. We can see this effect in Fig. 3.2(b) which is typical in shape for cases in which T_0 is large. When ω is small but ωT_c is large, the eigenvalues from Eq. (3.13) are close to 0 and $2\Gamma U_c^2$. The $-$ branch of the solution passes $2\Gamma U_c^2 - 2\epsilon_c U_c$ at $\omega = 0$, making arcs going upwards and downwards, reaching $2\Gamma U_c^2$ near the real axis, and then goes along one of the asymptotes as ω increases. Since Γ is positive for fast saturable absorbers, a laser with such a gain medium is likely to self-start. We note that the parameters in Figs. 3.2(a) and 3.2(b) correspond respectively to Dye lasers and figure eight fiber lasers. Because the gain in fiber ring lasers comes from erbium-doped optical amplifiers, which has a long relaxation time relative to gain media such as YAG, Ti:sapphire and Dye, the figure eight laser self-starts more easily than those lasers.

Third, the laser self-starts more easily as the bandwidth increases, *i.e.*, as B decreases. From Eq. (3.13), one finds that increasing B causes the eigenvalues to move toward the left hand side of the complex plane. A smaller B leads to slower movement of λ toward the left, and it is therefore easier to have a positive real part. Physically, it allows perturbations from a wider range of frequencies to exist.

Fourth, when D becomes large and positive, corresponding to large anomalous dispersion, one finds a behavior analogous to the modulational instability in the nonlinear Schrödinger equation, and the laser will self-start. Also, as K increases, the laser will self-start more easily in the anomalous regime, since the square root in Eq. (3.13) is real and increasing, so that it is easier to obtain

positive values of $\mathrm{Re}(\lambda)$.

The effect of g_0 and l on the laser's ability to self-start is rather complex. We note that in general $U_c^2 \gg P_{\mathrm{sat}}$ and $\omega T_c \gg 1$, hence, $U_c\epsilon_c/(1+i\omega T_c) \approx g_0/(i\omega T_0)$. One finds from Eq. (3.2), for fixed g_0, that when l decreases, U_c increases; however, $U_c\epsilon_c/(1+i\omega T_c) \approx g_0/(i\omega T_0)$ is almost unchanged. From Eq. (3.13), it follows that the λ-values shift toward the right hand side and hence the laser self-starts more easily. We also find that, if l is fixed, an increase in g_0 induces only a linear increase in $U_c\epsilon_c/(1+i\omega T_c)$, while the increase in ΓU_c^2 is faster than linear. Hence the traces will shift toward the right and we conclude, once again, that the laser will self-start more easily.

In Fig. 3.3, we plot the self-starting region on the g_0-l plane, given that the parameter values are $T_0 = 10^6$ psec, $P_{\mathrm{sat}} = 1$ mW, $B = 0.3$ psec^2, $D = 0.045$ psec^2, $\Gamma = 0.001$ W^{-1}, and $K = 0.008$ W^{-1}. These parameters are typical for a fiber ring laser [27]. The axes are small signal power gain, $\exp(2g_0)$ and loss, $\exp(2l)$ in decibels. As expected, a decrease in l and an increase in g_0 will make it easier for the laser to self-start. In this case, decreasing loss by a given number of dB is more effective than increasing small signal power gain by the same amount in inducing the laser to self-start.

3.2 Stability of passively modelocked lasers

The stability of passively modelocked lasers with fast saturable absorption when they are operating in pulsed mode is examined in this section. In addition to the CW solution discussed in Section 3.1, Eq. (2.35) has a pulse solution, which is the wave profile when a laser operates in pulsed mode. The parameter relations

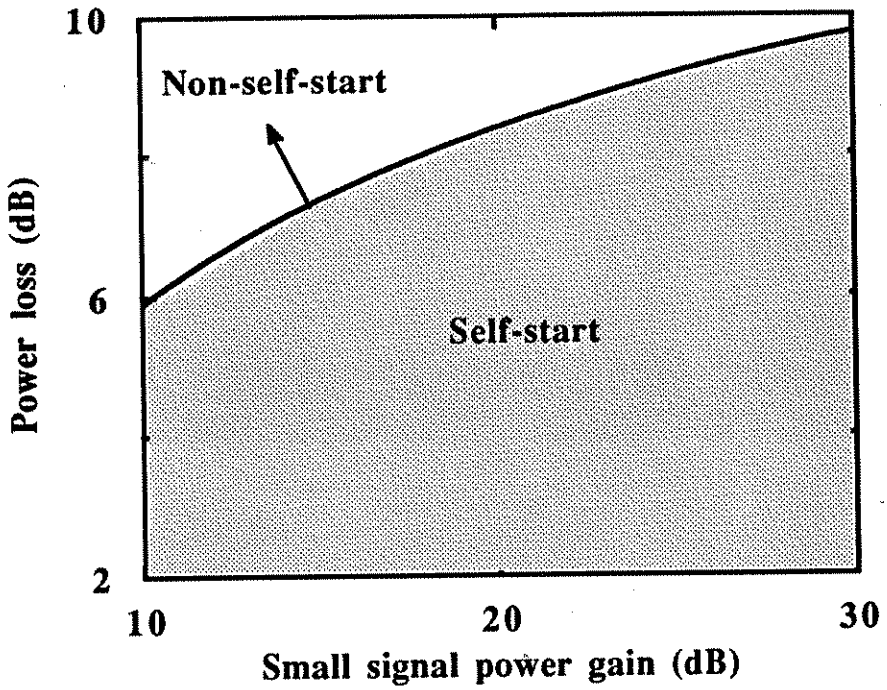

Figure 3.3: Self-starting region on the g_0-l plane. The small signal power gain is $\exp(2g_0)$. The parameter values are $T_0 = 10^6$ psec, $P_{\text{sat}} = 1$ mW, $B = 0.3$ psec^2, $D = 0.045$ psec^2, $\Gamma = 0.001$ W^{-1}, and $K = 0.008$ W^{-1}.

for this solution are first determined. We then study the stability of this solution by linearizing the equations and determining the eigenmodes and eigenvalues. It is noted that without gain saturation the pulse solution is always unstable. The effect of the gain saturation is to suppress the growth of a perturbation which tends to sharpen the modelocked pulses, so that gain saturation plays an important role in the stabilization of passively modelocked lasers.

3.2.1 The pulse solution

In addition to the CW mode of operation, the lasers of interest to us, which can be modeled by the laser equation Eq. (2.35), have a pulsed mode of operation in which the pulse shape has a hyperbolic secant amplitude profile with chirp given by

$$U_p = U_0 \exp(i\psi z) = A\,\mathrm{sech}^{1+i\beta}(t/\tau)\exp(i\psi z), \tag{3.14}$$

where A is the amplitude, τ is the pulse width, β is the chirp constant, and ψ is the wavenumber. The parameters A, τ, β, and ψ are determined by substituting Eq. (3.14) into the laser equation, Eq. (2.35), [14], [28]-[30]. Two complex equations must be satisfied. They are

$$g_s - l + i(\theta - \psi) - (\beta^2 - 2i\beta - 1)\frac{B + iD}{\tau^2} = 0, \tag{3.15}$$

$$(\Gamma + iK)A^2\tau^2 + (\beta^2 - 3i\beta - 2)(B + iD) = 0. \tag{3.16}$$

The quantities g_s, B, Γ and K are, in general, all functions of A and τ. For two of the lasers of interest to us in this thesis, the fiber ring laser and the figure eight laser with its amplifier in the external Sagnac loop, Γ and K are constants. In these two laser configurations, passive interferometric elements are used as fast saturable absorbers, whose characteristics do not depend on gain and, therefore, Γ and K do not depend on the pulse shape. Also, the bandwidth B can be treated as a constant since the bandwidth in neither ring lasers nor figure eight lasers is limited by the gain bandwidth. In figure eight lasers, the bandwidth is limited by a dispersive resonance [10]. In other lasers, Γ and K can depend upon A and τ, as, for example, in the figure eight lasers when gain is located in the loop mirror. In this case, the overall transmission curve of the loop mirror depends on gain, and hence A and τ. In this chapter, B, Γ, and K are assumed

to be constant while g_s depends on A and τ.

We begin with Eq. (3.16), which allows us to determine the values of β and $A^2\tau^2$. From Eq. (3.16), it follows that $\arg[(\beta^2-3i\beta-2)(B+iD)] = \arg(\Gamma+iK)$. Since $\arg(\beta^2 - 3i\beta - 2)$ ranges from $-\pi$ to π as β changes from $-\infty$ to ∞, β is uniquely determined. Next, we derive an equation from average power, based on Eq. (3.15). The average power of the pulse is

$$P_{\text{av}} = \frac{\int_{-\infty}^{\infty} |U|^2 dt}{T_R} = \frac{2A^2\tau}{T_R}, \tag{3.17}$$

where we are integrating over a single pulse and assuming that they are well separated. After the constant $A^2\tau^2$ is determined from Eq. (3.16), the pulse width is given by

$$\tau = \frac{2(A^2\tau^2)}{T_R P_{\text{av}}}. \tag{3.18}$$

The steady-state gain may be written

$$g_s = g_s(P_{\text{av}}) = g_s\left(\int_{-\infty}^{\infty} |U|^2 dt/T_R\right), \tag{3.19}$$

which is determined from experimental data. Using Eqs. (3.18) and (3.19), the real part of Eq. (3.15) gives

$$g_s(P_{\text{av}}) = l - \frac{c_1 T_R^2}{4(A^2\tau^2)^2} P_{\text{av}}^2, \tag{3.20}$$

where $c_1 = \text{Re}\{(1 + 2i\beta - \beta^2)(B + iD)\}$. The average power, P_{av}, can then be determined graphically as in Fig. 3.4. When we solve for all four parameters, the *ansatz* is fully determined, as are the average power and gain. We refer to this solution as working point of the laser.

In general, there are two solutions which we designate as $P_{\text{av},s}$ and $P_{\text{av},l}$ from Fig. 3.4. The solution with larger power is more likely to be unstable than the one with smaller power because when a small fluctuation in the pulse

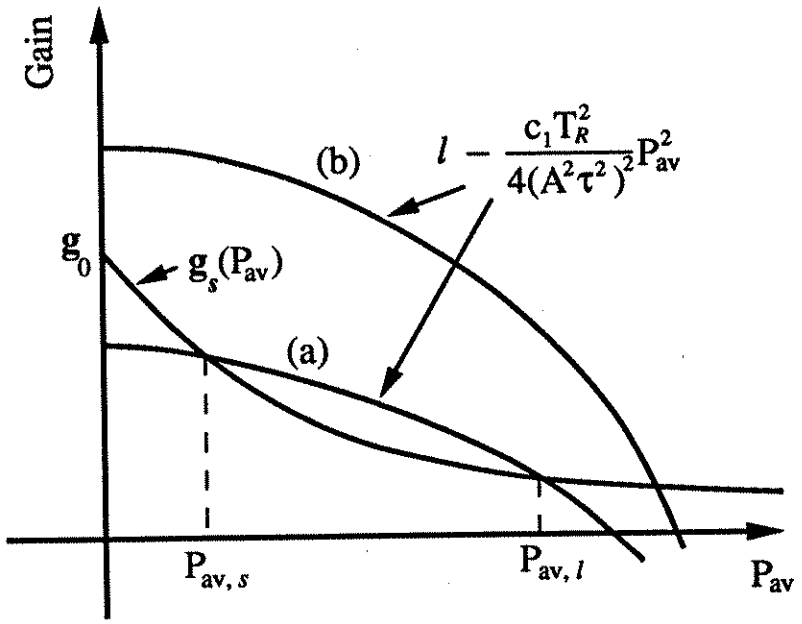

Figure 3.4: Graphic solution of the working points for pulsed mode operation.

energy increases the average power, *i.e.* $P_{av} > P_{av,l}$, the value of the gain curve, $g_s(P_{av})$ is larger than that of the loss curve from Fig. 3.4. Hence there is a net increase in the overall gain and the average power will increase further. Conversely, if the fluctuation in pulse energy leads to a decrease in the average power, *i.e.* $P_{av} < P_{av,l}$, the value of the gain curve, $g_s(P_{av})$ is smaller than that of the loss curve. There is a decrease in overall gain and the power will decrease further. Hence, this operating point is unstable. A similar argument suggests that $P_{av} = P_{av,s}$ is more likely to be stable. The above argument, however, is only heuristic. The actual effect of such a fluctuation is to cause a mismatch when Eq. (3.14) is substituted into the laser equation, Eq. (2.35). The stability of the fixed points is not obvious and has to be analyzed with more care. A fuller discussion of this issue is given in Section 3.2.5.

3.2.2 Perturbation Analysis

We now determine the stability of the pulse solution, Eq. (3.14). A perturbation of this solution can be represented as

$$U = (U_0 + \hat{u}) \exp(i\psi z), \tag{3.21}$$

where U_0 is defined in Eq. (3.14) and is z-independent and $\hat{u}$ is the perturbation. Substitution of Eq. (3.21) into Eq. (2.35) leads to the linear equation

$$\begin{aligned} \frac{\partial \hat{u}}{\partial z} = & \left[g_s - l + i(\theta - \psi) + (B + iD)\frac{\partial^2}{\partial t^2} \right] \hat{u} \\ & + (\Gamma + iK)(2|U_0|^2 \hat{u} + U_0^2 \hat{u}^*) + \delta g U_0. \end{aligned} \tag{3.22}$$

The perturbation on gain, δg_s, is derived from Eq. (3.19) and has the following form,

$$\delta g_s = \frac{g_s'(P_{\text{av}})}{T_R} \int_{-\infty}^{\infty} (U_0 \hat{u}^* + U_0^* \hat{u}) dt, \tag{3.23}$$

where g_s' is the derivative of g_s with respect to $|U|^2$ at the working point.

For easier handling of the linear evolution equation Eq. (3.22), we will introduce some new definitions and scalings. Substituting of Eqs. (3.15) and (3.16) into Eq. (3.22) and using the transformed variables

$$b_1 = \beta^2 - 2i\beta - 1, \tag{3.24}$$

$$b_2 = \beta^2 - 3i\beta - 2, \tag{3.25}$$

$$a = B/(2|D|), \tag{3.26}$$

$$s = t/\tau, \tag{3.27}$$

$$\xi = 2|D|z/\tau^2, \tag{3.28}$$

we find

$$\frac{\partial \hat{u}}{\partial \xi} = \left(a \pm \frac{i}{2}\right)\left\{b_1\hat{u} + \frac{\partial^2 \hat{u}}{\partial s^2} - b_2\left[2\mathrm{sech}^2(s)\hat{u} + \mathrm{sech}^{2+2i\beta}(s)\hat{u}^*\right]\right\}$$
$$-\epsilon_p \mathrm{sech}^{1+i\beta}(s)\int_{-\infty}^{\infty} \mathrm{sech}^{1-i\beta}(s')\hat{u} + \mathrm{sech}^{1+i\beta}(s')\hat{u}^* ds', \qquad (3.29)$$

where the + sign in the $\pm$ symbol represents anomalous intracavity dispersion, while the $-$ sign represents normal dispersion, and

$$\epsilon_p = -\frac{A^2\tau^3}{2|D|T_R} g_s'(P_{\mathrm{av}}). \qquad (3.30)$$

Since $g_s(P)$ decreases as P increases, ϵ_p has a positive value. In particular, when the steady gain, g_s, is modeled by Eq. (2.24), the formula becomes

$$\epsilon_p = \frac{A^2\tau^3 g_0}{2|D|P_{\mathrm{sat}}T_R(1 + 2A^2\tau/P_{\mathrm{sat}}T_R)^2}. \qquad (3.31)$$

Since the complex conjugate of $\hat{u}$ appears in Eq. (3.29), we must decompose Eq. (3.29) into its real and imaginary parts or, equivalently, treat $\hat{u}$ and $\hat{u}^*$ as independent variables. We shall use the latter approach and define a new independent variable $\hat{v} \equiv \hat{u}^*$. The complete set of equations governing the perturbed quantities $\hat{u}$ and $\hat{v}$ is

$$\begin{aligned}
\frac{\partial \hat{u}}{\partial \xi} &= \left(a \pm \frac{i}{2}\right)\left\{b_1\hat{u} + \frac{\partial^2 \hat{u}}{\partial s^2} - b_2\left[2\mathrm{sech}^2(s)\hat{u} + \mathrm{sech}^{2+2i\beta}(s)\hat{v}\right]\right\} \\
&\quad -\epsilon_p \mathrm{sech}^{1+i\beta}(s)\int_{-\infty}^{\infty} [\mathrm{sech}^{1-i\beta}(s')\hat{u} + \mathrm{sech}^{1+i\beta}(s')\hat{v}]ds', \\
\frac{\partial \hat{v}}{\partial \xi} &= \left(a \mp \frac{i}{2}\right)\left\{b_1^*\hat{v} + \frac{\partial^2 \hat{v}}{\partial s^2} - b_2^*\left[\mathrm{sech}^{2-2i\beta}(s)\hat{u} + 2\mathrm{sech}^2(s)\hat{v}\right]\right\} \\
&\quad -\epsilon_p \mathrm{sech}^{1-i\beta}(s)\int_{-\infty}^{\infty} [\mathrm{sech}^{1-i\beta}(s')\hat{u} + \mathrm{sech}^{1+i\beta}(s')\hat{v}]ds'.
\end{aligned} \qquad (3.32)$$

This evolution equation is turned into an eigenvalue problem by setting

$$\begin{pmatrix} \hat{u}(\xi, s) \\ \hat{v}(\xi, s) \end{pmatrix} = \exp(\lambda\xi)\begin{pmatrix} u(s) \\ v(s) \end{pmatrix}, \qquad (3.33)$$

so that Eq. (3.32) becomes

$$\begin{aligned}
\lambda u = \left(a \pm \frac{i}{2}\right) &\left\{ b_1 u + \frac{\partial^2 u}{\partial s^2} - b_2 \left[2\mathrm{sech}^2(s) u + \mathrm{sech}^{2+2i\beta}(s) v \right] \right\} \\
&- \epsilon_p \mathrm{sech}^{1+i\beta}(s) \int_{-\infty}^{\infty} [\mathrm{sech}^{1-i\beta}(s') u + \mathrm{sech}^{1+i\beta}(s') v] ds', \\
\lambda v = \left(a \mp \frac{i}{2}\right) &\left\{ b_1^* v + \frac{\partial^2 v}{\partial s^2} - b_2^* \left[\mathrm{sech}^{2-2i\beta}(s) u + 2\mathrm{sech}^2(s) v \right] \right\} \\
&- \epsilon_p \mathrm{sech}^{1-i\beta}(s) \int_{-\infty}^{\infty} [\mathrm{sech}^{1-i\beta}(s') u + \mathrm{sech}^{1+i\beta}(s') v] ds'.
\end{aligned} \tag{3.34}$$

First we consider the case in which there is no gain saturation, *i.e.*, g_s is a constant, in which case, Eq. (2.35) becomes the Ginzburg-Landau equation. The linearized Ginzburg-Landau equation can be obtained by setting $\epsilon_p = 0$ in Eq. (3.34), which yields

$$\begin{aligned}
\lambda u &= \left(a \pm \frac{i}{2}\right) \left\{ b_1 u + \frac{\partial^2 u}{\partial s^2} - b_2 \left[2\mathrm{sech}^2(s) u + \mathrm{sech}^{2+2i\beta}(s) v \right] \right\}, \\
\lambda v &= \left(a \mp \frac{i}{2}\right) \left\{ b_1^* v + \frac{\partial^2 v}{\partial s^2} - b_2^* \left[\mathrm{sech}^{2-2i\beta}(s) u + 2\mathrm{sech}^2(s) v \right] \right\}.
\end{aligned} \tag{3.35}$$

An important observation is that Eq. (3.34) depends only on β, a, and ϵ_p, while Eq. (3.35) depends only on β and a.

The linear stability criterion is that if all the eigenvalues have a negative real part, *i.e.*, $\mathrm{Re}(\lambda) < 0$, then pulsed mode operation is stable. On the other hand, if there exists some λ having positive real parts, a small perturbation which has a component of the corresponding mode will grow exponentially.

The eigenvalue problem in Eq. (3.34) cannot be solved analytically in most cases, but some special properties of the eigenvalues can still be extracted. Just as in the case of Eq. (3.13), the distribution of eigenvalues on the complex plane is symmetric with respect to the real axis. We find that if $\{\lambda, (u, v)\}$ indicates an eigenvalue λ and an eigenvector (u, v) which satisfies Eq. (3.34), then $\{\lambda^*, (v^*, u^*)\}$ also satisfies Eq. (3.34). When λ is real-valued, it is apparent

that (v^*, u^*) is a solution with the same eigenvalue, so that u and v can be chosen to be complex conjugates.

3.2.3 Radiation modes

There are both radiation modes and discrete modes which satisfy the eigenvalue problem, Eq. (3.34). The radiation modes, *i.e.*, those modes that do not vanish as ξ approaches $\pm\infty$, correspond to a continuous set of eigenvalues. These eigenvalues can be found by observing the behavior of the radiation modes as $s \to \pm\infty$. Considering the radiation modes in u, we note that $u \propto \exp(iys)$ as $s \to \pm\infty$, which implies

$$\lambda = (a \pm i/2)(b_1 - y^2), \tag{3.36}$$

where y is any real number. The result is a half-line on the complex plane which starts at $\lambda = (a \pm i/2)b_1 = (\tau^2/2|D|)[g_s - l + i(\theta - \psi)]$ when $y = 0$. Therefore, the radiation modes are stable if $g_s - l < 0$. Physically, the radiation modes represent a perturbation on the wings of the pulses. When $g_s - l < 0$, they experience a loss rather than a gain and decay as they propagate, which is consistent with the results previously reported in ref. [14]. Another half-line comes from the mode which satisfies $v \propto \exp(iys)$ as $s \to \pm\infty$. As explained earlier, the half-lines of the radiation eigenvalues must be symmetric with respect to the real axis on the complex plane. We will show a numerically generated plot of these eigenvalues later in this thesis.

The radiation modes are stable if the constraint $\mathrm{Re}\{(a \pm i/2)b_1\} = \beta^2 a - a \pm \beta < 0$ is satisfied. Since the contribution from the integral terms is locally confined, *i.e.*, u and v are multiplied by sech-functions, the integral operators do not affect the eigenvalues and eigenfunctions at large $|s|$ values. The stability

of the radiation modes is independent of the gain saturation and is determined entirely by β and a. Note that β and a are completely determined by B, D, Γ, and K through Eqs. (3.16) and (3.26). The stability regions in the β-a plane for radiation modes in both the anomalous and normal dispersion regimes are plotted in Figs. 3.5(a) and (b) respectively. In both cases, the stable regions are bounded by the curves $g_s - l = 0$.

Next we study how the stability of the radiation modes is affected by the changes in parameters. From Eq. (3.16), we find

$$\begin{aligned} (\beta^2 - 2)a \pm \frac{3}{2}\beta &= -\frac{A^2\tau^2\Gamma}{2|D|}, \\ \pm\frac{\beta^2 - 2}{2} - 3\beta a &= -\frac{A^2\tau^2 K}{2|D|}. \end{aligned} \tag{3.37}$$

Eliminating $A^2\tau^2/(2|D|)$, we obtain

$$a = \pm\frac{(\Gamma/K)(\beta^2 - 2) - 3\beta}{2\beta^2 - 2 + 3\beta(\Gamma/K)}. \tag{3.38}$$

Shown in Fig. 3.5 are the β-a curves for different values of Γ/K when D changes and other parameters are fixed. In both the anomalous and normal dispersion regimes, we find that when Γ/K is large, the curves are well within the stable region. By contrast, when Γ/K is small, *e.g.*, $\Gamma/K = 0.25$, we find that at least part of the curves is outside the stable region, and the system has unstable radiation modes. When a laser has a small Γ/K, *i.e.*, it has a weak saturable absorber, then all the radiation modes are stable if β is small in a cavity with anomalous intracavity dispersion; by contrast, β must be large in a cavity with normal dispersion. Since smaller β values correspond to pulses with smaller chirp, the pulses generated with anomalous intracavity dispersion have better quality at small Γ/K values.

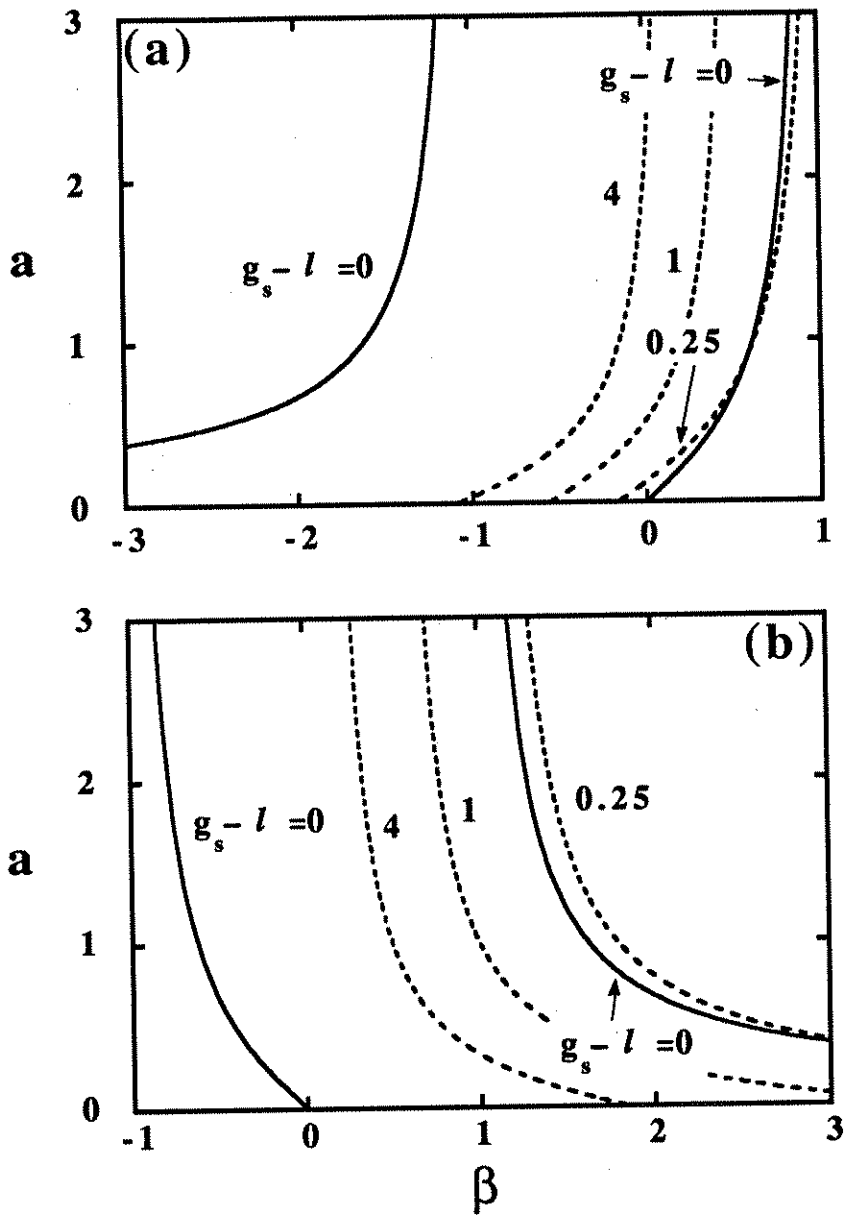

Figure 3.5: Stable regions exist between the solid curves marked by $g_s - l = 0$. The dashed curves are the traces of β and a when D changes and other parameters are fixed. Different Γ/K values are labeled for, (a) anomalous intracavity dispersion, (b) normal intracavity dispersion.

3.2.4 Discrete modes

In addition to the radiation modes, there are localized eigenfunctions that correspond to the discrete modes. Two eigenfunctions, both with $\lambda = 0$, can be found using invariant transformations of the pulse solution. A more general pulse solution is obtained by introducing an arbitrary time translation, t_0, and phase shift, ψ_0, to U_0 in Eq. (3.14), *i.e.*,

$$U_0(t, z; t_0, \psi_0) = A \operatorname{sech}^{1+i\beta}[(t - t_0)/\tau] \exp(\psi_0). \tag{3.39}$$

Both $\partial U_0(t, z; t_0, \psi_0)/\partial \psi_0$ and $\partial U_0(t, z; t_0, \psi_0)/\partial t_0$ evaluated at $t_0 = 0, \psi_0 = 0$ satisfy Eq. (3.34) with $\lambda = 0$. Explicitly, they may be written

$$u_{\text{even}} = i \operatorname{sech}^{1+i\beta}(s), \tag{3.40}$$

and

$$u_{\text{odd}} = (1 + i\beta) \tanh(s) \operatorname{sech}^{1+i\beta}(s). \tag{3.41}$$

Since both u_{even} and u_{odd} are orthogonal to the integral operators in Eq. (3.34), both u_{even} and u_{odd} are also eigenfunctions to Eq. (3.35) with $\lambda = 0$. By the same observation, we conclude that an odd eigenfunction of Eq. (3.35) is also an eigenfunction of Eq. (3.34) with arbitrary ϵ_p values.

We will present more analytical results regarding the unstable discrete mode in the rest of this section and Section 3.2.5. It is usually not possible to find analytical expressions for the discrete eigenmodes, other than u_{even} and u_{odd}. We can, however, solve Eq. (3.35) by making series expansion. Using the series expansion method to find eigenvalues of Eq. (3.35) over the β-a plane, we find that there is a tradeoff between the stability of the discrete modes and the radiation modes, so that if the radiation modes are stable, then one of the discrete

modes is always unstable, and vice versa. By treating the integral operator in Eq. (3.34) as a perturbation to Eq. (3.35), we are able to show that the gain saturation shifts the most unstable eigenvalue and stabilizes the laser system. We show that an $\epsilon_p > \epsilon_{p,\min}$ is needed to stabilize a modelocked laser and give a formula for $\epsilon_{p,\min}$. In Section 3.2.5, we discuss the stability of modelocked lasers which have constant B, D, Γ, and K, based on the $\epsilon_{p,\min}$ formula.

The most unstable eigenmode of Eq. (3.35) can be obtained by a series expansion, assuming that there is a real eigenvalue for given β and a values, an assumption which is consistent with what we have found from a complete numerical solution of Eq. (3.35). When λ is real, we may choose $v = u^*$ without loss of generality. The series expansion for even u is written as

$$u = \operatorname{sech}^{1+i\beta}(s)[c_0 + c_2 \tanh^2(s) + \cdots]. \tag{3.42}$$

An algorithm for calculating λ and the coefficients $c_0, c_2, \cdots$ is given in Appendix A. We obtain a recursion relation for the coefficients and use this relation to calculate their values as well as the eigenvalue. We typically calculate on the order of a hundred coefficients, which yields an eigenvalue and an eigenfunction which are accurate to more than four places. For example, with $\beta = 0.4$, $a = 0.52$, and using 101 terms, we obtain $\lambda = 0.1656$ and the eigenfunction plotted in Fig. 3.6. As a test of the accuracy of the solution, we substitute this eigenvalue and eigenfunction into Eq. (3.35). The magnitude of the error, estimated as the difference between the right and left sides of Eq. (3.35), is less than 3×10^{-5} uniformly over s axis.

We have calculated the eigenvalues of Eq. (3.35) inside the stability region on the β-a plane for both signs of D. Our findings can be summarized as follows: In most cases, eigenvalues corresponding to bounded modes are real. There always

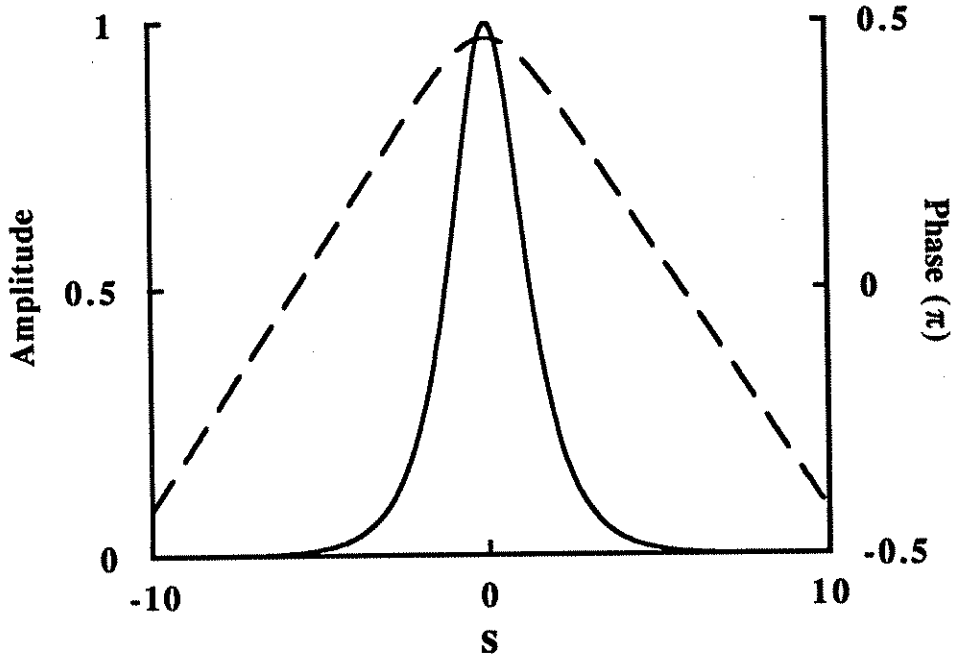

Figure 3.6: The eigenfunction that corresponds to the unstable mode which is also shown in Fig. 3.8(a). The eigenvalue is $\lambda = 0.1656$. The amplitude is shown as a solid line, and the phase is shown as a dashed line.

exists a discrete eigenvalue on the right hand side of the complex plane, which means that a modelocked laser without gain saturation is always unstable. There is a tradeoff between the stability of the radiation modes and the stability of the bounded modes. We observe that as we choose parameters close to the $g_s - l = 0$ boundary, the eigenvalue for the unstable bounded mode moves closer to zero. Once we pass the $g_s - l = 0$ boundary, *i.e.*, we are inside the region in which the radiation modes are unstable, the unstable bounded mode becomes stable.

Treating the gain saturation as a perturbation, we can estimate the shift of the eigenvalue due to gain saturation. To do so, we must solve the eigenvalue

problem which is adjoint to Eq. (3.35),

$$\lambda u^a = \left(a \mp \frac{i}{2}\right)\left[b_1^* u^a + \frac{\partial^2 u^a}{\partial s^2} - 2b_2^* \mathrm{sech}^2(s) u^a\right] - \left(a \pm \frac{i}{2}\right) b_2 \left[\mathrm{sech}^{2+2i\beta}(s) v^a\right],$$
$$\lambda v^a = \left(a \pm \frac{i}{2}\right)\left[b_1 v^a + \frac{\partial^2 v^a}{\partial s^2} - 2b_2 \mathrm{sech}^2(s) v^a\right] - \left(a \mp \frac{i}{2}\right) b_2^* \left[\mathrm{sech}^{2-2i\beta}(s) u^a\right], \tag{3.43}$$

where the superscript a denotes the adjoint. This adjoint eigenvalue problem is similar to the original eigenvalue problem, Eq. (3.35), in its appearance. Again, when λ is a real number, one can set $v^a = u^{a,*}$ and solve for the eigenvalues and eigenfunctions using the series expansion approach in Appendix A. The spectrum of Eq. (3.43) is symmetric with respect to the original eigenvalue problem about the real axis. Since the original spectrum is symmetric around the real axis, both eigenvalue problems have an identical spectrum. From first order perturbation theory, the first order shift, $\Delta\lambda$, in the eigenvalue can be written as

$$\Delta\lambda = -\epsilon_p \frac{\langle (u^a, v^a), I(u,v) \rangle}{\langle (u^a, v^a), (u,v) \rangle}, \tag{3.44}$$

where $\langle \cdot, \cdot \rangle$ is the inner product and I is the integral operator excluding the factor of $-\epsilon_p$ in Eq. (3.34). Since the shift in the eigenvalue is proportional to ϵ_p, there exists a minimum gain saturation which is required to stabilize the modelocked laser—an $\epsilon_{p,\mathrm{min}}$ such that the shift in λ is large enough to move the eigenvalue to the imaginary axis, or, $\Delta\lambda = -\lambda$. The perturbation method generally gives a good estimate on $\epsilon_{p,\mathrm{min}}$. For instance, using $\beta = 0.4$ and $a = 0.5$, we obtain an $\epsilon_{p,\mathrm{min}} = 0.0359$ while the exact value of 0.0368 is obtain from an analytical expression of $\epsilon_{p,\mathrm{min}}$ later in this section. This method continues to work well when the laser configuration is changed and parameters such as Γ and K are not constant, as, for example, in the figure eight laser with gain in the loop mirror. In this case, it is not possible to obtain an analytic expression.

Next, we investigate the solution to the eigenvalue problems, Eqs. (3.34) and (3.35) given particular β and a relations. First, we will confirm the tradeoff between radiation modes and discrete modes mentioned above by showing that when $g_s - l = 0$, the eigenvalue corresponding to the unstable mode is zero. Two eigenfunctions for $\lambda = 0$ have already been found in Eqs. (3.40) and (3.41) for arbitrary β and a values. When $g_s - l = 0$, *i.e.*, on the boundary at which some radiation modes become unstable, shown in Fig. 3.5, $a = \pm\beta/(1-\beta^2)$ and $(a \pm i/2)b_1 = \mp i|b_1|^2/[2(1-\beta^2)]$. Using the function

$$u_0 = [1 - (1 + i\beta)s\tanh(s)]\mathrm{sech}^{1+i\beta}(s), \tag{3.45}$$

which is Eq. (B.8) discussed in Appendix B, we obtain the equation

$$\left(a \pm \frac{i}{2}\right)\left(b_1 u_0 + \frac{\partial^2 u_0}{\partial t^2} - 2b_2\mathrm{sech}^2(s)u_0 - b_2\mathrm{sech}^{2+2i\beta}(s)u_0^*\right) = \pm i\frac{|b_1|^2}{1-\beta^2}\mathrm{sech}^{1+i\beta}(s). \tag{3.46}$$

The right hand side equals the eigenfunction u_{even} multiplied by a real factor $\pm|b_1|^2/(1-\beta^2)$. We rewrite Eq. (3.46) as

$$\mathcal{P}\left(\pm\frac{1-\beta^2}{|b_1|^2}\right)u_0 = u_{\mathrm{even}}, \tag{3.47}$$

where the operator on the left hand side of Eq. (3.46), denoted as $\mathcal{P}$, is the linearized Ginzburg-Landau operator in Eq. (3.35) at $\lambda = 0$. Two other equations valid for zero eigenvalue solutions are $\mathcal{P}u_{\mathrm{even}} = 0$ and $\mathcal{P}u_{\mathrm{odd}} = 0$. We thus conclude that when $g_s - l = 0$, the diagonalization of the subspace of the linear operator in Eq. (3.35) at $\lambda = 0$ will lead to

$$\begin{pmatrix} 0 & 1 & 0 \\ 0 & 0 & 0 \\ 0 & 0 & 0 \end{pmatrix}\begin{pmatrix} x_1 \\ x_2 \\ x_3 \end{pmatrix}, \tag{3.48}$$

where x_1, x_2, and x_3 are the coordinates of the three functions, $u_{\text{even}}, [\pm(1-\beta^2)/|b_1|^2]u_0$, and u_{odd}, respectively. It is in Jordan canonical form and the multiplicity is 3. Hence, the previously unstable bound mode is now located at $\lambda = 0$.

We have verified the following: When (β, a) is inside the stability regions for the radiation modes shown in Fig. 3.5, there always exists an unstable bound mode. As (β, a) approaches $g_s - l = 0$, the unstable eigenvalue approaches zero and becomes zero exactly when the boundary is reached. The laser is therefore marginally stable at $g_s - l = 0$. Then, the unstable discrete mode becomes stable, but unstable radiation modes appear if (β, a) moves outside the stability region for the radiation modes. A mode locked laser system is therefore always unstable or marginally stable without gain saturation.

With gain saturation, the same function u_0 in Eq. (3.45) can be used to calculate $\epsilon_{p,\text{min}}$, which is

$$\epsilon_{p,\text{min}} = -\text{Re}\{(a \pm i/2)b_1\} = \frac{\tau^2}{2|D|}(l - g_s), \tag{3.49}$$

and based on this formula, accurate contour plots can be generated.

To demonstrate that Eq. (3.49) holds, we set $\epsilon_p = \epsilon_{p,\text{min}}$, given by Eq. (3.49), and we substitute $u = v^* = u_0$ into the right hand side of Eq. (3.34), obtaining

$$\begin{aligned}\left(a \pm \frac{i}{2}\right)\left\{b_1 u_0 + \frac{\partial^2 u_0}{\partial s^2} - b_2\left[2\text{sech}^2(s)u_0 + \text{sech}^{2+2i\beta}(s)u_0^*\right]\right\} \\ -\epsilon_p \text{sech}^{1+i\beta}(s)\int_{-\infty}^{\infty}[\text{sech}^{1-i\beta}(s')u_0 + \text{sech}^{1+i\beta}(s')u_0^*]ds' \\ = -2i\,\text{Im}\left\{\left(a \pm \frac{i}{2}\right)b_1\right\}\text{sech}^{1+i\beta}(s).\end{aligned} \tag{3.50}$$

Again, the right hand side is proportional to u_{even}. The proportionality factor is

$-2\mathrm{Im}\{(a \pm (i/2))b_1\} = 4a\beta \mp (\beta^2 - 1)$. We rewrite Eq. (3.50) as

$$\mathcal{Q}\left(\pm\frac{1}{4a\beta \mp (\beta^2 - 1)}\right) u_0 = u_{\mathrm{even}}, \tag{3.51}$$

where we denote the operator on the left hand side of Eq. (3.50) by $\mathcal{Q}$, corresponding to the operator in Eq. (3.34) with $\epsilon_p = \epsilon_{\mathrm{p,min}}$. Both $u_{\mathrm{even}} = 0$ and $u_{\mathrm{odd}} = 0$ are in the null space of $\mathcal{Q}$. The subspace corresponding to the operator in Eq. (3.34) at $\lambda = 0$ is 3-dimensional. A Jordan canonical form which is identical to Eq. (3.48) arises when we try to diagonalize this linear operator at $\lambda = 0$. The coordinate components x_1, x_2, and x_3 now refer to $u_{\mathrm{even}}, 1/[4a\beta \mp (\beta^2 - 1)]u_0$, and u_{odd} respectively. Since the modelocked lasers always have an unstable eigenvalue for $\epsilon_p = 0$, the unstable eigenvalue is shifted to the origin of the complex plane when $\epsilon_p = \epsilon_{p,\mathrm{min}}$. When ϵ_p increases further, the eigenvalue of the previously unstable mode shifts further to the left, and the laser is stable.

In Fig. 3.7, we plot the minimum ϵ_p value, $\epsilon_{p,\mathrm{min}}$, needed to stabilize the system by showing contours of fixed $\epsilon_{p,\mathrm{min}}$ on β-a plane. The anomalous intracavity dispersion case is shown in Fig. 3.7(a), and the normal intracavity dispersion case is shown in Fig. 3.7(b). For example, with anomalous intracavity dispersion, and setting $\beta = 0.5$ and $a = 1.6$, we need ϵ_p larger than 0.7 to make the modelocked laser stable. Higher values of ϵ_p than the minimum are always able to stabilize the modelocked laser.

3.2.5 Bounds for ϵ_p and their implications

When Γ and K are constant, the case being considered in this chapter, we may estimate the values of ϵ_p in Eq. (3.30). Two solutions of P_{av} are found from Fig. 3.4 and $g_s'(P_{\mathrm{av},s})$ and $g_s'(P_{\mathrm{av},l})$ are the derivatives at these two working points.

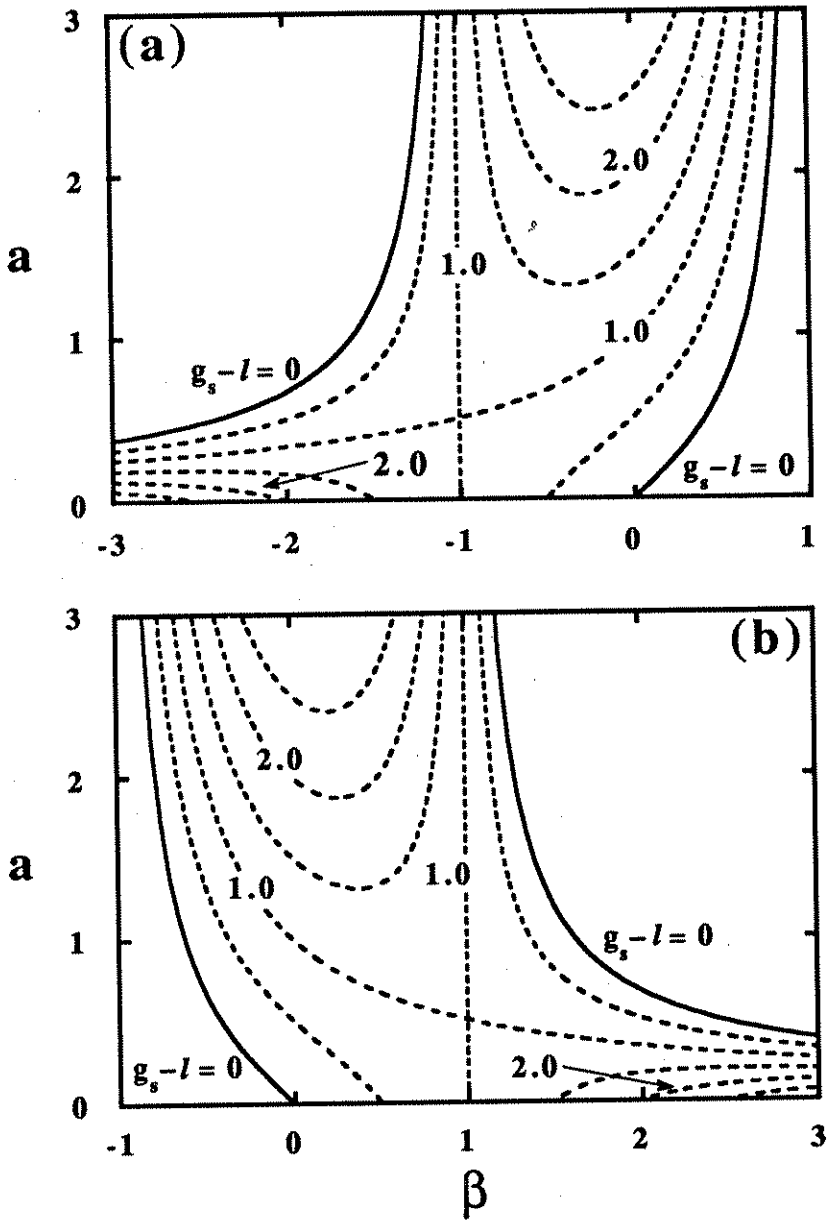

Figure 3.7: Contour plots of the minimum ϵ_p value needed to stabilize the mode-locked laser. (a) Anomalous intracavity dispersion. (b) Normal intracavity dispersion. The solid lines indicate the stability boundary, $g_s - l = 0$.

These slopes are negative numbers and satisfy the following inequalities,

$$g_s'(P_{\mathrm{av},s}) < -\frac{c_1 T_R^2 P_{\mathrm{av},s}}{2(A^2\tau^2)^2}, \tag{3.52}$$

$$g_s'(P_{\mathrm{av},l}) > -\frac{c_1 T_R^2 P_{\mathrm{av},l}}{2(A^2\tau^2)^2}. \tag{3.53}$$

The right hand sides of the inequalities, Eqs. (3.52) and (3.53), are from the derivative of the right hand side of Eq. (3.20). From definition of ϵ_p in Eq. (3.30), these two inequalities give bounds on ϵ_p. Applying Eq. (3.17) for P_{av} and the definition of c_1 in Eq. (3.20), the right hand sides of the inequalities are equal and the value is $-\mathrm{Re}\{(a + i/2)b_1\}$ or $\epsilon_{p,\mathrm{min}}$! The inequalities become

$$\epsilon_{p,s} > \epsilon_{p,\mathrm{min}}, \tag{3.54}$$

$$\epsilon_{p,l} < \epsilon_{p,\mathrm{min}}. \tag{3.55}$$

The implication is that if two working points exist as shown in curve (a) in Fig. 3.4, the one with the smaller average power is always stable, while the other one with larger average power is always unstable. Similar results were reported by Haus in a different setting [8]. If there are no intersections as shown in curve (b) in Fig. 3.4, there are no stable working points for pulsed operation since Eq. (3.55) applies. The conclusion is independent of the input power versus output power gain characteristic as long as the relaxation time, T_0, of the gain medium is large and the gain depends only on average power. When the assumptions that Γ and K are constant and g_s is a function of average input power do not hold, as, for example, in a figure eight laser with gain in the Sagnac mirror, a more delicate gain model has to be used.

3.3 Numerical approaches

We present the numerical approach that we used to solve the eigenvalue problems. We also describe the numerical method that we used to carry out laser simulations. We use a finite difference method to solve the eigenvalue problem, Eqs. (3.34) and (3.35) in Section 3.3.1. By transforming the eigenvalue problem into a matrix form, we are able to easily solve for the eigenvalues of both the radiation and discrete modes. With today's high speed computers and eigenvalue solvers, this approach is efficient and accurate. We will compare this approach to the available analytical results.

In Section 3.3.2, we discuss the beam propagation method which we use to simulate the complete evolution equation, Eq. 2.3, using difference operators, which describe the evolution through the physical media. If the operator involves the solution of partial differential equations, as is the case in optical fibers, then we use the beam propagation method.

3.3.1 Eigenvalue problem

We may use a finite difference method to solve the eigenvalue problem in Eqs. (3.34) and (3.35) [31]. Since the hyperbolic secant function decays exponentially, we typically choose a computational window from $s = -40$ to $s = 40$, where $\mathrm{sech}(s)$ is on the order of 10^{-17}. The eigenfunction (u, v) is sampled and represented as a column vector $[u_1, \cdots, u_n, v_1, \cdots, v_n]^t$, where n is the number of points sampled. The differential, the integral, and the multiplication operators are represented as matrices. The second order differential operator is approximated by a five-point formula, which yields fourth order accuracy in the

discretization parameters. For example, at the i-th point

$$u_i'' = \left(-\frac{1}{12}u_{i-2} + \frac{4}{3}u_{i-1} - \frac{5}{2}u_i + \frac{4}{3}u_{i+1} - \frac{1}{12}u_{i+2}\right) \Big/ \Delta s^2, \tag{3.56}$$

where Δs is the sampling interval. At the left end of the calculation window, the following formulae are used

$$u_1'' = \left(\frac{35}{12}u_1 - \frac{26}{3}u_2 + \frac{19}{2}u_3 - \frac{14}{3}u_4 + \frac{11}{12}u_5\right) \Big/ \Delta s^2, \tag{3.57}$$

$$u_2'' = \left(\frac{11}{12}u_1 - \frac{5}{3}u_2 + \frac{1}{2}u_3 + \frac{1}{3}u_4 - \frac{1}{12}u_5\right) \Big/ \Delta s^2. \tag{3.58}$$

Similar formulae are used at the right end of the calculation window. The integrals in Eq. (3.34) are approximated as finite sums. As an example, we use

$$\int_{-\infty}^{\infty} \mathrm{sech}^{1-i\beta}(s')u ds' \approx \sum_{m=1}^{n} \mathrm{sech}^{1-i\beta}(s_m')u_m \Delta s. \tag{3.59}$$

Combined with the function, $\mathrm{sech}^{1+i\beta}(s)$, in front of the integral, this part of the equation is represented by

$$\mathrm{sech}^{1+i\beta}(s) \int_{-\infty}^{\infty} \mathrm{sech}^{1-i\beta}(s')u ds' \approx$$
$$\left\{[\cdots, \mathrm{sech}^{1+i\beta}(s_m'), \cdots]^t[\cdots, \mathrm{sech}^{1-i\beta}(s_m'), \cdots]\Delta s\right\}[u_1, \cdots, u_n]^t. \tag{3.60}$$

Using Eqs. (3.56) to (3.60), Eq. (3.34) is transformed to a matrix eigenvalue problem. Many standard eigenvalue solvers are capable of calculating the eigenvalues and eigenvectors of the matrix with high accuracy and efficiency [31]. Typical sampling sizes are $n = 300$ and 600.

In Fig. 3.8, we show the distribution of λ calculated numerically on the complex plane. To show how the gain saturation affect the stability, we have studied both Eq. (3.34) and Eq. (3.35). In Fig. 3.8(a), we show a typical distribution of eigenvalues for Eq. (3.35) are shown. The parameters that we used are $\beta = 0.4$

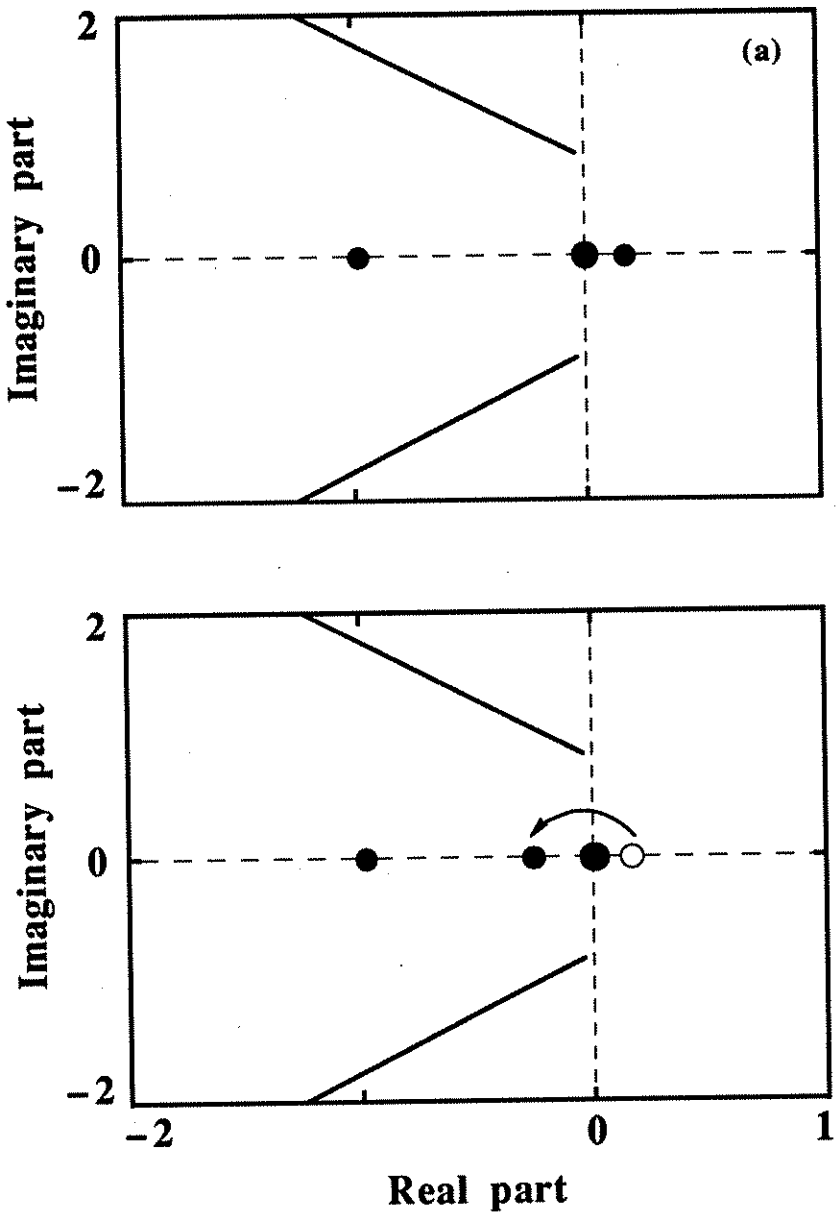

Figure 3.8: Eigenvalues of the linearized equation are shown in the complex λ-plane when $\beta = 0.4$ and $a = 0.52$. The two solid half-lines correspond to radiation modes and the dots to discrete modes. (a) Without gain saturation, $\epsilon_p = 0$, (b) With gain saturation, $\epsilon_p = 0.1$.

and $a = 0.52$, corresponding to a fiber ring laser. The two solid half-lines correspond to radiation modes and agree well with Eq. (3.36) and its complex conjugate. In addition to the radiation modes, there exist discrete modes which are plotted as dots. The eigenvalue at zero has a multiplicity of 2, which are the two eigenfunctions, u_{even} and u_{odd}, described in Eqs. (3.40) and Eq. (3.41). The mode on the right hand side of the λ-plane is not stable and therefore a mode locked laser with this set of parameters has an unstable pulsed mode operation. In Fig. 3.8(b), β and a are the same as in Fig. 3.8(a) and ϵ_p is 0.1. Comparing Fig. 3.8(a) and (b), the unstable discrete eigenvalue is shifted to the left hand side of the complex plane and, therefore, pulsed mode operation is stable. In general, as noted in Section 3.2, the effect of gain saturation is to stabilize the system. Larger values of ϵ_p imply a larger shift of the eigenvalue of the most unstable discrete mode, which is even. By contrast, the eigenvalues of the radiation modes are not affected. Also, the eigenvalues corresponding to odd eigenfunctions will not be shifted since they are orthogonal to the perturbation. The two eigenfunctions u_{even} and u_{odd} must of course remain eigenfunctions with zero eigenvalue at any ϵ_p.

We check the accuracy of the numerical method in several ways. First, the eigenvalues of the two eigenfunctions u_{even} and u_{odd} are zero and the numerical results are within 10^{-4}. The discrete eigenvalues are compared with the results from the series expansion and the error is again within 10^{-4}. The accuracy of the radiation eigenvalues is not as good primarily due to the finite size of the sampling window. This situation is improved when the window size and the number of sampling points is increased. The error in this case is about 10^{-2}.

We verify numerically the tradeoff between the stability of the radiation

modes and of the discrete modes described in Section 3.2.4. When β and a are on the $g_s - l = 0$ boundary, there are three eigenvalues at zero and the laser is marginally stable. We have also verified the minimum ϵ_p given analytically in Section 3.2.4 by use of the numerical method. Using $\epsilon_{p,\min}$ from Eq. (3.49) in the eigenvalue problem, Eq. (3.34), we find three eigenvalues at zero.

The numerical method is particularly useful when the laser configuration leads to an equation in which analytical or perturbation estimates of λ are not available. A practical example is when the coefficients in Eq. (2.35) are not constant, as in the case of a figure eight laser with gain in the Sagnac mirror, whose Γ and K parameters are gain dependent.

3.3.2 Beam propagation method

The purpose of the beam propagation method is to solve Eq. (2.5). For simplicity, we will discuss the beam propagation method, assuming that it is applied to an evolution equation with two operators.

Suppose that an evolution equation,

$$\frac{\partial U(z,t)}{\partial z} = \mathcal{O}U(z,t), \tag{3.61}$$

is to be solved given the initial wave profile $U(0,t)$. Next, assume that this equation can be decomposed into two operators, *i.e.*,

$$\frac{\partial U(z,t)}{\partial z} = (\mathcal{O}_1 + \mathcal{O}_2)U(z,t), \tag{3.62}$$

such that

$$\frac{\partial U(z,t)}{\partial z} = \mathcal{O}_k U(z,t), \tag{3.63}$$

where $k = 1, 2$ can be solved exactly and efficiently. To second order accuracy, advancing the pulse profile by one small step $\Delta\xi$ can be approximated by prop-

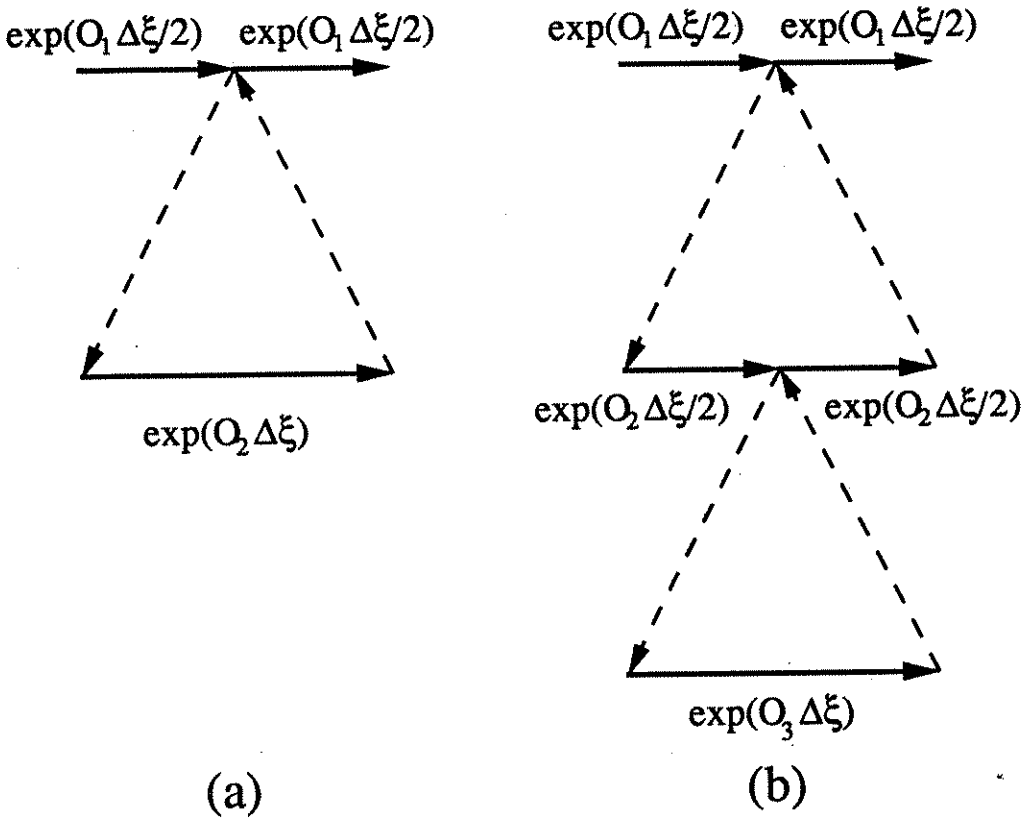

Figure 3.9: Graphical representation of the beam propagation method when (a) two operators appear, and (b) three operators appear.

agating a half step just using $\mathcal{O}_1$ to operate on U, then propagating a full step just using $\mathcal{O}_2$ to operate on U, and then finally, propagating a half step just using $\mathcal{O}_1$. Formally, this procedure is represented by the equation,

$$\exp[(\mathcal{O}_1 + \mathcal{O}_2)\Delta\xi] = \exp\left(\mathcal{O}_1\frac{\Delta\xi}{2}\right)\exp(\mathcal{O}_2\Delta\xi)\exp\left(\mathcal{O}_1\frac{\Delta\xi}{2}\right) + o(\Delta\xi^3). \quad (3.64)$$

In Fig. 3.9, we show a graphical representation of this procedure. We also show the iteration when three operators appear. Since in practice one of the operators is always a differential operator that can be solved by using the Fourier transform technique, the beam propagation method is also referred to as the split step semi-spectral method [32].

We primarily use the beam propagation method to calculate the evolution of the pulse shape in fibers when we simulate a figure eight laser or a fiber ring laser. The wave propagation inside a optical fiber is modeled by the nonlinear Schrödinger equation or the coupled nonlinear Schrödinger equation, which is of the form of Eq. (3.62) and is solvable by the beam propagation method.

The growth rate of the unstable discrete mode of Eq. (3.29) when $\epsilon_p = 0$ is found by using the beam propagation method and then comparing to the theoretical growth rate obtained by finding the eigenvalues of Eq. (3.35). The initial pulse profile is set to that of the unstable discrete mode, which is obtained from the series expansion method. The theoretical energy growth rate of this initial profile is $\exp[2\mathrm{Re}(\lambda)\xi]$, where λ is the corresponding eigenvalue. We find the agreement in the growth rates is within 10^{-3}.

3.4 Summary

The stability of both CW and pulsed mode operation are discussed using the same laser equation, Eq. (2.35). We assume that pulsed mode operation will only self-start from noise if CW operation is unstable and pulsed mode operation is stable. We discuss the conditions for a laser to self-start. Generally, increases in the magnitudes of the relaxation time, bandwidth, dispersion, saturable absorption, Kerr nonlinearity, and small signal gain, and decreases in the loss will facilitate self-starting. We plotted the parameter regime in which a laser can self-start on the loss-gain plane.

The stability of the pulsed mode operation is determined by the stability of the radiation eigenmodes and the discrete modes. We found that the radiation is

stable when $g_s - l < 0$, and discrete modes are stable when $\epsilon_p > \epsilon_{p,\min}$. We found that gain saturation is essential to stabilize a modelocked laser since without gain saturation, there is always an unstable discrete mode when all radiation modes are stable.

Numerical methods play an important role. By transforming the eigenvalue problem into a matrix eigenvalue problem, we obtain all eigenvalues of the linearized equation with efficiency and accuracy. A full numerical simulation of lasers can be performed by using the beam propagation method, which is able to calculate the evolution of the pulse shape when the initial wave profile is given.

Chapter 4

Figure Eight Laser

One of the key difficulties in building a passively modelocked laser with fast saturable absorption is finding fast saturable absorbers! For a laser pulse with a duration on the order of a picosecond, only a few materials demonstrate fast saturable absorption. Present fast saturable absorbers are made from a dye jet [33] or a multiple quantum well [34]. However, these components are frequency dependent or subject to material degradation after a period of time. It is also difficult to adjust parameters with these materials. In Sections 4.1 and 4.2, we introduce nonlinear, optical fiber loop mirrors and nonlinear, optical fiber amplifying loop mirrors as interferometric devices that act as saturable absorbers when certain parameter values are properly chosen [35]. The Kerr nonlinearity, which has a response time on the order of femtoseconds, plays a key role in the saturable absorption, so that it is very fast acting.

A laser using a nonlinear amplifying loop mirror as a gain and pulse shaping component was first introduced into a ring laser cavity by Dr. Irl N. Duling at the Naval Research Laboratory [36], [37]. The structure and analysis of the laser are discussed in Section 4.3. We simulated the figure laser in a modular fashion,

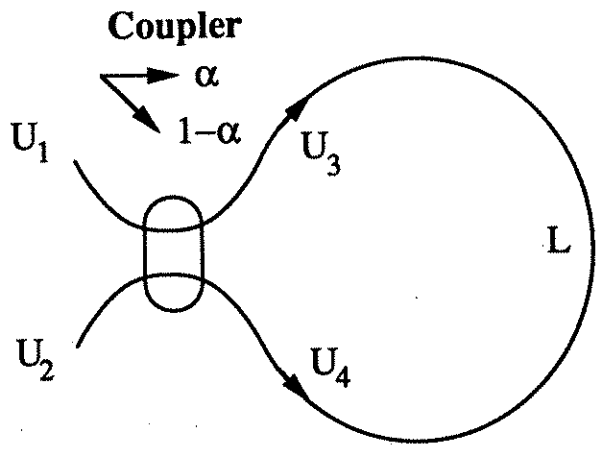

Figure 4.1: The structure of a nonlinear loop mirror.

and the results are presented in Section 4.4. A summary is given in Section 4.5.

4.1 Nonlinear loop mirrors as fast saturable absorbers

A nonlinear loop mirror is basically a Mach-Zehnder interferometer [38]. As shown in Fig. 4.1, it consists of a coupler or a beam splitter and a fiber that is connected to both output ends of the coupler or beam splitter. After the coupler, the separated light waves propagate in opposite directions through the loop, and their paths are obviously identical. They interfere at the coupler again and generate reflected and transmitted waves. In the laser that we are going to discuss, only the transmitted wave are used and the reflected wave are blocked by an isolator in the laser cavity. This combination has zero transmission when the coupler is a 50/50 splitter since the same wave profiles travel through an

identical waveguide and cancel each other at the output end. However, when the splitter is not 50/50, optical power propagating in each direction of the fiber is different, and the relative phase shift in the two propagation directions changes with the power difference and the length of the loop due to the Kerr effect. Constructive instead of destructive interference at the output end may occur if the phase difference is close to π.

4.1.1 Quasi-CW inputs

To understand the behavior of the loop mirror we consider a quasi-CW input to the nonlinear loop mirror. By quasi-CW input we mean a segment of CW input which is long enough to be considered continuous, *i.e.*, has no significant dispersion, but is shorter than the time of passage through the loop mirror so that the overlap of different directions of propagation is not significant and not taken into account. The coupler can then be described by the scattering equation [38],

$$\begin{aligned} U_3 &= \alpha^{1/2} U_1 + i(1-\alpha)^{1/2} U_2, \\ U_4 &= i(1-\alpha)^{1/2} U_1 + \alpha^{1/2} U_2, \end{aligned} \tag{4.1}$$

where α is the power coupling ratio of the coupler and U_1, U_2, U_3, and U_4 are wave amplitudes as indicated schematically in Fig. 4.1.

The Kerr nonlinearity inside the fiber will affect the optical length of each propagation direction as described in Section 2.2. From Eq. (2.21), the phase change, ϕ_{NL}, due to the Kerr nonlinearity is

$$\phi_{\mathrm{NL}} = \frac{2\pi n_2 L_{\mathrm{fiber}}}{\lambda_0 A_{\mathrm{eff}}} |U|^2 = K_s |U|^2, \tag{4.2}$$

From Eqs. (4.1) and (4.2) and the loop mirror topology shown in Fig. 4.1, the

output field can be calculated and, hence, the transmission coefficient. When the input is quasi-CW with $U = U_{\text{in}}$, the output is

$$U_{\text{out}} = \alpha U_{\text{in}} \exp(i\alpha K_s |U_{\text{in}}|^2) - (1-\alpha) U_{\text{in}} \exp(i(1-\alpha) K_s |U_{\text{in}}|^2), \tag{4.3}$$

and the transmission coefficient, t, is [38],

$$\begin{aligned} |t|^2 &= \frac{|U_{\text{out}}|^2}{|U_{\text{in}}|^2} \\ &= 1 - 2\alpha(1-\alpha)\{1 + \cos[(1-2\alpha) K_s |U_{\text{in}}|^2]\}. \end{aligned} \tag{4.4}$$

Since the value of cosine function ranges from -1 to 1, the transmission coefficient has two bounds, 1 and $1 - 4\alpha(1-\alpha)$ at $|U_{\text{in}}|^2 = (2m+1)\pi/[(1-2\alpha)K_s]$ and $2m\pi/[(1-2\alpha)K]$, respectively, with m an integer. When α equal $1/2$, the transmission is always zero, so that the optical energy is reflected back by the loop.

We plot the transmission coefficient, $|t|^2$, as a function of input power, $|U_{\text{in}}|^2$ in Fig. 4.2. The parameters that we used are $\alpha = 0.4$, $\lambda_0 = 1.55$ μm, $L_{\text{fiber}} = 100$ m, and $A_{\text{eff}} = 80$ μm^2. From Eq. (4.2), we now find K_s is 0.162 W^{-1}. The curve oscillates between 0.04 to 1.0 while the period is determined by α and K_s. Results for $\alpha = 0.3$ and 0.45 are also plotted in Fig. 4.2. Saturable absorption occurs because parts of the transmission curve shows a higher transmission as the input power increases, as shown in Fig. 2.3(b) [39], [40]. This effect is fast because the Kerr nonlinearity has a response time on the order of femtoseconds. Also, a small change in α when it is close to 0.5 can lead to a large variation in the oscillation period in the transmission curve. The large input powers shown in Fig. 4.2, which are required for the loop to become transparent, imply that the nonlinear loop mirror is not practical unless long fibers or small effective areas

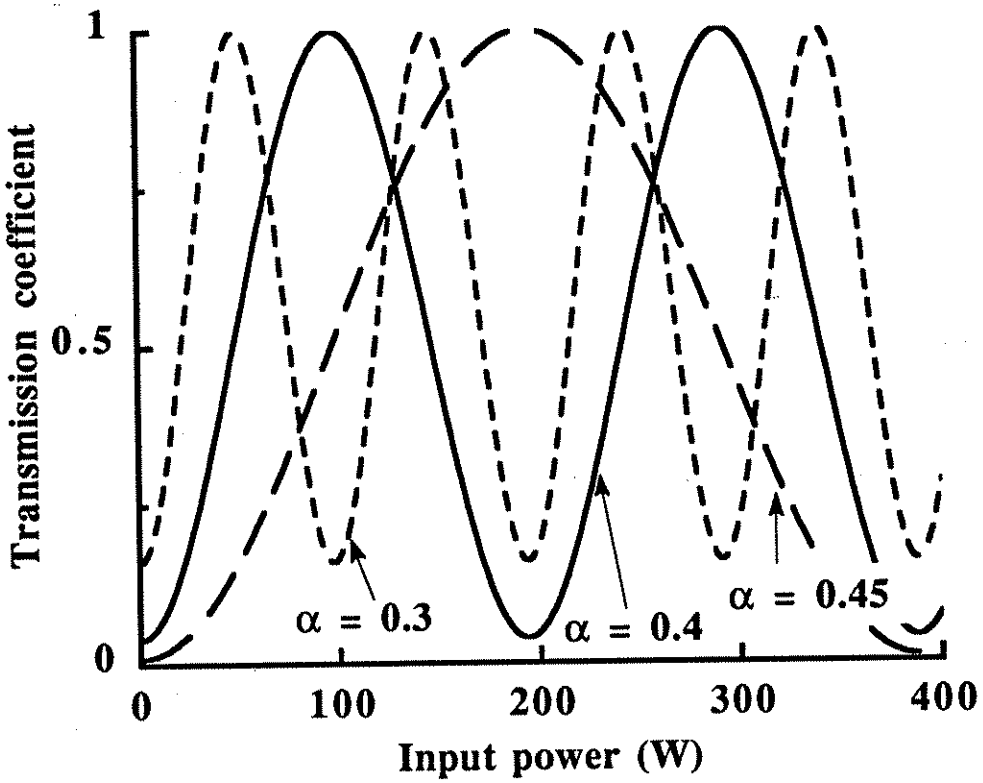

Figure 4.2: Transmission coefficient of the nonlinear loop mirror with parameters $\lambda_0 = 1.55$ μm, $L_{\text{fiber}} = 100$ m, and $A_{\text{eff}} = 80$ μm^2. Three α values, 0.3, 0.4, and 0.45 are plotted.

are used. However, for pulse inputs, the peak power reaches this range easily, and the transmission can reach unity without using high average powers.

4.1.2 Nonlinear Schrödinger equation

A detailed model for pulse propagation in optical fibers is needed when pulse inputs are considered since both dispersion and the Kerr nonlinearity operate simultaneously along the length of the fibers. Using the operators for dispersion and Kerr nonlinearity which are given in Eqs. (2.14) and (2.19), we obtain the

evolution equation

$$i\frac{\partial U}{\partial \Xi} + \frac{\lambda^2 D_m}{4\pi c}\frac{\partial^2 U}{\partial t^2} + \frac{2\pi n_2}{\lambda_0 A_{\text{eff}}}|U|^2 U = 0, \tag{4.5}$$

where we recall that Ξ is length along the optical fiber and we have used the relation Eq. (2.18) to express k'' in terms of D_m, the measured dispersion of the fiber in delay time per unit wavelength per unit length (psec/nm-km).

In theoretical discussions, it is convenient to normalize the evolution equation, reducing it to a standard form. We introduce new units for the normalization—the so-called soliton units. Choosing a normalization time, T_c, which will be fixed later and defining new normalization variables,

$$Z_c = \frac{2\pi c T_c^2}{\lambda_0^2 D_m}, \qquad P_c = \frac{\lambda_0 A_{\text{eff}}}{2\pi n_2 Z_c}, \tag{4.6}$$

we normalize the variables, t, Ξ, and U as follows,

$$s = \frac{t}{T_c}, \qquad \xi = \frac{\Xi}{Z_c}, \qquad u = \frac{U}{\sqrt{P_c}}, \tag{4.7}$$

which yield the nonlinear Schrödinger equation,

$$i\frac{\partial u}{\partial \xi} + \frac{1}{2}\frac{\partial^2 u}{\partial s^2} + |u|^2 u = 0. \tag{4.8}$$

The second term represents the dispersion and the third term represents the Kerr nonlinearity, which is in the form of a self-induced potential. The nonlinear Schrödinger equation is one of the small number of special partial differential equation which can be linearized using the inverse scattering method [41], [42]. As a consequence, it has soliton solutions. These are localized solutions which propagate without changing shapes and maintain their shape during collision with other solitons and continuous radiation. Physically, a soliton creates a self induced potential through the Kerr nonlinearity to counteract the pulse

broadening dispersive effect. The soliton has a hyperbolic secant profile which depends on four parameters, A, v_0, s_0, and ψ, in the following way,

$$u = A\,\mathrm{sech}[A(s - v_0\xi - s_0)]\exp\left[iv_0(s - v_0\xi - s_0) + i\frac{A^2 + v_0^2}{2}\xi + i\psi\right]. \quad (4.9)$$

A stationary solution with unity amplitude is obtained by setting $A = 1$, $v_0 = 0$, $s_0 = 0$, and $\psi = 0$ and the resulting soliton solution is

$$u = \mathrm{sech}(s)\exp(i\xi/2). \quad (4.10)$$

Note that the solution's phase is uniform as a function of time at each position as the pulse propagates down the fiber. The full width at half maxima (FWHM) of this fundamental soliton is 1.763 in s or 1.763 T_c in t. A convenient choice of T_c is

$$\tau = 1.763\,T_c, \quad (4.11)$$

where τ is the FWHM pulse width. Experimentally, one can create a soliton by launching a nearly sech-shaped pulse into a fiber. Then, the experimentalist adjusts the amplitude until the pulse shape does not change at the output end of the fiber.

Hasegawa and Tappert first predicted in 1973 [43] that solitons could be observed in optical fibers. These were first observed experimentally by Mollenauer, *et al.* in 1980 [44]. Since the work of Mollenauer, *et al.*, these solitons have been the continual focus of both theoretical and experimental activity. Solitons are of interest because they tend to act as a unit since they have a uniform phase and do not change their shape during collisions.

Numerically, the nonlinear Schrödinger equation can be solved accurately and efficiently using the beam propagation method which was introduced in Section 3.3.2. We observe that the nonlinear Schrödinger equation contains two parts

which are represented by $\mathcal{L}$, the dispersive operator, and $\mathcal{N}$, the Kerr operator, so that Eq. (4.8) becomes

$$\frac{\partial u}{\partial \xi} = \mathcal{L}u + \mathcal{N}u, \tag{4.12}$$

where $\mathcal{L} = (i/2)\partial^2/\partial s^2$ and $\mathcal{N} = i|u|^2$. The evolution equations with the individual operators, $\partial u/\partial \xi = \mathcal{L}u$ and $\partial u/\partial \xi = \mathcal{N}u$, can be integrated exactly. The solution to Eq. (4.8) is then found numerically by propagating with $\mathcal{L}$ and $\mathcal{N}$ alternatively as described in Section 3.3.2.

4.1.3 Pulse inputs

In order to simulate pulse propagation in the loop mirror, we solve Eq. (4.8) using the beam propagation method. We assume that the input pulses are sech-shaped and are divided into two directions in accordance with Eq. (4.1). We solve separately for the evolution in the two directions, assuming that pulses in the two directions do not interact. The two pulses then recombine at the coupler to create the transmitted wave. Using $\alpha = 0.4$, $D_m = 10$ ps/nm-km, $\tau = 1$ ps, and the same physical parameters used in Fig. 4.2, we find that $T_c = 0.567$ ps, $Z_c = 25.3$ m, and $P_c = 24.4$ W. The fiber length is 100 m ($\approx 4\ Z_c$). The input waveform is

$$u = A\,\mathrm{sech}(s). \tag{4.13}$$

The FWHM is 1.763 and the root mean square (r.m.s.) width is $\langle s^2 \rangle^{1/2} = [\int_{-\infty}^{\infty} s^2\ \mathrm{sech}^2(s) ds]^{1/2} = \pi/\sqrt{6} \approx 1.283$, which are used for pulse width normalization.

We plot the energy transmission coefficient, *i.e.*, output energy/input energy, versus A^2 in Fig. 4.3(a). We also plot the pulse widths in Fig. 4.3(b). Both normalized full width at half maximum (FWHM) and root mean square widths (r.m.s.) are plotted. When both widths are close to unity, the output pulse

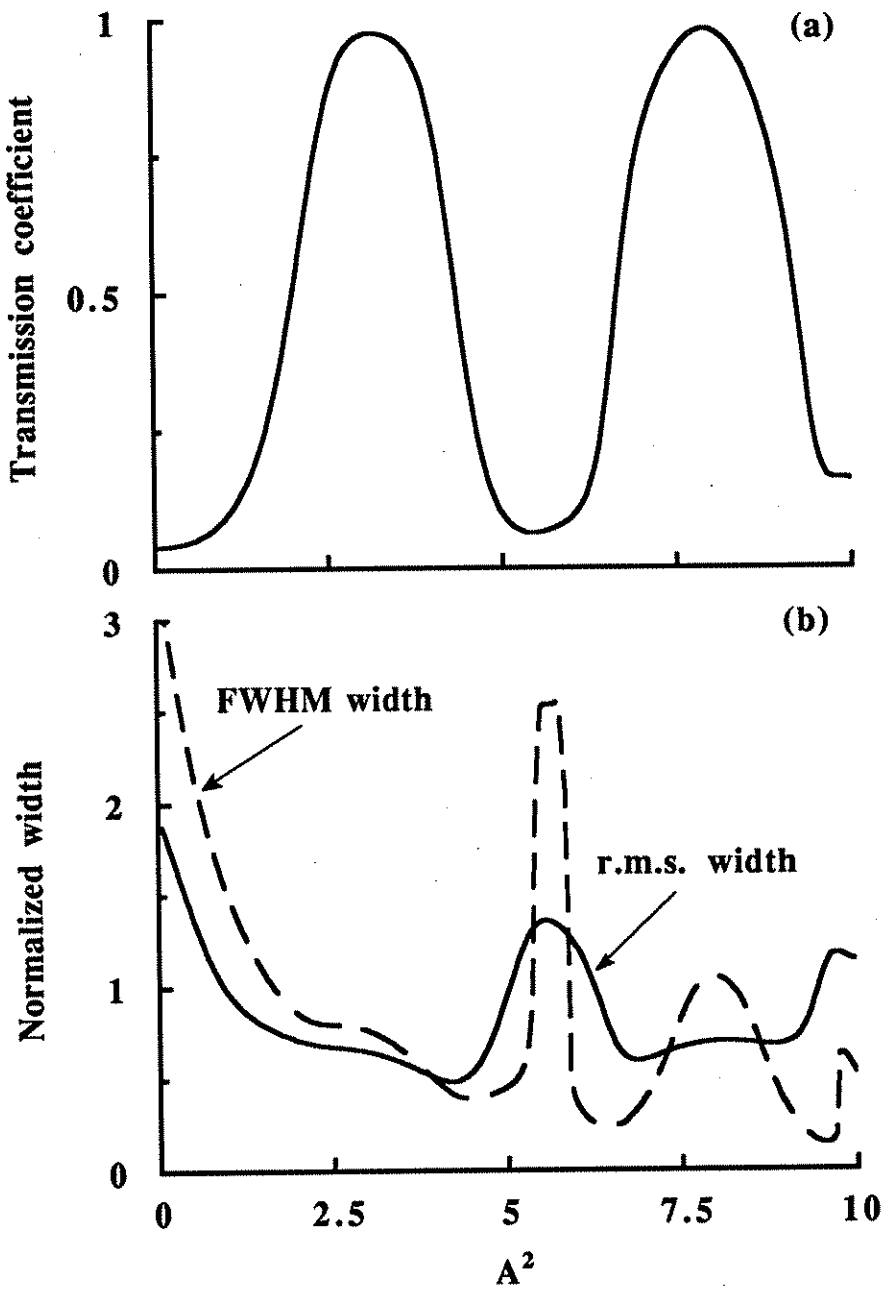

Figure 4.3: (a) Transmission coefficient, and (b) pulse width, as a function of peak power, A^2. Normalized peak power is used.

is sech-like and smooth; otherwise, large pedestals typically appear. Both the transmission coefficient and the output pulse width depend on the input pulse amplitude. The transmission coefficients shows oscillatory behavior with peak values close to unity, which means almost complete transmission is possible. The oscillation period is related to the length of the loop. Longer loops have smaller A values for the first transmission peak. The FWHM and r.m.s. widths follow nearly the same trend; however, the FWHM width changes more drastically because the pulse shape can be spiky. When the widths are less than one, the output pulse duration is shorter than the input, *i.e.*, pulse compression occurs. The small transmission and large widths at $A^2 \approx 5.5$ indicate that the output power is low and that the pulse has a significant pedestal. The fact that the output pulse width may become smaller than the input pulse width is due to the saturable absorption that the loop demonstrates. The loop passes light for the peak portion of a pulse and block light for the wings of the pulse [39], [40]. As a consequence, the output pulse width can become shorter than the input.

4.2 Nonlinear amplifying loop mirrors

In nonlinear loop mirrors, the asymmetry in the power propagating in the two directions is essential since it generates a phase difference which leads to amplitude-dependent interference and saturable absorber action. This asymmetry can also be obtained by using a 50/50 coupler and an erbium-doped fiber amplifier which is situated close to one end of the loop mirror as shown in Fig. 4.4. Because of the asymmetric location of the amplifier, the power levels are different in both propagation directions, even though the final output power from each propagation

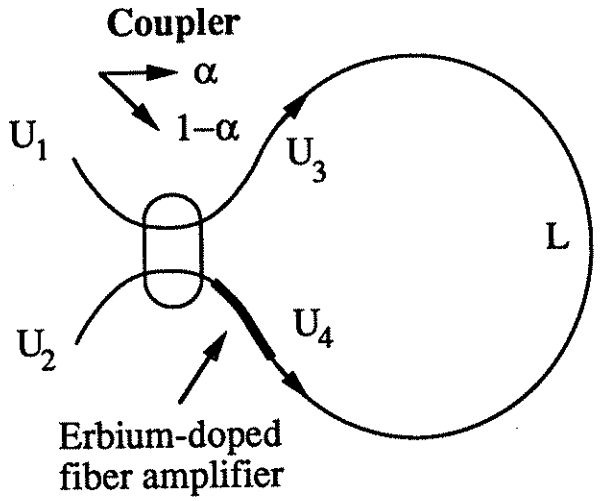

Figure 4.4: The structure of a nonlinear amplifying loop mirror.

direction is identical. A phase difference results.

4.2.1 Quasi-CW inputs

The amplitude gain in a nonlinear amplifying loop mirror is $\sqrt{G} = g_a \approx 1 + g_s$, where G is the power gain defined in Eq. (2.31), g_a is the amplitude gain, and g_s is the steady gain defined in Eq. (2.24). We are assuming that the average input power is large. The amplifier is placed next to one of the output arms of the coupler, so that

$$U_{\text{out}} = \alpha g_a \exp(i\alpha K_s |U_{\text{in}}|^2) U_{\text{in}} - (1-\alpha) g_a \exp[i(1-\alpha) G K_s |U_{\text{in}}|^2] U_{\text{in}}, \quad (4.14)$$

and the energy transmission coefficient, $|t|^2$, is,

$$|t|^2 = G\left\{1 - 2\alpha(1-\alpha)(1+\cos\{[G-(1+G)\alpha]K_s|U_{\text{in}}|^2\})\right\}. \quad (4.15)$$

The transmission coefficient varies between $G[1-4\alpha(1-\alpha)]$ and G, so that power gain as high as G is possible. Note that when $G = 1/(1-\alpha)$, the asymmetries

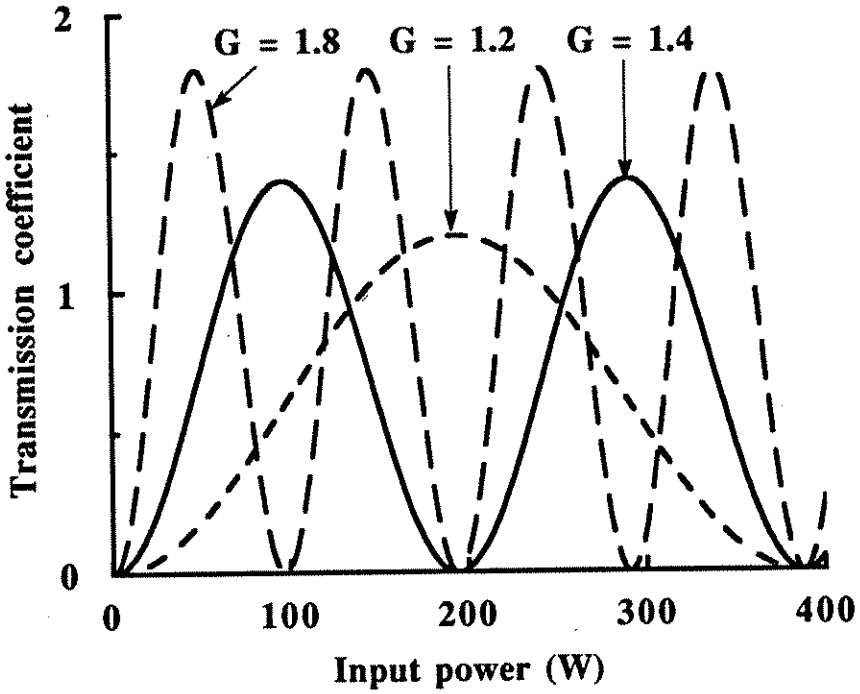

Figure 4.5: Transmission coefficient of the nonlinear loop mirror with parameters $\alpha = 0.5$, $\lambda_0 = 1.55$ μm, $L_{\text{fiber}} = 100$ m, and $A_{\text{eff}} = 80$ μm^2. Three gain values, 1.2, 1.4, and 1.8 are plotted.

due to the coupler and the gain cancel each other and no change in transmission occurs when the input power changes. Setting $\alpha = 0.5$, the case of greatest practical interest, we find

$$|t|^2 = G\left\{1 - 0.5\{1 + \cos[(G-1)K_s|U_{\text{in}}|^2/2]\}\right\}. \tag{4.16}$$

In Fig. 4.5, we use the parameter values as in Fig. 4.2 except that $\alpha = 0.5$. In order to obtain the same oscillation period in the transmission curve for comparison, we choose gain values $(G-1)/2 = 1 - 2\alpha$, where the α values are the same as in Fig. 4.2. For $\alpha = 0.3, 0.4$, and 0.45, we find that $G = 1.8, 1.4$, and 1.2 respectively.

The peak gain of the loop mirror is the gain of the amplifying medium. The minimum transmission coefficient is zero in contrast to that in Fig. 4.2, which is never zero. The period of the transmission curves decreases as the gain increases and becomes highly oscillatory when g is very large. Since the transmission coefficient increases as input power increases in parts of the transmission curves, the loop mirror with gain can also exhibit fast saturable absorption just as is the case for the loop mirror without gain described in Section 4.1.1. In addition to the fast saturable absorption, the loop mirror with gain also provides amplification in some input power ranges.

4.2.2 Pulse inputs

We proceed to numerical simulations of sech-profile inputs. We use the same parameters as in the nonlinear loop mirror. The gain element is an erbium-doped fiber amplifier with a value of 1.4 and is located right next to the coupler. Again, we use the beam propagation code to find the output pulse shapes, transmission coefficients, and pulse widths. The results shown in Fig. 4.6 are similar to Fig. 4.2. The peak gain is larger than unity but it does not reach 1.4, the amplifier gain. When the loop gain is low, the output pulse width is large, and the shape of the output waveform is no longer sech-like. For output pulses with normalized widths smaller than one, the output pulses are sharper than the input pulses. Again, we attribute this sharpening to the fast saturable absorption demonstrated by the amplifying loop mirror.

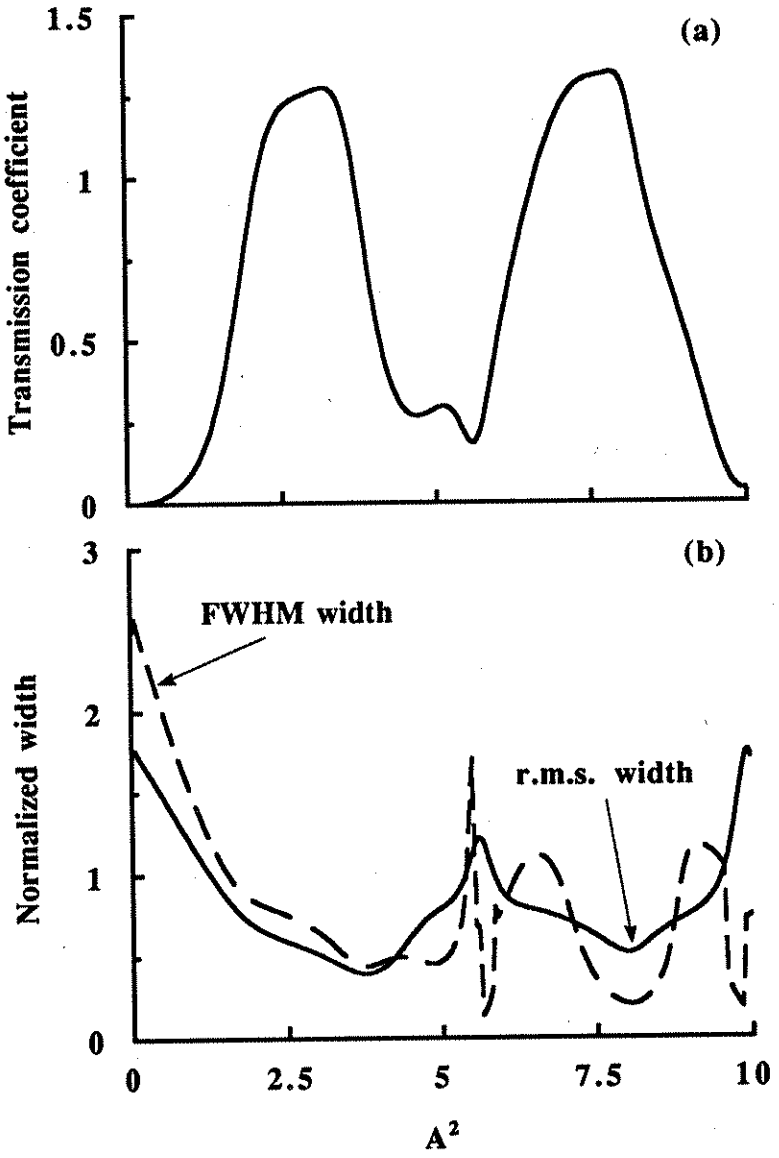

Figure 4.6: (a) Transmission coefficient, and (b) pulse width, as a function of peak power, A^2, when $g = 1.4$. Normalized peak power is used.

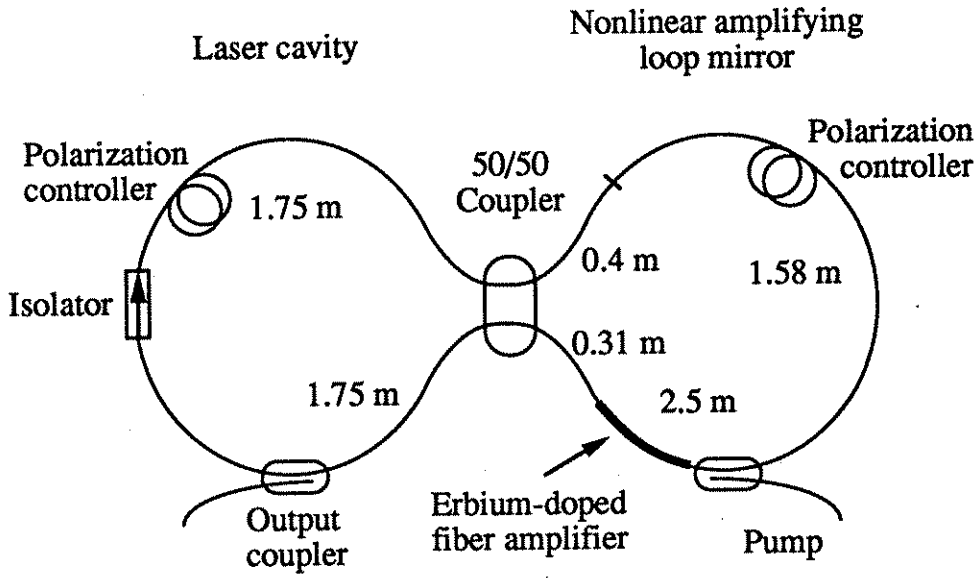

Figure 4.7: The structure of the figure eight laser.

4.3 Figure eight lasers

Since a nonlinear amplifying loop mirror provides gain and fast pulse shaping, it can be used as an element in a fiber ring cavity to form a modelocked laser. As shown in Fig. 4.7, the ring cavity contains a nonlinear amplifying loop mirror on the right hand side. This is the figure eight laser which was proposed by Dr. I. Duling at the Naval Research Laboratory [36], [37]. Pulse widths as short as 100 fsec has been demonstrated using erbium-doped fiber amplifiers. Other elements inside the cavity include an isolator to obtain a single propagation direction, a polarization controller to adjust the polarization state, and an output coupler to access the laser power. No alignment of the laser is needed after fibers are spliced together, and the whole assembly is compact.

Another way to construct a figure eight laser is to place the gain outside the

loop mirror [35]. In this case, the loop mirror acts as a fast saturable absorber and provides pulse shaping without amplification. Successful modelocking has been observed experimentally [45]. We will focus, however, on the figure eight lasers with gain in the loop mirror because more experiments have been done with this configuration.

We shall extract the laser parameters which are required for use in Eq. (2.35) from a given physical setup. From Eq. (2.35), we find that the gain, the loss, the fast saturable absorber, and the Kerr nonlinearity can be determined by considering CW waves since the second derivative term vanishes for a CW wave. The dispersion and frequency limiting terms are then determined by summing up all the dispersive and frequency limiting elements in the cavity. As shown in Fig. 4.8, a 50/50 coupler joins the main cavity and the nonlinear amplifying loop mirror. In the main cavity on the left hand side, starting from the 50/50 coupler and proceeding clockwise, there is a 1.75 m fiber (dispersion 16 = psec/nm-km), a 20% output coupler, and another 1.75 m fiber (dispersion = 16 psec/nm-km) to the 50/50 coupler. The position of the isolator does not affect the operation of the laser. On the right hand side, starting form the 50/50 coupler and proceeding clockwise, there are a 0.4 m fiber (dispersion = 16 psec/nm-km), a 1.58 m fiber (dispersion = 5 psec/nm-km), a 2.5 m erbium-doped fiber amplifier (dispersion = 8.8 psec/nm-km), and, finally, a 0.31 m fiber (dispersion = 16 psec/nm-km) back to the 50/50 coupler. The total length of the setup is 8.29 m and the average dispersion is 11.73 psec/nm-km. The repetition rate is 25 MHz, assuming the refractive index of silica is $n_0 = 1.45$. The effective area A_{eff} of all the fibers is measured to be 85 μm^2, which is also assumed to be uniform for over the fibers used in the laser. The erbium-doped fiber amplifier is measured to have

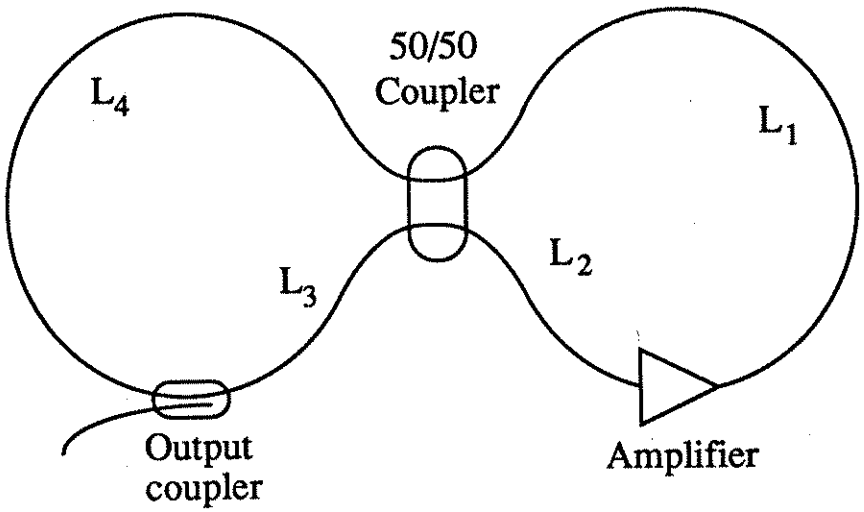

Figure 4.8: Simplified model of the figure eight laser.

$g_0 \approx 3.94$ and $P_{\text{sat}} \approx 2.77$ mW. The loss is estimated to be 60% to include loss due to splicing and fiber coupling. We also assume a frequency limiter of 5 nm to account for other frequency limiting elements as well as the soliton resonance sideband generation, which leads to a frequency dependent loss [10].

Using this information, we find the parameters which must be used in the laser equation, Eq. (2.35). We find that $l = 0.255$, $D = 0.062$ psec^2, and $B = 1/\omega_0^2 = 0.108$ psec^2, using ω_0 as given in Eq. (2.11). We have used a simplified model of the erbium doped fiber amplifier, in which the spread of gain throughout the erbium-doped fiber amplifier is ignored. In this case, we obtain the model of the figure eight laser shown in Fig. 4.8. From the fiber lengths in Fig. 4.7, we infer that $L_1 = 3.23$ m and $L_2 = 1.56$ m.

4.3.1 Determining the fast saturable absorption and nonlinearity

We will proceed with our analysis of the figure eight laser by first performing a CW analysis on the nonlinear amplifying loop mirror and then deriving the laser equation. Using the CW analysis, we found that the loop mirror provides the gain, the fast saturable absorption, part of the Kerr nonlinearity, and part of the dispersion while the main cavity on the left hand side provides the loss, part of the Kerr nonlinearity, and part of the dispersion.

Since polarization controllers are added into the laser cavity to adjust the polarization state of the cavity as shown in Fig. 4.7, a non-reciprocal phase in the amplifying loop mirror may result. With this non-reciprocal phase shift, the wave traveling in one direction has an additional phase offset from the wave which travels in the opposite direction. There is experimental evidence for this additional phase shift from the dependence of the laser operation on the setting of the polarization controllers. When the figure eight laser is assembled, its ability to self-start can be optimized by adjusting the polarization controllers. We account for the non-reciprocal phase by multiplying the counterclockwise propagating beam by a phase angle, $\exp(i\phi)$. We then find

$$U_{\text{out}} = \frac{g_a}{2}\left[\exp\left(i\frac{K_{s,1}+g_a^2K_{s,2}}{2}|U_{\text{in}}|^2\right) - \exp\left(i\frac{g_a^2K_{s,1}+K_{s,2}}{2}|U_{\text{in}}|^2 + i\phi\right)\right]U_{\text{in}}, \tag{4.17}$$

where $K_{s,1}$ and $K_{s,2}$ account for the nonlinear phase changes in the loop mirror due to fibers of length L_1 and L_2 respectively. In order to find the coefficients used in the evolution formalism, we take the logarithm of the operator on U_{in} and then expand it in terms of $|U_{\text{in}}|^2$. The evolution equation for the nonlinear

amplifying loop mirror is then approximated by

$$\frac{\partial U}{\partial z} = \left\{ \ln\left[\frac{(1-\exp(i\phi))g_a}{2}\right] + \frac{i}{2}\left[\frac{K_{s,1} - K_{s,2}\exp(i\phi) + g_a^2(K_{s,2} - K_{s,1}\exp(i\phi))}{1-\exp(i\phi)}\right]|U|^2 \right\} U$$

$$\approx \left\{ g_s + \ln\left(\frac{1-\exp(i\phi)}{2}\right) + \frac{i}{2}\left[\frac{K_{s,1} - K_{s,2}\exp(i\phi) + (1+2g_s)(K_{s,2} - K_{s,1}\exp(i\phi))}{1-\exp(i\phi)}\right]|U|^2 \right\} U, \quad (4.18)$$

where $\ln(g_a) \approx g_s$ and $g_a^2 \approx 1 + 2g_s$ are used. The real part of the third term on the right hand side of Eq. (4.18) corresponds to fast saturable absorption, while the imaginary part corresponds to the Kerr nonlinearity. When ϕ is close to zero, the transmission coefficient is close to zero, and the expansion fails.

In contrast to the amplifying loop mirror, the main cavity contributes only loss and Kerr nonlinearity. The Kerr nonlinearity is due to the fiber and is denoted as $K_{s,c} = K_{s,3} + K_{s,4}$, where $K_{s,3}$ and $K_{s,4}$ correspond to fiber length L_3 and L_4 in Fig. 4.8 respectively. Since there is a unique propagation direction, there is no fast saturable absorption from this part of the ring. From the laser configuration, it follows that $K_{s,1} = 4.93 \times 10^{-3}$ W^{-1}, $K_{s,2} = 2.38 \times 10^{-3}$ W^{-1}, and $K_{s,c} = 5.34 \times 10^{-3}$ W^{-1}.

Combining the effects due to the nonlinear phase changes with the parameters, B, D, and l mentioned previously, we obtain the laser equation for the figure eight laser, which is

$$\frac{\partial U}{\partial z} = \left\{ g_s - l + \ln\left(\frac{1-\exp(i\phi)}{2}\right) + (B+iD)\frac{\partial^2}{\partial t^2} + iK_{s,c}|U|^2 + \frac{i}{2}\left[\frac{K_{s,1} - K_{s,2}\exp(i\phi) + (1+2g_s)(K_{s,2} - K_{s,1}\exp(i\phi))}{1-\exp(i\phi)}\right]|U|^2 \right\} U. \quad (4.19)$$

We will now study the conditions required for self-starting and pulse stability.

4.3.2 Conditions to self-start

Using the technique described in Section 3.1, we determine the parameter requirements for the figure eight laser to self-start. The CW solution has a form of $U = U_c \exp(iP_c z)$ as in Eq. (3.1), which we will substitute into Eq. (4.19). Both Eqs. (3.2) and (3.3) have to be modified accordingly in order to find the CW solution. The amplitude of the CW state is determined by solving

$$g_s = \frac{g_0}{1 + U_c^2/P_{\text{sat}}} = l - \ln\left(\frac{1 - \exp(i\phi)}{2}\right) - \Gamma U_c^2, \tag{4.20}$$

where Γ depends on g_s, or, from Eq. (4.18),

$$\Gamma = \text{Re}\left\{ i\frac{K_{s,1} - K_{s,2}\exp(i\phi) + (1 + 2g_s)[K_{s,2} - K_{s,1}\exp(i\phi)]}{2 - 2\exp(i\phi)} \right\}. \tag{4.21}$$

When $\phi = 0.6$, we find that $U_c = 0.068$ W$^{1/2}$.

We now linearize Eq. (4.19) around this CW solution, and we transform the resulting equation into an eigenvalue problem, in precise analogy with Eqs. (3.7)-(3.12). The resulting eigenvalue problem, which corresponds to Eq. (3.12) is

$$\begin{aligned} \lambda \begin{pmatrix} A_1 \\ A_2 \end{pmatrix} &= M \begin{pmatrix} A_1 \\ A_2 \end{pmatrix} \\ &= \left[\begin{pmatrix} M_1 & M_2 \\ M_2^* & M_1^* \end{pmatrix} - \frac{\epsilon_c}{1 + i\omega T_c} \begin{pmatrix} m & m \\ m^* & m^* \end{pmatrix} \right] \begin{pmatrix} A_1 \\ A_2 \end{pmatrix}, \end{aligned} \tag{4.22}$$

where $m = U_c + i[K_{s,2} - K_{s,1}\exp(i\phi)]U_c^3/[1 - \exp(i\phi)]$. The other variables, T_c, M_1, and M_2, are defined in Chapter 3 after Eqs. (3.6) and (3.12). The relaxation time constant T_0 is 10 msec. The eigenvalue is plotted on the complex λ-plane for all ω in Fig. 4.9 using $\phi = 0.6$. We plot only the right hand side of the complex plane to show that the laser will self-start. We find that λ reaches the

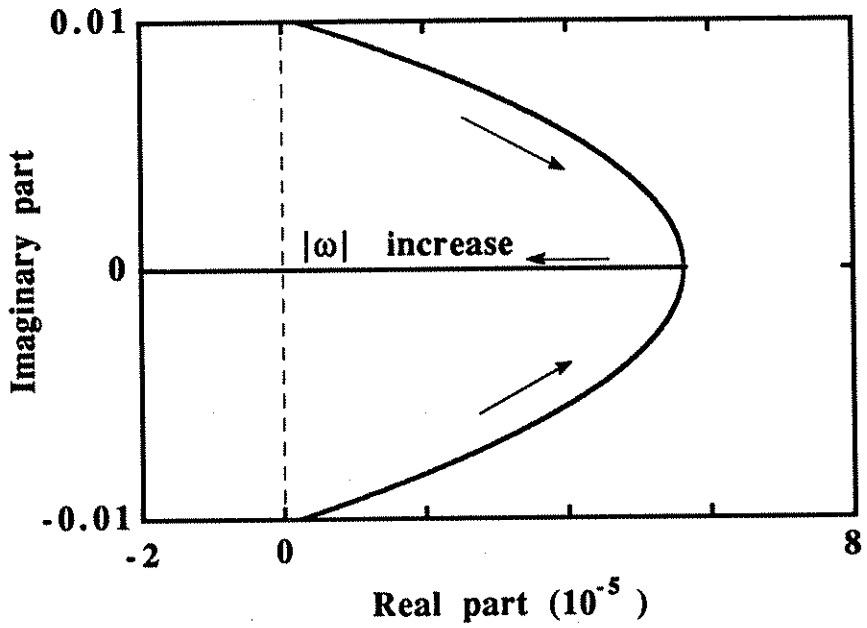

Figure 4.9: The eigenvalue on the complex plane shows that this figure eight laser can self-start.

right hand side of the complex plane when $\mathrm{Re}(\lambda) \approx 2\Gamma U_c^2 = 5.63 \times 10^{-5}$, as described in Section 3.1. Solving Eq. (4.22) numerically for λ, we find that its actual maximum value is 5.73×10^{-5}, which happens at $\omega = 7.18 \times 10^{-3}$ psec^{-1}. For other values of ϕ, we find that the figure eight laser self-starts except when ϕ is close to but less than 2π.

4.3.3 Stability of the pulse solution

We begin by determining the parameters in the *ansatz* in Eq. (3.14). To do so, we must satisfy Eqs. (3.15) and (3.16). Since both Γ and K now depend upon gain and therefore upon A and τ, the solution to these two equations is not straightforward. We have solved these equations numerically in the range $0 \leq \phi < 2\pi$ and the results may be summarized as follows: For $0 \leq \phi < 0.9$,

there exist pulse solutions; for other values of ϕ there is no pulse solution. The parameter β is roughly constant over the region that pulse solution exists and its value is approximately 0.56. We will describe the analysis in more detail using $\phi = 0.6$ as an example. When $\phi = 0.6$, $\beta = 0.5437$ and $a = 0.8680$, the pulse width is $\tau = 206$ fsec and the amplitude is $A = 41$ $W^{1/2}$.

We now study the linear stability using the technique described in Section 3.2. Again, since Γ and K depend on gain, the stability can be studied by using perturbation method or solving the resulting eigenvalue problem numerically. In addition to the terms in Eq. (3.29), the terms due to the gain dependence of Γ and K have to be taken into account. From Eq. (4.18), the perturbation $U = U_0 + \hat{u}$ will lead to an extra term on the right hand side of Eq. (3.29), and the equation becomes

$$\frac{\partial \hat{u}}{\partial \xi} = \mathcal{R}(\hat{u}) - \epsilon_k \operatorname{sech}^{3+i\beta}(s) \int_{-\infty}^{\infty} \operatorname{sech}^{1-i\beta}(s')\hat{u} + \operatorname{sech}^{1+i\beta}(s')\hat{u}^* ds', \qquad (4.23)$$

where $\mathcal{R}(\hat{u})$ is the right hand side of Eq. (3.29) and $\epsilon_k = i[K_{s,2} - K_{s,1}\exp(i\phi)]A^2\epsilon_p$ $/[1-\exp(i\phi)]$ and ϵ_p is defined in Eq. (3.31). Note that ϵ_k is in general a complex number. Using the calculated A and τ, we find $\epsilon_p = 0.0373$ and $\epsilon_k = 0.259 + 0.230i$. We find the eigenvalue $\lambda = 0.3273$ for the most unstable discrete mode and the corresponding eigenfunction using series expansion method. The adjoint problem is also solved for the same eigenvalue. We estimate that the eigenvalue is $\lambda = 0.1443$ when only ϵ_p is used, while $\lambda = -0.4798$ when both ϵ_p and ϵ_k are applied. These are to be compared to results from the matrix eigenvalue solver, which gives $\lambda = 0.1426$ when only ϵ_p is used, and $\lambda = -0.5734$ when both ϵ_p and ϵ_k are applied. The eigenvalues which were determined numerically, are plotted on the complex λ-plane in Fig. 4.10. All the eigenvalues are on the left hand side of the plane, and the laser is therefore stable.

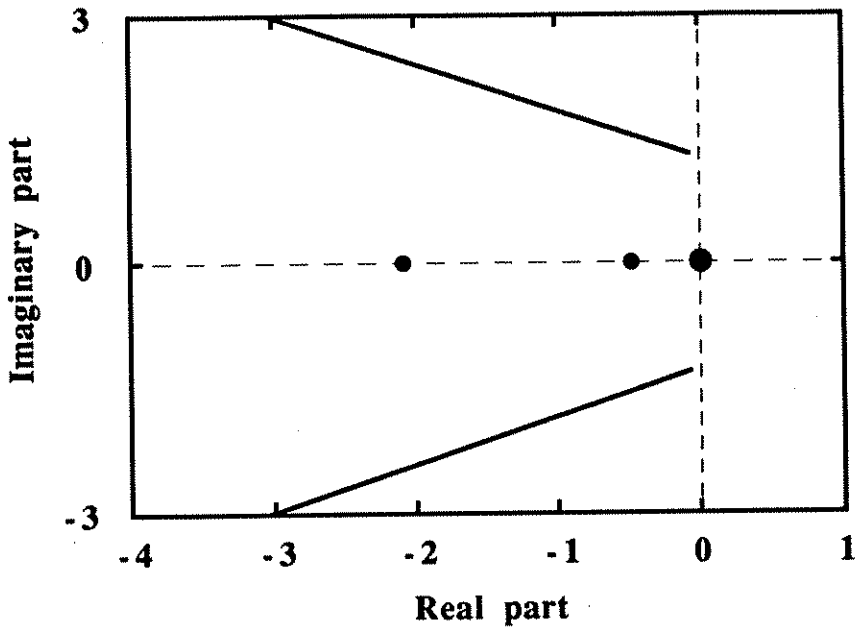

Figure 4.10: Eigenvalues of the figure eight laser on the complex λ-plane.

Since Γ and K depend on g_s and, therefore, P_{av}, the inequalities given in Eqs. (3.52) and (3.53) are not applicable, and the value of ϵ_p which is required to stabilize the laser is reduced, since the effect of non-zero ϵ_k is to further stabilize the laser. From a perturbation calculation using Eq. (3.44), we find that the eigenvalue will shift to the left when $\text{Re}(\epsilon_k)$ is positive. The implication of this additional eigenvalue shift is that it extends the parameter range in which the figure eight laser is stable. Physically, it is easier to modelock the laser by putting the saturable gain inside the loop mirror, the case considered here, than outside the loop mirror, the case considered in Section 3.2.

4.4 Simulation of the figure eight laser

We will carry out the numerical simulation in the modular fashion described in Section 3.3.2. The laser configuration has been shown in Fig. 4.8. Using the beam propagation method, we calculate the pulse evolution in each segment of the fiber using the nonlinear Schrödinger equation in Eq. (4.8). We follow the pulse envelope, which will change after passing through each element. We normalize the time variable to $T_c = 200$ fsec. The dispersion of each of the fibers is set to 11.73 psec/nm-km and the effective area of the fibers are assumed to be 85 μm^2 uniformly. Then we calculate $Z_c = 2.677$ m and $P_c = 244.77$ W from Eq. (4.6). The fiber lengths in this normalization are $L_1 = 1.21\ Z_c$, $L_2 = 0.58\ Z_c$, and $L_3 = L_4 = 1.21\ Z_c$. The gain inside the loop mirror is assumed to be a lumped gain, whose behavior is given by Eq. (2.29). The parameter values for the gains are $g_0 = 3.94$ and $P_{\rm sat} = 2.77$ mW. The parameter $P_{\rm sat}$ corresponds to 2.263 in the normalized units, assuming a repetition rate of 25 MHz. The average power $P_{\rm av}$ is now represented by $\int_{-\infty}^{\infty} |u|^2\, ds$, since the round trip time has been taken into account in finding $P_{\rm sat}$. The output coupler is set to 60% to include other losses in the cavity. The frequency limiter is described by Eq. (2.9), where ω_0 is 3.05 psec^{-1} in this normalization, corresponding to 5 nm in the frequency spectrum. We use the smaller value to include other possible frequency limiting effects from other elements, such as the coupler and the isolator, or the effect referred to as soliton resonance sideband generation.

The non-reciprocal phase shift $\exp(i\phi)$ is important in the laser operation, since it affects the characteristic of the nonlinear amplifying loop mirror at the working point of the laser. With a 50/50 coupler and a small value of ϕ, the amplifying loop mirror becomes a reflector and transmits little light. The laser

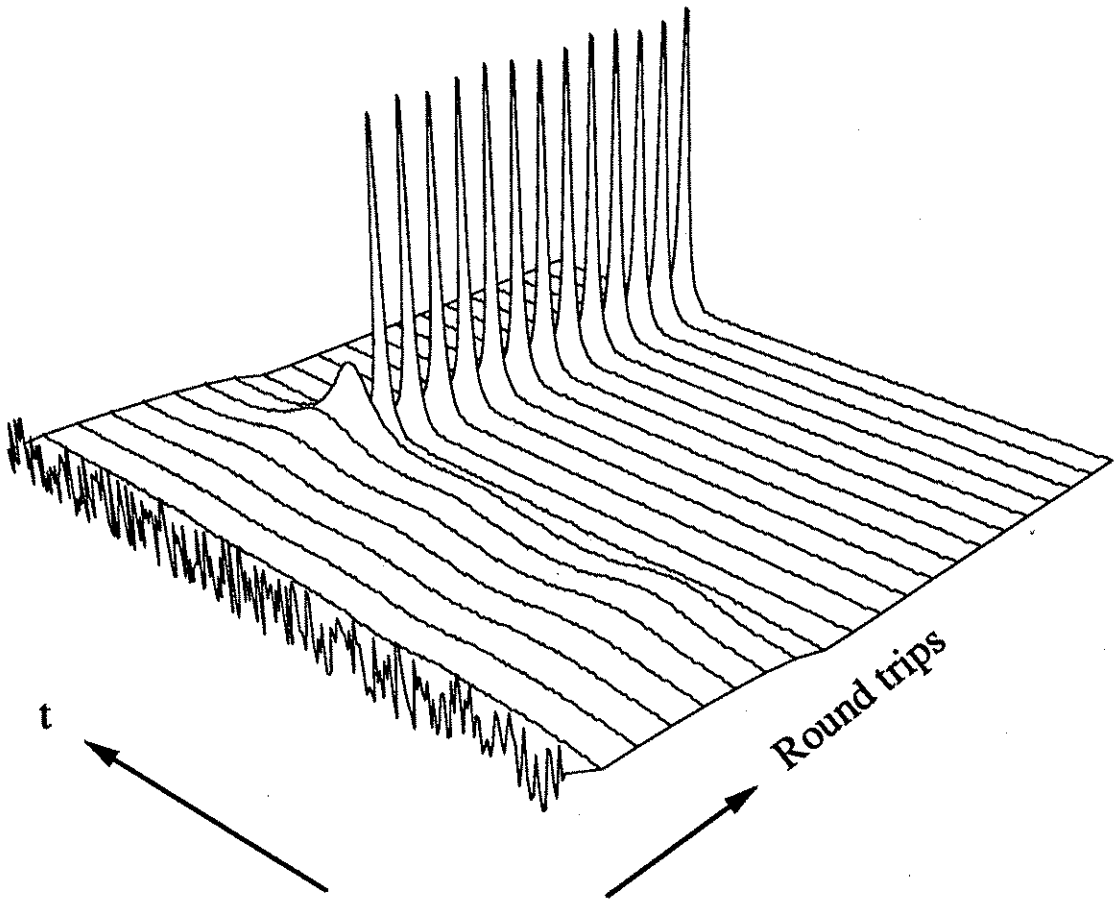

Figure 4.11: Simulated startup process. Each line represents 10 round trips.

becomes harder to self-start since the light energy must have large fluctuations to reach the transparent portion of the loop mirror. With a large value of ϕ, *i.e.*, around π, there is no saturable absorption. The transmission curve in Fig. 4.5 is translated by the phase angle ϕ and the transmission coefficient and slope at $|U_{\text{in}}|^2 = 0$ are changed. Experimentally, one finds that there is sensitivity when adjusting polarization controllers in the loop mirror, since they affect the ϕ value.

We show a numerical simulation using $\phi = 0.6$ in Fig. 4.11. With this ϕ value, the loop mirror provides fast saturable absorption. We plot the pulse evolution from initial noise into a pulse after about 80 round trips, which corresponds to 3.2 μsec. The pulse width (FWHM) is 2.46 $T_c = 492$ fsec, the spectral width is 4.48 nm and the $\Delta t \Delta f = 0.28$.

We have also carried out a more thorough study on the effect of varying the ϕ value from 0 to 2π. When $0 < \phi \leq 1.2$, the laser operate in pulse mode stably. When $1.3 < \phi \leq 4.8$, the optical energy in the laser evolves into pulses but the pulse operation is not stable. A typical outcome is shown in Fig. 4.12 with $\phi = 2.0$. When $4.8 < \phi < 2\pi$, the laser does not self-start and has only a CW output. When ϕ is close to 2π, there is no output energy since loss is larger than gain.

4.5 Summary

We have carried out an analysis of the figure eight laser. Since the gain medium is located in the nonlinear loop mirror to provide both gain and saturable absorption, Γ and K are both functions of the pulse shape. We calculate the working

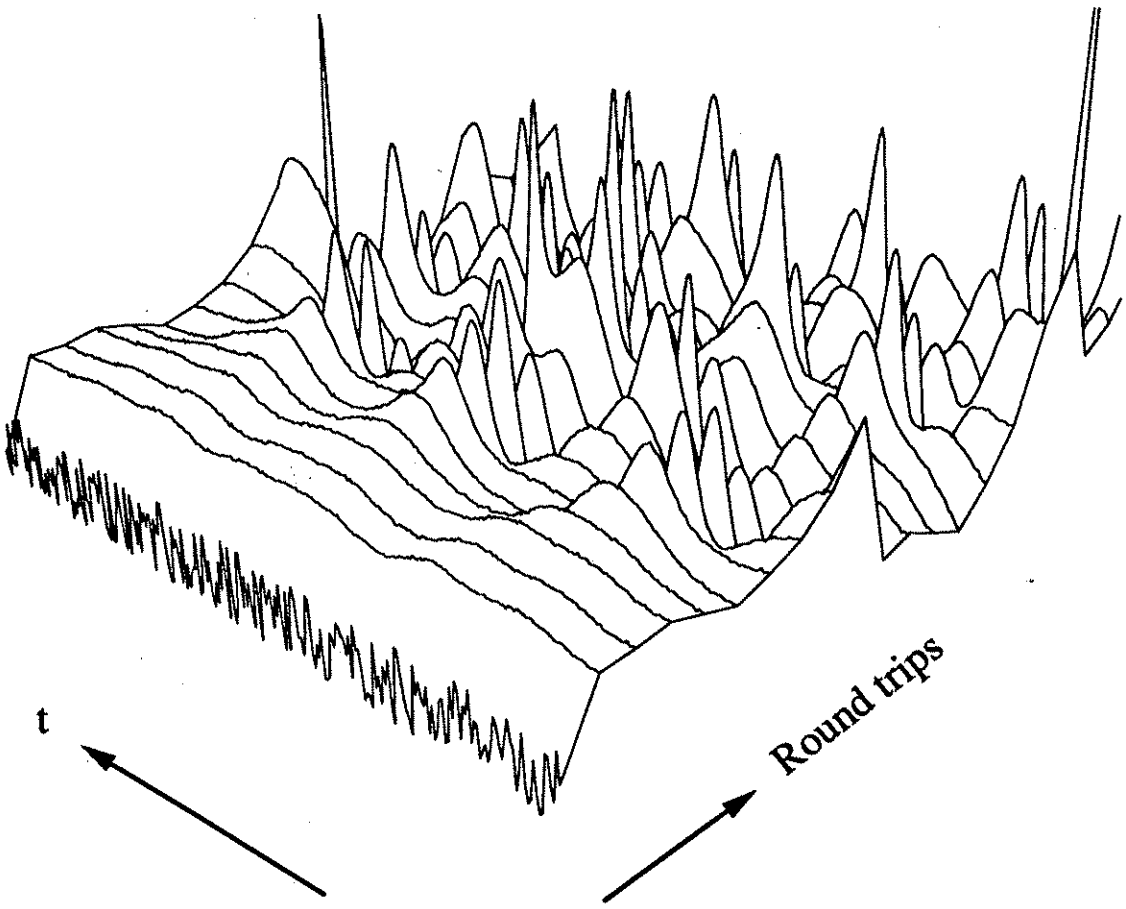

Figure 4.12: A typical outcome of the numerical simulation when $\phi > 1.3$. In this figure, $\phi = 2.0$. Each line represents 10 round trips

points for both the CW and pulse solutions. The stability of both working points is then investigated and particular results for $\phi = 0.6$ are presented. We find that the dependence of Γ and K on gain saturation further stabilizes the mode-locking relative to the model considered in Section 3.2 which corresponds to a gain located outside the loop mirror.

The numerical and analytical results both show that there is a range of ϕ in side of which the laser can operate stably. The numerical simulation shows that the figure eight laser is able to self-start from noise and operate stably in pulsed mode for $0 < \phi \leq 1.2$, while analytical results predicts $0 < \phi < 0.9$. When $\phi = 0.6$ the pulse width calculated analytically is 206 fsec and is 492 fsec in the numerical simulation. This result can be further improved if more sophisticated models for the saturable absorber are used, such as one that includes higher orders in the expansion of Eq. (4.18).

Chapter 5

Fiber Ring Laser

The fiber ring laser discussed in this chapter was first proposed by Dr. L. Mollenauer [27] for telecommunication applications. Since solitons are to be used as carriers to convey digital signals, a suitable laser source is desirable. The laser basically consists of a long fiber and a fiber amplifier arranged in a ring configuration. The original idea was that the modulational instability in the fibers in the anomalous dispersion regime would lead to self-starting of the laser and evolution of the modelocked pulses into solitons since solitons are the fundamental nonlinear propagation mode in fibers.

Unfortunately, the modulational instability does not provide saturable absorption, and simulations show that the laser will not modelock when only the modulational instability is present [9]. It was found, however, that nonlinear polarization rotation and polarization selective elements would lead to the laser self-starting. This issue is discussed in Section 5.1. Since no polarization selective elements were explicitly included in the design of the fiber ring laser, we discuss ways in which they may have been implicitly included. The structure of the fiber ring laser is presented in Section 5.2 and models of the laser elements

not previously described are presented.

To analyze the fiber ring laser, we assume a set of polarizer angles and extract parameters used in the laser equation. In Section 5.3, we perform a stability analysis of the fiber ring laser. The evolution of optical waves inside the laser system is then simulated in Section 5.4 using the beam propagation method. A summary is given in Section 5.5.

5.1 Saturable absorption due to soliton polarization rotation

In Chapter 4, we discussed fast saturable absorption using nonlinear amplifying mirrors. The Kerr effect plays a key role in the mirror's operation. In this Chapter, applying the Kerr nonlinearity again, we will present another setup that consists of polarization selective elements and a birefringent optical fiber to form a saturable absorber. Two polarization modes of an optical fiber are utilized in the process. A single mode fiber actually has two polarization modes with slightly different refractive indices. Light energy in one polarization axis, which is called the fast axis, propagates faster than the other, which is called slow axis. The difference between the refractive indices is small, $\Delta n/n \approx 10^{-5}$-$10^{-7}$ [46], and the group velocity dispersion is negligible in our study. The Kerr nonlinearity affects the phases in both the self and cross polarizations, leading respectively to self and cross phase modulation. The coefficient of cross phase modulation is 2/3 that of the self phase modulation in standard, linearly birefringent fiber [47], [48], which was used in construction of fiber ring lasers.

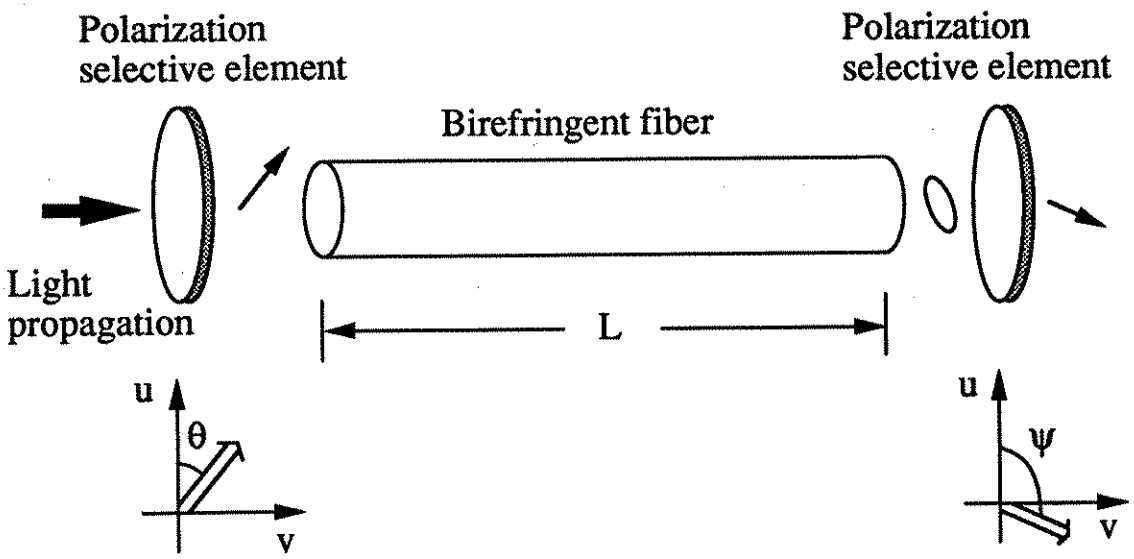

Figure 5.1: A birefringent optical fiber of length L in between of a pair of polarizers. The polarization states are indicated. The elliptically polarized output of the fiber is made linear. This simple setup is equivalent to a saturable absorber.

5.1.1 Transmission curve for CW inputs

For CW inputs to a birefringent fiber, the effect of the Kerr nonlinearity is obtained by modifying Eqs. (2.19) which yields,

$$\begin{aligned} \left.\frac{\partial U}{\partial \Xi}\right|_{\text{Kerr}} &= i\left(\frac{2\pi n_2}{\lambda_0 A_{\text{eff}}}|U|^2 + \frac{2}{3}\frac{2\pi n_2}{\lambda_0 A_{\text{eff}}}|V|^2\right)U, \\ \left.\frac{\partial V}{\partial \Xi}\right|_{\text{Kerr}} &= i\left(\frac{2}{3}\frac{2\pi n_2}{\lambda_0 A_{\text{eff}}}|U|^2 + \frac{2\pi n_2}{\lambda_0 A_{\text{eff}}}|V|^2\right)V, \end{aligned} \tag{5.1}$$

where U and V are the CW powers in the two polarizations. The fiber length is L. Equation (5.1) describes the phase evolution in each polarization. Since the ratio of cross phase modulation to self phase modulation is not unity, the relative phase between U and V and, therefore, the polarization state of the output can be changed by the power levels of U and V [49]-[51]. Using a polarizer at the

output end, we can change the transmission coefficient by varying the input power. Therefore, a piece of birefringent fiber with polarizers at both ends, as shown in Fig. 5.1, will act as a fast saturable absorber. The input light to the fiber is linearly polarized at an angle θ with respect to the u polarization. The output light from the fiber then passes through another polarizer at an angle ψ. To make a saturable absorber, we adjust both polarizers such that the lower intensity wave is discarded, while the higher intensity wave is passed. Explicitly, we find that

$$U_{\text{out}} = \left\{ \cos\theta\cos\psi \exp\left[i\left(\cos^2\theta + \frac{2}{3}\sin^2\theta\right) U_{\text{in}}^2 K_s + i\phi \right] + \sin\theta\sin\psi \exp\left[i\left(\frac{2}{3}\cos^2\theta + \sin^2\theta\right) U_{\text{in}}^2 K_s \right] \right\} U_{\text{in}}, \tag{5.2}$$

where K_s is the self phase modulation constant as defined in Eq. (4.2) and U_{in} and U_{out} are the amplitudes of the input and output waves. The additional phase shift ϕ in the U polarization is to account for the linear phase difference caused by other effects such as a difference in the refractive indices. The power transmission coefficient can be derived from Eq. (5.2), *i.e.*,

$$|t|^2 = \sin^2\theta\sin^2\psi + \cos^2\theta\cos^2\psi + \frac{1}{2}\sin 2\theta \sin 2\psi \cos\left[\frac{U_{\text{in}}^2 K_s}{3}\cos 2\theta + \phi\right], \tag{5.3}$$

When $\theta = 0$ or $\pi/2$, the light energy is transmitted along one of the polarization axes, so $|t|$ is independent of U_{in}. Also when $\theta = 45°$, $|t|$ is a constant since both polarizations have equal power and the phase shifts due to cross phase modulation are the same. The transmission amplitude $|t|$ has its maximum variation at $\theta \approx 22.5°$.

To show the fast saturable absorption demonstrated by this combination, we set $\phi = 0$, $\theta = 22.5°$, and $\psi = 100°$, $112.5°$, $125°$, and obtain the set of transmission curves shown in Fig. 5.2. In plotting Fig. 5.2, we assume a 100 m

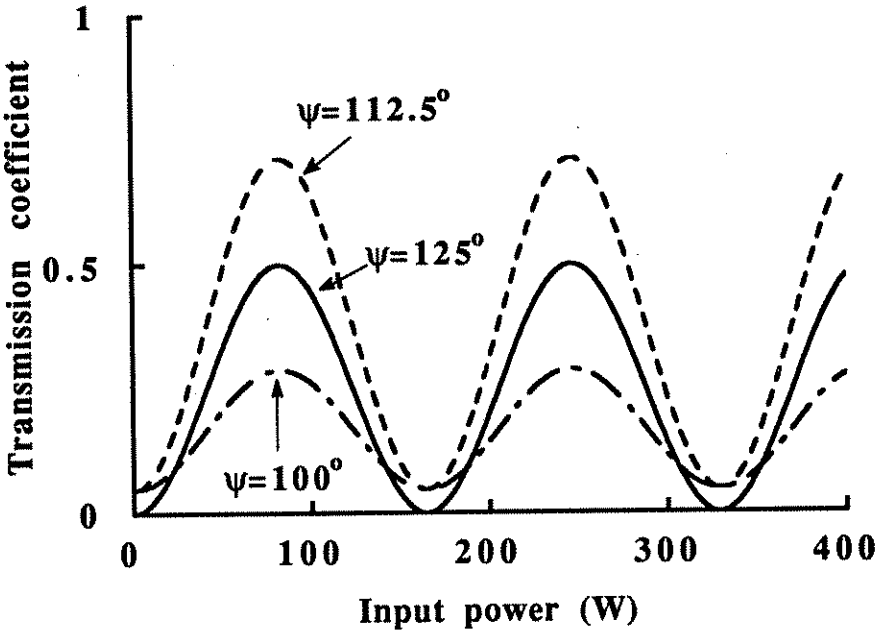

Figure 5.2: The power transmission coefficient as a function of input power. The length of the fiber is 100 m, $A_{\text{eff}} = 80\ \mu\text{m}^2$ and $\lambda_0 = 1.55\mu\text{m}$. The input polarization angle is $\theta = 22.5°$ and output polarization angles are $\psi = 100°$, 112.5°, and 125° as indicated.

long fiber with $A_{\text{eff}} = 80\ \mu\text{m}^2$ and $\lambda_0 = 1.55\ \mu\text{m}$, which gives a K_s of 0.162 W^{-1}. These parameter values are taken from Section 4.1 so that we compare the loop mirror to the nonlinear polarization rotator. Observing this figure, we find that the transmission characteristic is equivalent to that of fast saturable absorbers at low power inputs. The transmission can be zero for the curve corresponding to $\psi = 112.5°$. We note that when $\phi = 0$, the transmission is zero for small input power if $\theta - \psi = \pm\pi/2$.

5.1.2 Transmission curve for pulse inputs

Wave propagation in linearly birefringent optical fibers is described by the coupled equations [47], [48]

$$\begin{aligned} i\frac{\partial U}{\partial \Xi} + ik'\frac{\partial U}{\partial t} - \frac{1}{2}k''\frac{\partial^2 U}{\partial t^2} + \frac{2\pi n_2}{\lambda_0 A_{\text{eff}}}\left(|U|^2 + \frac{2}{3}|V|^2\right)U = 0, \\ i\frac{\partial V}{\partial \Xi} + il'\frac{\partial V}{\partial t} - \frac{1}{2}l''\frac{\partial^2 V}{\partial t^2} + \frac{2\pi n_2}{\lambda_0 A_{\text{eff}}}\left(\frac{2}{3}|U|^2 + |V|^2\right)V = 0, \end{aligned} \tag{5.4}$$

where $k(\omega)$ and $l(\omega)$ are the dispersion relations for the two axes, $k' = \partial k/\partial\omega|_{\omega_0}$, $l' = \partial l/\partial\omega|_{\omega_0}$, $k'' = \partial^2 k/\partial\omega^2|_{\omega_0}$, and $l'' = \partial^2 l/\partial\omega^2|_{\omega_0}$. In the following, we assume $k'' = l'' = -\lambda^2 D_m/(2\pi c)$. We also assume $k' > l'$, *i.e.*, U is the slow axis, and $k' - l' = \Delta n/c$, where Δn is the difference in refractive indices between the two polarization axes. The normalization that we will use is similar to that of Section 4.1. First, we transform to retarded time by setting $t' = t - [(k' + l')/2]\Xi$ and $\Xi' = \Xi$. Then, we define new variables [48],

$$s = \frac{t'}{T_c}, \quad \xi = \frac{\Xi'}{Z_c}, \quad u = \frac{U}{\sqrt{P_c}}, \quad v = \frac{V}{\sqrt{P_c}}, \tag{5.5}$$

where Z_c and P_c given in Eq. (4.6). Finally, we let

$$\delta = \frac{Z_c \Delta n}{2cT_c}. \tag{5.6}$$

The quantity δ which is a measure of the birefringence strength is negligible in all the cases we will be considering. The equation that we finally obtain is the coupled nonlinear Schrödinger equation [48],

$$\begin{aligned} i\frac{\partial u}{\partial \xi} + i\delta\frac{\partial u}{\partial s} + \frac{1}{2}\frac{\partial^2 u}{\partial s^2} + \left(|u|^2 + \frac{2}{3}|v|^2\right)u = 0, \\ i\frac{\partial v}{\partial \xi} - i\delta\frac{\partial v}{\partial s} + \frac{1}{2}\frac{\partial^2 v}{\partial s^2} + \left(\frac{2}{3}|u|^2 + |v|^2\right)v = 0. \end{aligned} \tag{5.7}$$

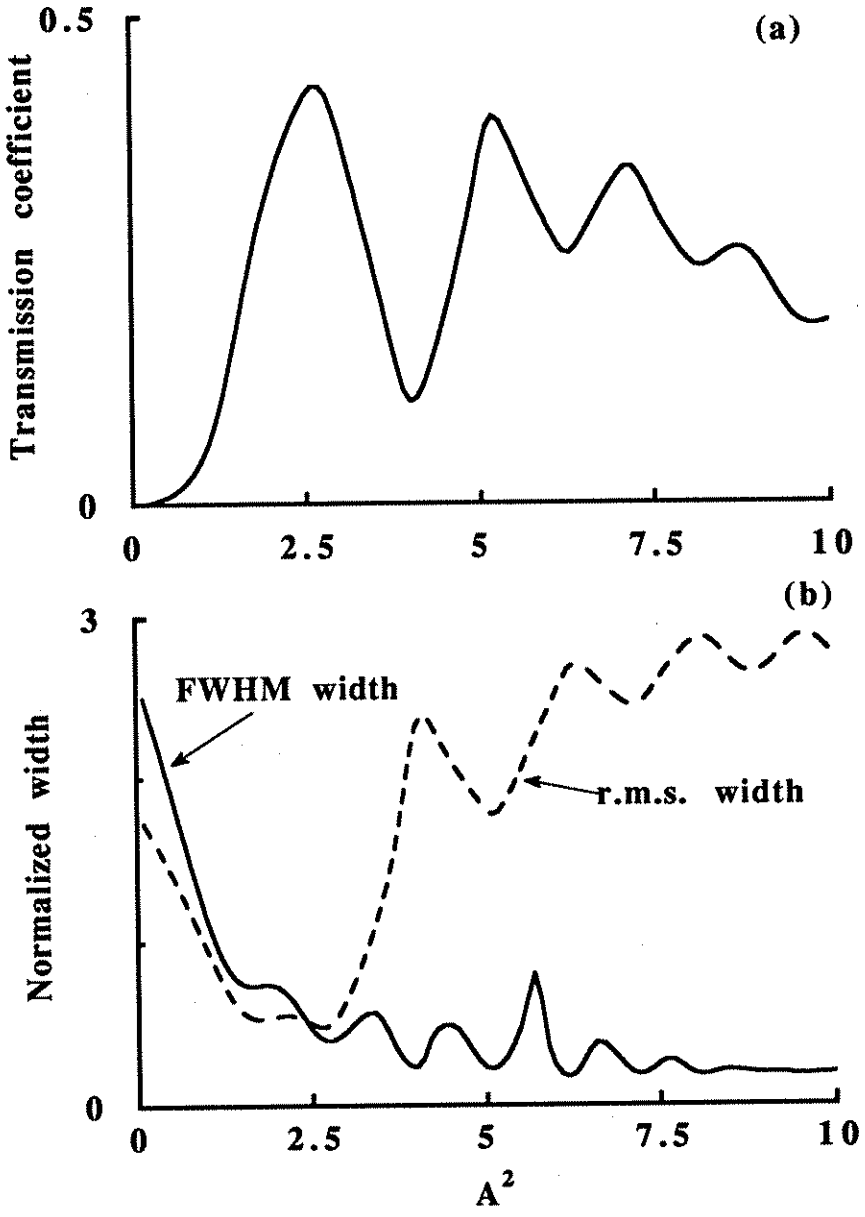

Figure 5.3: (a) Transmission coefficient, and (b) pulse widths, of the setup shown in Fig. 5.1, as a function of peak power A^2 in normalized units.

Setting $\delta = 0$ and using the same parameters which we previously used in our discussion of the loop mirror in Section 4.1, *i.e.*, $D_m = 10$ ps/nm-km, $\tau = 1$ ps, $\lambda_0 = 1.55$ μm, $L = 100$ m, we obtain the transmission coefficient and normalized pulse widths in Fig. 5.3. The fiber length is $4Z_c$ in the normalized units. The polarizers are set to $\theta = 22.5°$ and $\psi = 112.5°$ and the phase offset ϕ is set to zero. The transmission curve shows an oscillatory characteristic similar to those in Figs. 4.3 and 4.6. The device exhibits saturable absorption for $A^2 < 3$. Its maximum transmission value is near 0.5, since the output polarizer blocks the low power pedestal. When the peak is larger than 4, the output pulse is degraded, and r.m.s. widths larger than one are observed. When the transmission value is near its maximum, the pulse widths are less than unity and saturable absorption occurs.

5.2 Structure of the soliton ring laser

A schematic diagram of the fiber ring laser that we are going to study is shown in Fig. 5.4 [27]. It contains a length of fiber, a delay stage, a polarization controller, a fiber Fabry-Perot interferometer, an Er-doped fiber amplifier, an isolator, and an output coupler. The long fiber has a negative group velocity dispersion which can sustain solitons when the Kerr nonlinearity becomes important. The Fabry-Perot interferometer controls the pulse repetition rate by passing only those pulse trains that have a repetition rate T, where T is the etalon round-trip time. The delay stage is used to tune the central wavelength of the fiber ring laser. Since the optical length of the fiber ring has to be an integral multiple of twice the etalon length, the wavelength will be forced to adjust through group

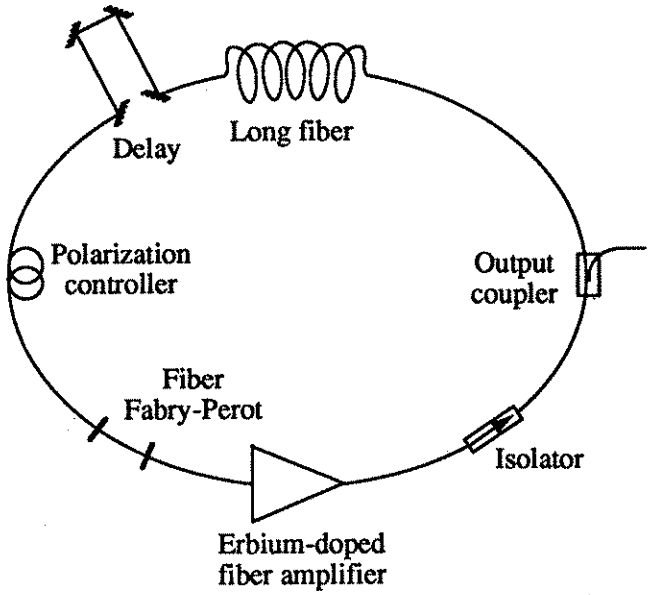

Figure 5.4: Schematic diagram of the fiber ring laser.

velocity dispersion to compensate any extra optical length in the delay stage. The erbium-doped fiber amplifier is generally pumped at either 980 μm or 1480 μm and acts as the gain medium in the laser cavity. The isolator is used to block counterpropagating waves and the polarization controller is used to change the polarization state inside the ring cavity.

One might suppose that the startup and modelocking of the fiber ring laser occurs as follows: The laser could start from noise and build up its CW state when the gain and loss balance each other. The CW state then breaks into pulses due to the modulational instability which exists in an optical fiber with anomalous dispersion. The pulses are equally separated after passing through the fiber Fabry-Perot interferometer. Next, these pulses evolve into solitons because that solitons are the modes of nonlinear wave propagation in optical fibers. The output soliton trains could be useful in telecommunication. Since soliton output

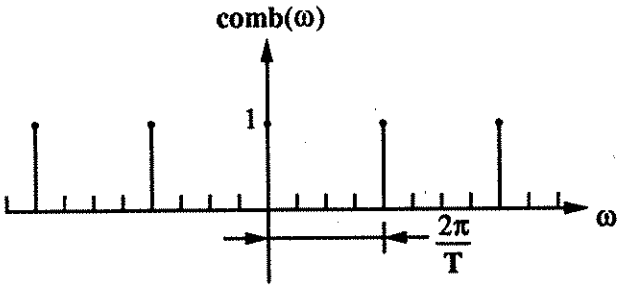

Figure 5.5: The comb function in the frequency domain.

is anticipated from this intuitive picture, this laser has been named the soliton ring laser. However, in the following sections, we will show that to make the fiber ring laser start from noise and operate stably, we need both a frequency limiter and a saturable absorber. These were present in the original, experimental setup [27] although not part of the explicit design.

First, we discuss the modeling of the elements in the soliton ring laser that were not previously discussed in Chapter 3. We assume that the Fabry-Perot interferometer has an infinite finesse, which implies that

$$\tilde{u}_{\text{out}}(\omega) = \text{comb}(\omega)\tilde{u}_{\text{in}}(\omega), \tag{5.8}$$

where $\tilde{u}_{\text{in}}(\omega)$ is the Fourier transform of $u_{\text{in}}(t)$, the pulse train at the input of the Fabry-Perot interferometer, and $\tilde{u}_{\text{out}}(\omega)$ is the corresponding output. The comb function is shown in Fig. 5.5 and defined as: $\text{comb}(\omega) = 1$ when $\omega = 2\pi n/T$, where n is any integer and T is the repetition period of the interferometer; $\text{comb}(\omega) = 0$, when $\omega \neq 2\pi n/T$ [52]. A typical repetition rate in the experiments is 2.5 GHz, which is appropriate for high speed telecommunication applications. This frequency corresponds to $T = 400$ psec. In numerical simulations, the

interferometer action is implemented through the periodic boundary conditions in the simulation window.

Referring to the model in Section 2.3, we use Eq. (2.29) to model the erbium-doped fiber amplifier. Since the length of the cavity is usually much longer than the length of the amplifier, the gain is treated as a lumped gain. We set $g_0 = 3.94$ and $P_{\text{sat}} = 2.77$ mW, as in previous chapters. The output coupler extracts 10% of the power from the cavity. We also introduce a frequency limiter as in Section 4.4, whose pass band is 5 nm at 1.55 μm. The fiber is modeled by the coupled nonlinear Schrödinger equation to take into account the effect of birefringence, dispersion, and nonlinearity. The fiber length is $L = 2000$ m with an average group velocity dispersion of 10 psec/nm-km. The effective area is 85 μm^2.

We assume that the fast saturable absorption mentioned in Section 5.1 is acting on this long fiber and the polarization selective elements at both ends are assumed to be at $\theta = 22.5°$, $\psi = 112.5°$ by the polarization controllers in the cavity, and ϕ is allowed to change. Although polarization selectivity is not explicitly in the model of Fig. 5.4, many of the physical elements are polarization sensitive, such as the isolator and the fiber Fabry-Perot interferometer. The orientation of the polarization controller must be optimized in the experiments for the laser to self-start [27], which shows the importance of the polarization state inside the cavity.

5.3 Stability study

We first consider CW inputs. The input-output relation has been given in Eq. (5.2). To use the laser equation, Eq. (2.35), we first take the logarithm of the

operator in Eq. (5.2) and then expand it in terms of $|U_{\text{in}}|^2$. The action of the fiber and polarizer assembly is described by

$$\frac{\partial U}{\partial z} = \ln\left[\exp(i\phi)\cos\theta\cos\psi + \sin\theta\sin\psi\right]U + iK_s\left[\frac{2}{3} + \frac{1}{3}\frac{\exp(i\phi)\cos^3\theta\cos\psi + \sin^3\theta\sin\psi}{\exp(i\phi)\cos\theta\cos\psi + \sin\theta\sin\psi}\right]|U|^2U. \tag{5.9}$$

Loss, phase shift, fast saturable absorption, and self-phase modulation are contributed by the real and imaginary parts of the first and second terms in Eq. (5.9). When $\phi = 0$, the fast saturable absorption vanishes since the coefficient of the nonlinear term becomes purely imaginary. The laser equation is obtained by adding the terms corresponding to gain, loss, dispersion, and a frequency limiter. We find

$$\frac{\partial U}{\partial z} = \left\{g_s - l + \ln\left[\exp(i\phi)\cos\theta\cos\psi + \sin\theta\sin\psi\right] + (B + iD)\frac{\partial^2}{\partial t^2} - iK_s\left[\frac{2}{3} + \frac{1}{3}\frac{\exp(i\phi)\cos^3\theta\cos\psi + \sin^3\theta\sin\psi}{\exp(i\phi)\cos\theta\cos\psi + \sin\theta\sin\psi}\right]|U|^2\right\}U. \tag{5.10}$$

The dispersion D corresponds to 22.5 psec^2 and B is 0.19 psec^2 for a 5 nm pass band. The nonlinearity is from the Kerr effect and $K_s = 3.05$ W^{-1} for the long fiber. The 10% output coupling gives $l = 0.105$.

The CW solutions and the pulse solutions for $0 \leq \phi < 2\pi$ can now be found. To illustrate the results of the analysis, we assume $\phi = 0.4$, in solving Eqs. (3.2) and (3.3), and find the operating points. We then obtain $\Gamma = 1.77$ W^{-1} and $K = 2.54$ W^{-1}. The CW output power is found to be 2.5 mW.

We assume, as always, that the laser will self-start when the CW solution is unstable. So, we examine the eigenvalues of the linearized solutions in the complex plane. We find that the laser self-starts at all ϕ values because of the large relaxation time. The eigenvalue trace on the complex plane is plotted in Fig. 5.6(a).

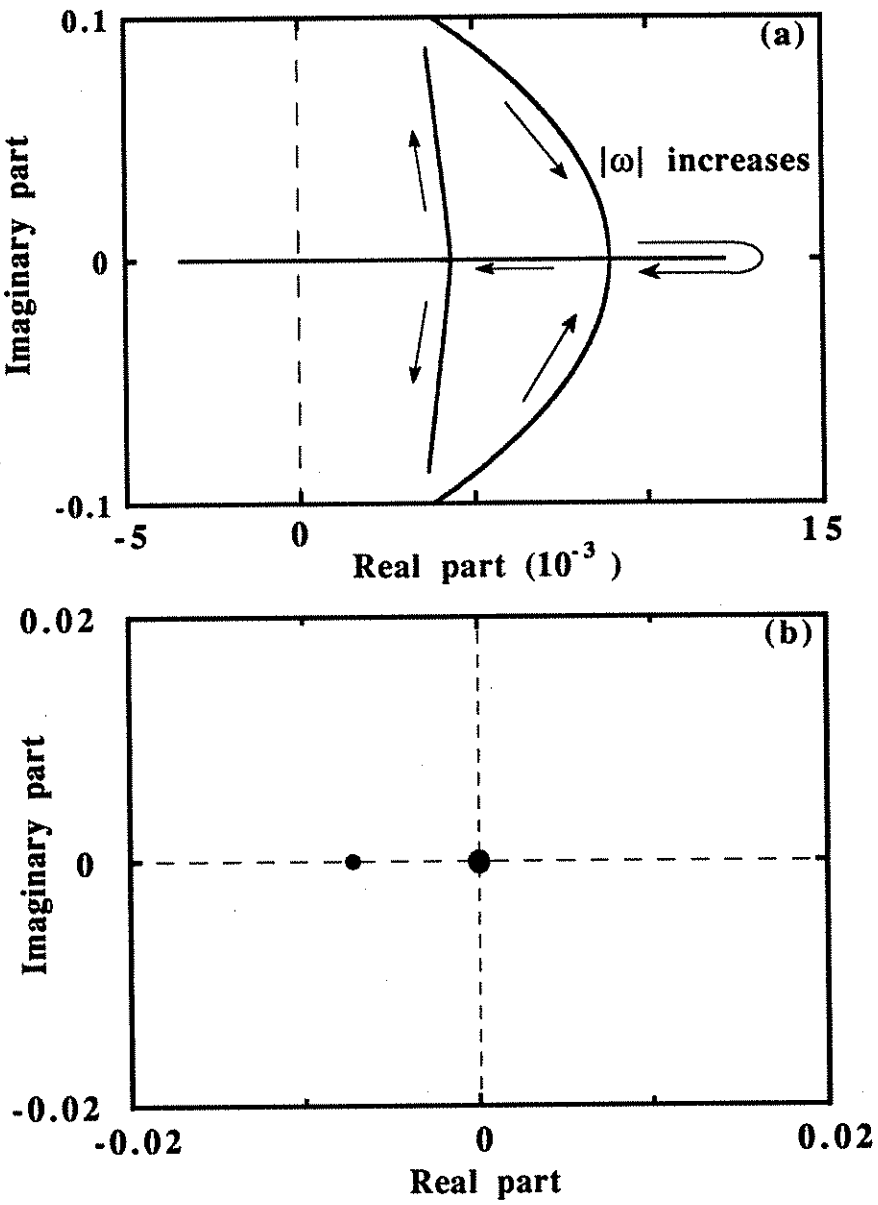

Figure 5.6: (a) Self-starting of the fiber ring laser. (b) Pulse stability of the fiber ring laser. The radiation modes all satisfy $\mathrm{Re}(\lambda) < -0.3$.

We next examine the pulse solutions. In contrast to the figure eight laser, with gain, Γ and K do not depend on gain saturation, and the analysis of Chapter 3 is directly applicable. When $\phi = 0.4$, we find two solutions. One has pulse width 4.68 psec and the other has pulse width 30.89 psec. The output powers are 17.1 mW and 2.6 mW respectively. In both cases, $\beta = -0.4170$ and $a = 0.0042$. Applying the results of Section 3.2, the stability is determined by Eqs. (3.54) and (3.55). We find that $\epsilon_{p,\min} = 0.421$ from Eq. (3.49). As expected, only the solution with lower power, for which $\epsilon_p = 5.92$, is stable. The eigenvalues obtained by solving Eq. (3.34) numerically are plotted in Fig. 5.6(b).

5.4 Simulation of modelocking

We will use the beam propagation method described in Section 3.3.2 to solve the coupled nonlinear Schrödinger equation and assume periodic boundary conditions. There is no absorber in these simulations because that is equivalent to introducing an active mode locker. The simulation is unidirectional; so, it is not necessary to model the isolator. The simulation window T is 400 psec, T_c is 5 psec. The 2000 m length of the fiber is 1.02 Z_c in normalized units. The erbium-doped fiber amplifier is typically a few meters long; hence, it is treated as a lumped gain. The normalized saturation power $P_{\text{sat}} = 0.664$, when P_{av} is replaced by $\int_{-\infty}^{\infty} |u|^2 \, ds$.

First, to demonstrate the importance of the nonlinear polarization rotation in providing saturable absorption and a frequency limiter, we used the usual nonlinear Schrödinger equation, *i.e.*, Eq. (4.8), to model the long fiber, which is equivalent to assuming that the polarizers at both ends of the long fiber are

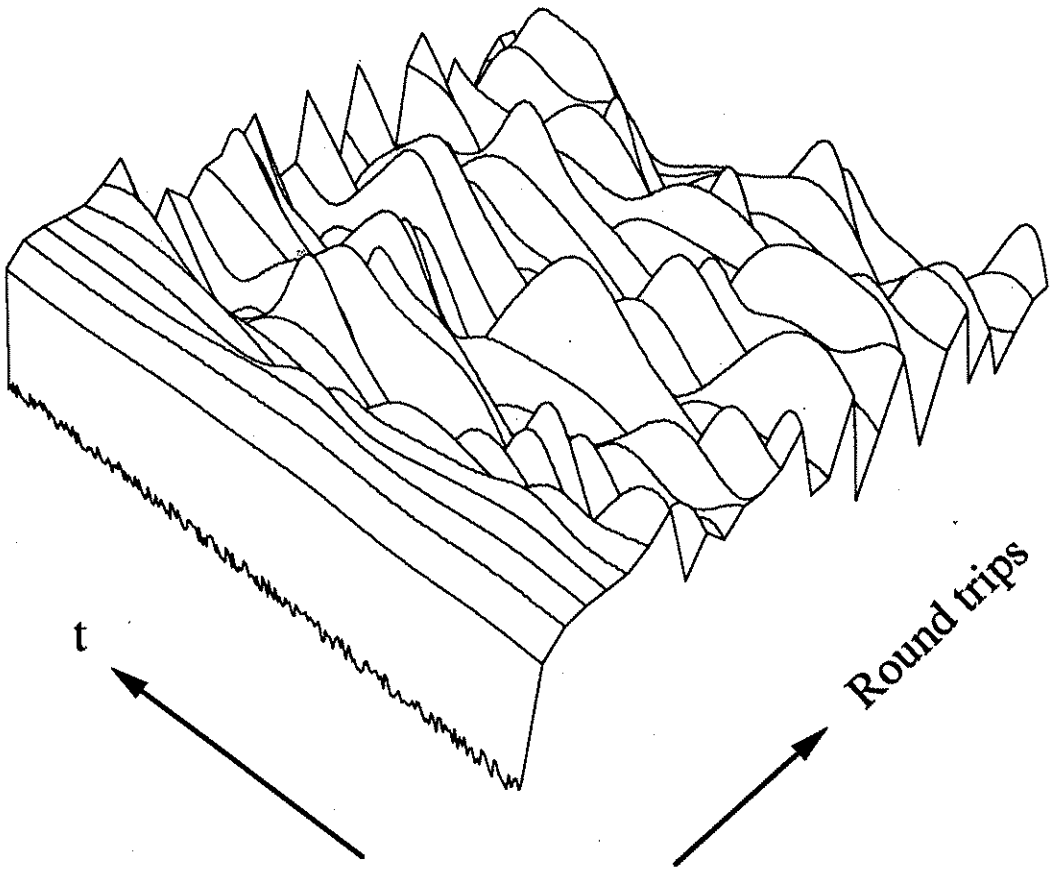

Figure 5.7: A simulation in which saturable absorption is neglected. Each line represents 10 round trips

aligned to the same axis. In the simulations, we found that the system does not self-start. We have tried several combinations of parameter values and none of them exhibit a stable pulse. A typical outcome of the simulated modelocking process is plotted in Fig. 5.7. A saturable absorber that obeys Eq. (2.32) has been introduced artificially into the loop and we observe stable pulses. We have also removed the frequency limiter while keeping the saturable absorber. We find that stable pulses do not appear. Instead, fluctuating waves similar to those in Fig. 5.7 are observed.

The saturable absorber and the frequency limiter act together to stabilize the modelocked pulse operation of the ring laser. The saturable absorber sharpens the pulse in the time domain, while the frequency limiter sharpens the pulse in the frequency domain. The detailed behavior depends strongly on the pulse shape at the input end of each element, but the actions of these two elements are balanced when we observe a fixed pulse width after one round trip through the laser. This balance is stable because if the width becomes too large, then the effect of the saturable absorber grows while that of the frequency limiter shrinks, and the pulse width tends to decrease. The converse takes place if the width becomes too small.

We attribute the saturable absorption to nonlinear polarization rotation [50]. The input polarization angle θ is then set to 22.5° and the output angle ψ is set to 112.5°. We carried out the simulation for $0 \leq \phi < 2\pi$ and found that the laser generates stable pulses in the range $0.1 \leq \phi < 0.9$. A particular simulation is presented using $\phi = 0.4$ for comparison with the stability analysis in the previous section. The simulated results are shown in Fig. 5.8. The laser self-starts from noise, generating a stable soliton train. The amplifier raises the initial noise to a

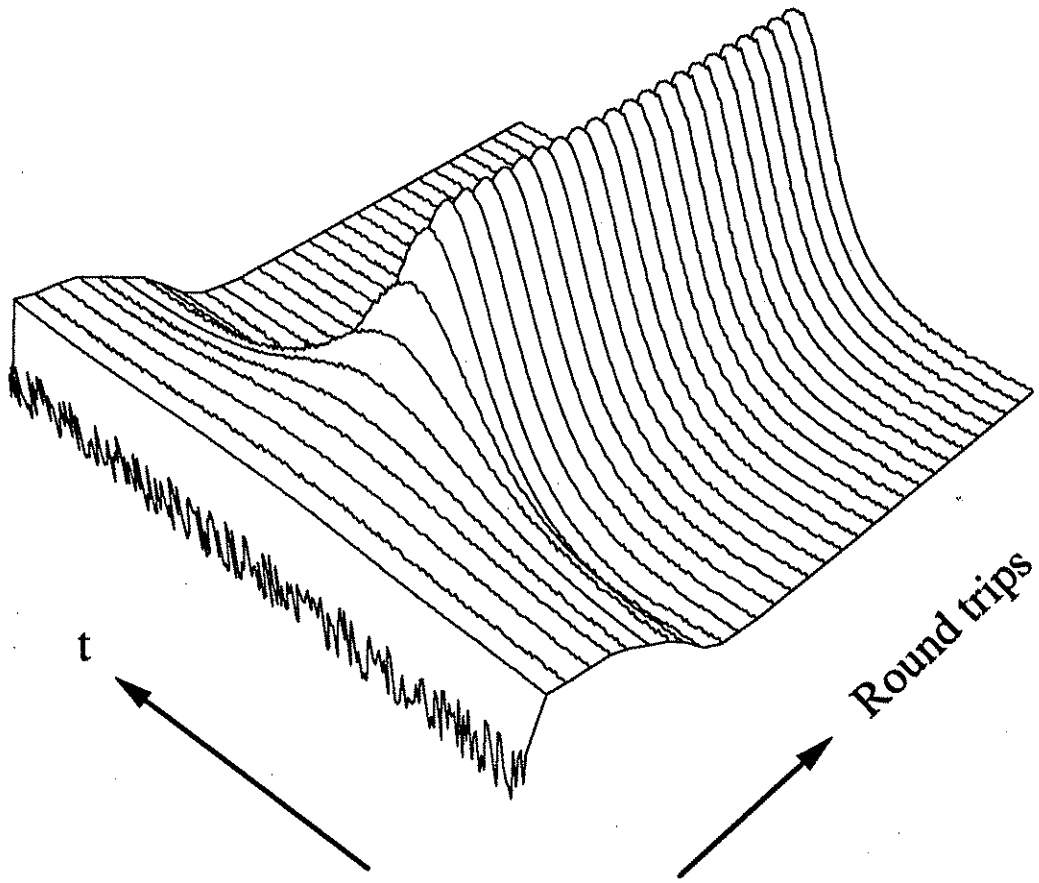

Figure 5.8: The simulated startup process. Each line represents 20 round trips

large intensity, at which point nonlinearity becomes important. The initial light train then breaks into pulses with large fluctuations. After about 200 round trips, soliton pulses emerge and remain stable. The pulse width (FWHM) in normalized units is 9.8 T_c or 49 psec, and we find a $\Delta t \Delta f = 0.393$. This value of $\Delta t \Delta f$ is close to the that of a sech pulse, which is 0.315. Note, however, the contrast with the figure eight laser, for which we found $\Delta t \Delta f = 0.28$. The figure eight laser evidently produces higher quality pulses.

5.5 Summary

We have studied the stability of the fiber ring laser and we find that the ring laser in Fig. 5.4 is self-starting if a saturable absorber and a frequency limiter are included. Numerical simulations confirm this conclusion. We have identified a plausible source of the saturable absorption in the existing experimental configuration. The match between the results from the stability analysis and the numerical simulations is reasonable. From the stability analysis, we find that stable pulses are generated when $0.1 \leq \phi \leq 1.4$, a somewhat larger range than we found in the simulations. However, the eigenvalue of the most unstable discrete mode is close to zero when $\phi \simeq 1.4$, which implies that the mode may be nonlinearly unstable; this point requires further investigation. When $\phi = 0.4$, we find that the pulse width obtained from the laser equation is 31 psec and is 49 psec from the numerical simulation. For $\beta = -0.4170$, the pulse solution in Eq. (3.14), has $\Delta t \Delta f = 0.352$, in contrast to 0.393 from simulation. Again, as in the figure eight laser, the primary cause of this discrepancy is that the saturable absorber model which we use in the stability analysis is not the same

as in the simulations because the latter becomes opaque at high power levels. By improving the model of the saturable absorber in the stability analysis, we should ultimately arrive at even better agreement.

Chapter 6

Conclusions

We have derived a laser equation which we use to study the stability of passively modelocked lasers with fast saturable absorbers. This analysis allows us to determine when a laser will self-start from noise to produce modelocked pulses. To confirm this approach and determine its limitations, we have also carried out numerical simulations. We have applied this approach to the figure eight laser and the fiber ring laser.

Both the CW and pulse solutions to the laser equation are found first. We then linearize the laser equations around the CW or pulse solution to determine its stability. To study the laser's ability to self-start, we determine the stability of the CW solutions. We derive a dispersion relation which gives the growth rate of a sinusoidal perturbation with frequency ω. We assume, as is physically plausible, that for a laser to self-start, the CW solution must be unstable at some frequency. To determine the stability of modelocked pulses, we transform the linearized equation into an eigenvalue problem. A perturbation analysis shows that gain saturation helps stabilize the modelocking by shifting the eigenvalue of an unstable discrete mode to the stable side of the complex λ-plane. When the

gain medium is the only element that depends on the pulse shape, the condition for the pulse mode to be stable is that $\epsilon_p > \epsilon_{p,\min}$, which is given analytically in Eq. (3.49). In other cases, perturbative or numerical approaches can be used to obtain the eigenvalues.

We have applied this approach to the figure eight laser and the fiber ring laser and determine the parameter regimes in which they operate stably. In both examples, we carried out numerical simulations to verify our results and their limitation. We use the beam propagation method to calculate the wave evolution inside optical fibers. Each element inside the cavity is modeled and the dynamics of the laser is studied by iterating the wave profile through each element. Comparing the simulation results to the results obtained from the laser equation, we find that the results agree reasonable well, although they suggests ways in which some elements, notably the saturable absorber, can be improved.

Our work to date suggest several directions for future research. First, the gain model in the laser equation should be improved. Second, we should modify the basic model to allow for component discreteness. Third, and most important, these results can and should be extended to lasers with moderate relaxation times such as Ti:sapphire lasers [53], [54].

Appendix A

Series Solution of the Linearized Ginzburg-Landau Equation

An effective approach for calculating bounded eigenfunctions with real eigenvalues is to use a series expansion to solve the linearized Ginzburg-Landau equation, Eq. (3.35). It is efficient because the calculation requires considerably less computation than the matrix eigenvalue solver. It is also highly accurate since we are able to bound the error and keep it small. However, the series solution method can only used to find the eigenvalues and eigenfunctions for a few discrete modes; we use the matrix eigenvalue solver to obtain a global distribution of eigenvalues, including those for radiation modes. We rely on this series solution approach to find accurate eigenvalues of Eq. (3.35) which are then compared with the results from the finite difference approach in Section 3.3.1 as an additional verification of the accuracy of the finite difference approach. We also use this approach to obtain eigenfunctions that are used in Eq. (3.44) to calculate the shift in the eigenvalue.

The series solution is described in the following. For simplicity, we will only use the upper sign of Eq. (3.35) in the following discussion, and, since we are

dealing with real eigenvalues, we will set $u = v^*$. The equation written in terms of u is

$$\lambda u = \left(a + \frac{i}{2}\right)\left\{b_1 u + \frac{\partial^2 u}{\partial s^2} - b_2\left[2\mathrm{sech}^2(s)u + \mathrm{sech}^{2+2i\beta}(s)u^*\right]\right\}. \qquad \text{(A.1)}$$

Setting $u = f(s)\mathrm{sech}^{1+i\beta}(s)$, our equation becomes

$$-b_2\mathrm{sech}^2(s)(f+f^*) - 2(1+i\beta)\tanh(s)f' + f'' = \frac{\lambda}{a+i/2}f, \qquad \text{(A.2)}$$

where, again, $b_2 = \beta^2 - 3i\beta - 2$ and the primes indicate derivatives with respect to s. We next let $w = \tanh(s)$ so that $\partial/\partial s = (1-w^2)\partial/\partial w$, and we write f as a power series in w,

$$f(w) = \sum_{n=0}^{\infty} c_{2n+n_0} w^{2n+n_0}. \qquad \text{(A.3)}$$

The function must have a definite parity. When $n_0 = 0$, f is an even function, while, when $n_0 = 1$, f is an odd function. Note that $-1 < w < 1$ for real s. Replacing the independent variable s with w, we obtain

$$-b_2(1-w^2)(f+f^*)-2(1+i\beta)w(1-w^2)\frac{\partial}{\partial w}f+(1-w^2)\frac{\partial}{\partial w}(1-w^2)\frac{\partial}{\partial w}f = \frac{\lambda}{a+i/2}f. \qquad \text{(A.4)}$$

Substituting Eq. (A.3) into Eq. (A.4) and collecting equal powers of w^{2m}, we obtain

$$\begin{aligned} 2b_2 c_{2m-2,r} + 4(1+i\beta)(m-1)c_{2m-2} + (2m-2)(2m-1)c_{2m-2} \\ -2b_2 c_{2m,r} - 4(1+i\beta)mc_{2m} - 8m^2 c_{2m} \\ +(2m+1)(2m+2)c_{2m+2} = \frac{\lambda}{a+i/2}c_{2m}, \end{aligned} \qquad \text{(A.5)}$$

where the subscript r represents the real part. Note that $2m = 2n + n_0$, and so $m = 0, 1, \cdots$ when $n_0 = 0$ and $m = 1/2, 3/2, \cdots$ when $n_0 = 1$, corresponding to

even and odd f respectively. We find, in particular, that for $m = 0$ and $m = 1$, we obtain

$$-2b_2c_{0,r} + 2c_2 = \frac{\lambda}{a + i/2}c_0, \tag{A.6}$$

$$2b_2c_{0,r} - 2b_2c_{2,r} - 4(1 + i\beta)c_2 - 8c_2 + 12c_4 = \frac{\lambda}{a + i/2}c_2. \tag{A.7}$$

When the series, Eq. (A.3), converges, an eigenvalue λ and eigenfunction u are obtained; hence, the series can only converge when λ equals an eigenvalue. One possibility is that the series truncates at a finite value of m which implies $c_{2m} = c_{2m+2} = \cdots = 0$. It follows from Eq. (A.4) that

$$2b_2c_{2m-2,r} + [4(1 + i\beta)(m - 1) + (2m - 2)(2m - 1)]c_{2m-2} = 0. \tag{A.8}$$

Dividing c_{2m-2} into its real and imaginary parts, $c_{2m-2,r}$ and $c_{2m-2,i}$, we find

$$\begin{pmatrix} 2\beta^2 - 4 + (m-1)(4m+2) & -4\beta(m-1) \\ -6\beta + 4\beta(m-1) & (m-1)(4m+2) \end{pmatrix} \begin{pmatrix} c_{2m-2,r} \\ c_{2m-2,i} \end{pmatrix} = 0, \tag{A.9}$$

which implies

$$[6\beta^2 + (m+1)(4m+2)](m-1)(2m-3) = 0. \tag{A.10}$$

Since $6\beta^2 + (m+1)(4m+2)$ is always larger than zero, the only possible values of m are $m = 1$ and $m = 3/2$, which correspond, respectively to u_{even} and u_{odd}, which we found earlier.

Assuming now that the series does not truncate, we first observe that the recursion relation, Eq. (A.5) depends on two variables, λ and θ, where θ is used to specify $c_{n_0} = \exp(i\theta)$. The value of c_{2m} at each m is a function of λ and θ and can therefore be expressed as $c_{2m}(\lambda, \theta)$.

In general, the series will diverge. To force it to converge, so that we obtain an eigenfunction and its eigenvalue, we use the following algorithm. First, the

sequence is truncated artificially at c_{2m}, *i.e.*, $c_{2m} = c_{2m+2} = \cdots = 0$. We then use Newton's method to find (λ_m, θ_m) such that $c_{2m}(\lambda, \theta) = 0$ at a specific m. Increasing the m value, we find that the (λ_m, θ_m) converges to a particular point (λ_0, θ_0) on the λ-θ plane. An eigenvalue $\lambda = \lambda_0$ is thus found as well as its corresponding eigenfunction. To find more eigenvalues, we apply the same algorithm and exclude λ_0 by searching for a zero of $c_{2m}(\lambda, \theta)/\lambda_0$ instead of $c_{2m}(\lambda, \theta)$. The process may be repeated until no more accumulation points on the λ-θ plane can be found. Since the sequence is truncated after $2n$-th term, there exists an error term associated with each truncation. The sequence $c_{n_0}, \cdots, c_{2m-2}, 0, 0, \cdots$ satisfies Eq. (A.5) up to the $m-1$. The next equation is not satisfied, and the error is

$$\begin{aligned} \mathrm{Err}_m = [&2b_2 c_{2m-2,r} + 4(1+i\beta)(m-1)c_{2m-2} \\ &+(2m-2)(2m-1)c_{2m-2}]w^{2m}(1-w^2)^{1+i\beta}, \end{aligned} \tag{A.11}$$

where $(1-w^2)^{1+i\beta}$ accounts for the $\mathrm{sech}^{1+i\beta}(s)$ term in the reduction to Eq. (A.2). We must show that the error term goes to zero as m increases. An uniform bound for $|\mathrm{Err}_m|$ over w can be find by noting that

$$\frac{1}{en} < |w^{2n}(1-w^2)^{1+i\beta}| = w^{2n}(1-w^2) < \left(\frac{n}{n+1}\right)^n \frac{1}{n} < \frac{1}{2n}, \tag{A.12}$$

which implies

$$|\mathrm{Err}_m| < [2b_2 c_{2m-2,r} + 4(1+i\beta)(m-1)c_{2m-2} + (2m-2)(2m-1)c_{2m-2}]/(2m). \tag{A.13}$$

When this bound tends to zero as $m \to \infty$, our approach must yield an eigenfunction.

A similar algorithm can be implemented when the eigenvalues are complex, but this of little interest since the eigenvalues are real in almost all cases. Finally,

the adjoint linearized Ginzburg-Landau equation, Eq. (3.43) can be solved using the same algorithm, allowing us to calculate $\Delta\lambda$ using Eq. (3.44) and to estimate $\epsilon_{p,\mathrm{min}}$. Since the calculation is efficient, we have an estimate of $\Delta\lambda$ and $\epsilon_{p,\mathrm{min}}$ before the eigenvalue problem is solved numerically. An example is found in the discussion of the stability of pulsed operation in Section 4.3.3.

Appendix B

A useful equation

In this part of the Appendix, we introduce a new function and derive a relation which is useful in our discussion of the degeneracy of the eigenvalues. Observing Eq. (3.15) and Eq. (3.16), we introduce a scaling variable η and a set of scaling transformations such that Eq. (3.15) and Eq. (3.16) continue to hold,

$$\tau \rightarrow \tau/\eta, \tag{B.1}$$

$$A \rightarrow A\eta, \tag{B.2}$$

$$g - l + i(\theta - \psi) \rightarrow \eta^2[g - l + i(\theta - \psi)]. \tag{B.3}$$

With this substitution, the *ansatz* in Eq. (3.14) becomes

$$U_0(t;\eta) = \eta A \,\mathrm{sech}^{1+i\beta}(\eta t/\tau), \tag{B.4}$$

which is a solution to the equation,

$$0 = \left\{\eta^2[g - l + i(\theta - \psi)] + (B + iD)\frac{\partial^2}{\partial t^2} + (\Gamma + iK)|U_0|^2\right\} U_0. \tag{B.5}$$

Differentiating the above equation with respect to η and evaluating at $\eta = 1$, we obtain the function

$$u_0 = A[1 - (1 + i\beta)(t/\tau)\tanh(t/\tau)]\mathrm{sech}^{1+i\beta}(t/\tau), \tag{B.6}$$

which satisfies the equation

$$-2[g-l+i(\theta-\psi)]U_0 = [g-l+i(\theta-\psi)]u_0+(B+iD)\frac{\partial^2 u_0}{\partial t^2} (\Gamma+iK)(2|U_0|^2u_0+U_0^2u_0^*), \quad \text{(B.7)}$$

where $U_0(t;\eta=1)=A\,\mathrm{sech}^{1+i\beta}(t/\tau)$ is denoted as U_0. Using the variables defined in Eqs. (3.24)–(3.28) and omitting A in Eq. (B.6), we find that

$$u_0=[1-(1+i\beta)s\tanh(s)]\mathrm{sech}^{1+i\beta}(s), \quad \text{(B.8)}$$

and the equation that it satisfies is

$$\left(a\pm\frac{i}{2}\right)\left[b_1u_0+\frac{\partial^2u_0}{\partial t^2}-2b_2\mathrm{sech}^2(s)u_0-b_2\mathrm{sech}^{2+2i\beta}(s)u_0^*\right] = -2\left(a\pm\frac{i}{2}\right)b_1\mathrm{sech}^{1+i\beta}(s) \quad \text{(B.9)}$$

When the coefficient $(a\pm i/2)b_1$ in Eq. (B.9) is imaginary, the left hand side of this equation is proportional to u_{even} in Eq. (3.40).

Bibliography

[1] A. E. Siegman, *Lasers*, Mill Valley, CA: University Science Books, 1986.

[2] A. Yariv, *Quantum Electronics*, New York: John Wiley & Sons, 1989.

[3] P. W. Smith, "Mode-locking of lasers," Proc. IEEE, vol. 58, pp. 1342-1357, 1970.

[4] C. V. Shank, "Generation of ultrashort optical pulses," in *Ultrashort Laser Pulses and Applications*, W. Kaiser, ed. Berlin; New York: Springer-Verlag, 1988.

[5] G. H. C. New, "The generation of ultrashort laser pulses," Rep. Prog. Phys., vol. 46, pp. 877-971, 1983.

[6] W. G. Wagner and B. A. Lengyel, "Evolution of the giant pulse in a laser," J. Appl. Phys., vol. 34, pp. 2040-2046, 1963.

[7] D. J. Kuizenga and A. E. Siegman, "FM and AM mode locking of the homogeneous laser – Part I: Theory," IEEE J. Quantum Electron., vol. QE-6, pp. 694-708, 1970.

[8] H. A. Haus, "Theory of mode locking with a fast saturable absorber," J. Appl. Phys., vol. 46, pp. 3049-3058, 1975.

[9] C.-J. Chen, P. K. A. Wai, and C. R. Menyuk, "A soliton fiber ring laser," Opt. Lett., vol. 17, pp. 417-419, 1992.

[10] M. L. Dennis and I. N. Duling, III, "Role of dispersion in limiting pulse width in fiber lasers," submitted to Appl. Phys. Lett. for publication.

[11] F. Krausz, T. Brabec, and Ch. Spielmann, "Self-starting passive mode locking," Opt. Lett., vol. 16, pp. 235-237, 1991.

[12] H. A. Haus, "Parameter ranges for CW passive mode locking," IEEE J. Quantum Electron., vol. QE-12, pp. 169-176, 1976.

[13] E. P. Ippen, L. Y. Liu, and H. A. Haus, "Self-starting condition for additive-pulse mode-locked lasers," Opt. Lett., vol. 15, pp. 183-185, 1990.

[14] H. A. Haus, J. G. Fujimoto, and E. P. Ippen, "Structures for additive pulse mode locking," J. Opt. Soc. Am. B, vol. 8, pp. 2068-2076, 1991.

[15] F. If, P. L. Christiansen, J. N. Elgin, J. D. Gibbon, and O. Skovgaard, "A theoretical and computational study of the soliton laser," Opt. Comm., vol. 57, pp. 350-354, 1986.

[16] K. J. Blow, and D. Wood, "Stability and compression of pulses in the soliton laser," IEEE J. Quantum Electron., vol. QE-22, pp. 1109-1116, 1986.

[17] K. J. Blow, and D. Wood, "Mode-Locked lasers with nonlinear external cavities," J. Opt. Soc. Am. B, vol. 5, pp. 629-632, 1988.

[18] G. P. Agrawal, *Nonlinear Fiber Optics*, Boston: Academic Press, 1989.

[19] W. A. Reed, L. G. Cohen, and H.-T. Shang, "Tailoring optical characteristics of dispersion-shifted lightguides for applications near 1.55 μm," AT&T Technol. J., vol. 65, pp. 105-122, 1986.

[20] H. A. Haus, "Theory of mode locking with a slow saturable absorber," IEEE J. Quantum Electron., vol. QE-11, pp. 736-746, 1975.

[21] H. A. Haus, "A theory of forced mode locking," IEEE J. Quantum Electron., vol. QE-11, pp. 323-330, 1975.

[22] The parameter g_0 and P_{sat} are obtained by determining the best fit of the measured input and output powers of a segmented of erbium-doped fiber amplifier to Eq. (2.29) in the least mean square sense.

[23] P. A. Belanger, "Soliton laser. I: A simplified model," J. Opt. Soc. Am. B, vol. 5, pp. 793-798, 1988.

[24] G. H. C. New and D. H. Rea, "Rate-equation dynamics of passively mode-locked quasicontinuous lasers: Perturbation theory of a ring laser," J. Appl. Phys., vol. 47, pp. 3107-3115, 1976.

[25] H. A. Haus, and E. P. Ippen, "Self-starting of passively mode-locked lasers," Opt. Lett., vol. 16, pp. 1331-1333, 1991.

[26] J. Goodberlet, J. Wang, and G. Fujimoto, "Starting dynamics of additive-pulse mode locking in the Ti:Al_2O_3 laser," Opt. Lett., vol. 15, pp. 1300-1302, 1990.

[27] This scheme and experimental results have been reported by Dr. Mollenauer in lectures which he gave as an IEEE/LEOS traveling lecturer.

[28] N. R. Pereira and Lennart Stenflo, "Nonlinear Schroedinger equation including growth and damping," Phys. Fluid, vol. 20, pp. 1733-1734, 1977.

[29] O. E. Martinez, R. L. Fork, and J. P. Gordon, "Theory of passively mode-locked lasers for the case of a nonlinear complex-propagation coefficient," J. Opt. Soc. Am. B, vol. 2, pp. 753-760, 1985.

[30] O. E. Martinez, R. L. Fork, and J. P. Gordon, "Theory of passively mode-locked lasers including self-phase modulation and group-velocity dispersion," Opt. Lett., vol. 9, pp. 156-158, 1984.

[31] W. H. Press, B. P. Flannery, S. A. Teukolsky, and W. T. Vetterling, *Numerical Recipes: The Art of Scientific Computing,* New York: Cambridge University Press, 1988.

[32] C. R. Menyuk, "Stability of solitons in birefringent optical fibers. II. Arbitrary amplitudes," J. Opt. Soc. Am. B, vol. 5, pp. 392-402, Feb. 1988.

[33] J. A. Valdmanis and R. L. Fork, "Design considerations for a femtosecond pulse laser balancing self phase modulation, group velocity dispersion, saturable absorption, and saturable gain," IEEE J. Quantum Electron., vol. QE-22, pp. 112-118, 1986.

[34] M. N. Islam, E. R. Sunderman, C. E. Soccolich, I. Bar-Joseph, N. Sauer, T. Y. Chang, and B. I. Miller, "Color center lasers passively mode locked by quantum wells," IEEE J. Quantum Electron., vol. 25, pp. 2454-2463, 1989.

[35] A. G. Bulushev, E. M. Dianov, and O. G. Okhotnikov, "Self-starting mode-locked laser with a nonlinear ring resonator," Opt. Lett., vol. 16, pp. 88-90, 1991.

[36] I. N. Duling, III, "Subpicosecond all-fiber erbium laser," Electron. Lett., vol. 27, pp. 544-545, 1991.

[37] I. N. Duling, III, "All-fiber ring soliton laser mode locked with a nonlinear mirror," Opt. Lett., vol. 16, pp. 539-541, 1991.

[38] N. J. Doran and D. Wood, "Nonlinear-optical loop mirror," Opt. Lett., vol. 13, pp. 56-58, 1988.

[39] K. Smith, N. J. Doran, and P. G. J. Wigley, "Pulse shaping, compression, and pedestral suppression employing a nonlinear-optical loop mirror," Opt. Lett., vol. 15, pp. 1294-1296, 1990.

[40] F. Ouellette, and M. Piche, "Pulse shaping and passive mode-locking with a nonlinear Michelson interferometer," Opt. Comm., vol. 60, pp. 99-103, 1986.

[41] V. E. Zakharov, and A. B. Shabat, "Exact theory of two-dimensional self-focusing and one-dimensional self-modulation of waves in nonlinear media," Sov. Phys. JETP, vol. 34, pp. 62-69, 1972.

[42] M. J. Ablowitz, D. J. Kaup, A. C. Newell, and H. Segur, "The inverse scattering transform - Fourier analysis for nonlinear problems," Studies Appl. Math., vol. 53, pp. 249-315, 1974.

[43] A. Hasegawa and F. Tappert, "Transmission of stationary nonlinear pulses in dispersive dielectric fibers. I. Anomalous dispersion," Appl. Phys. Lett. vol. 23, pp. 142-144, 1973.

[44] L. F. Mollenauer, R. H. Stolen, and J. P. Gordon, "Experimental observation of picosecond pulse narrowing and soliton in optical fibers," Phys. Rev. Lett., vol. 45, pp. 1095-1098, 1980.

[45] I. N. Duling, C.-J. Chen, P. K. A. Wai, and C. R. Menyuk, "Operation of a nonlinear loop mirror in a laser cavity," submitted to J. Quantum Electron. for publication.

[46] I. P. Kaminow, "Polarization in optical fibers," IEEE J. Quantum Electron., vol. QE-17, pp. 15-22, 1981.

[47] C. R. Menyuk, "Nonlinear pulse propagation in birefringent optical fibers," IEEE J. Quantum Electron., vol. QE-23, pp. 174-176, 1987.

[48] C. R. Menyuk, "Pulse propagation in an elliptically birefringent Kerr medium," IEEE J. Quantum Electron., vol. QE-25, pp. 2674-2682, 1989.

[49] R. H. Stolen, J. Botineau, and A. Ashkin, "Intensity discrimination of optical pulses with birefringent fibers," Opt. Lett., vol. 7, pp. 512-514, 1982.

[50] M. N. Islam, C. E. Soccolich, J. P. Gordon, and U. C. Paek, "Soliton intensity-dependent polarization rotation," Opt. Lett., vol. 15, pp. 21-23, 1990.

[51] M. Hofer, M. E. Fermann, F. Haberl, M. H. Ober, and A. J. Schmidt, "Mode locking with cross-phase and self-phase modulation," Opt. Lett., vol. 16, pp. 502-504, 1991.

[52] H. A. Haus, *Waves and Fields in Optoelectronics*, Englewood Cliffs, New Jersey: Prentice-Hall Inc., 1984.

[53] D. E. Spence, P. N. Kean, and W. Sibbett, "60-fsec pulse generation from a self-mode-locked Ti:sapphire laser," Opt. Lett., vol. 16, pp. 42-44, 1991.

[54] J. Goodberlet, J. Wang, J. G. Fujimoto, and P. A. Schulz, "Femtosecond passively mode-locked Ti:Al_2O_3 laser with a nonlinear external cavity," Opt. Lett., vol. 14, pp. 1125-1127, 1989.